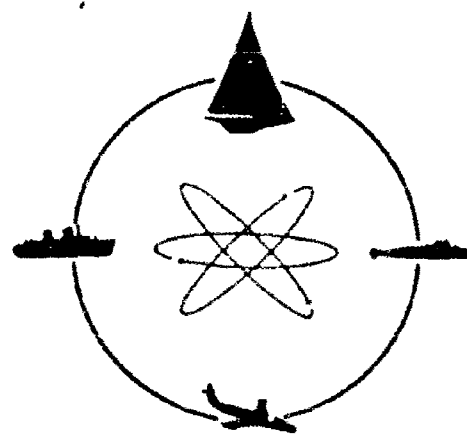
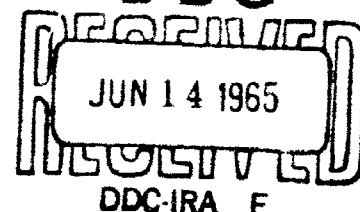


PERMIT  
ION.  
MADE IN  
DDC

R 850



# DAVIDSON LABORATORY



REPORT 850

COPY	2	OF	2	50
HARD COPY				\$ . 6.00
MICROFICHE				\$ . 1.20

PLASMA PRODUCTION  
BY  
KINETIC IMPACT

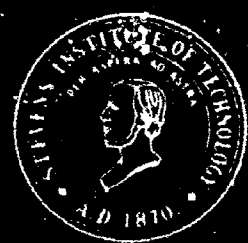
by

S.J. Lukasik  
and  
B.J. Pernick

February 1965

ARCHIVE COPY

R 850



STEVENS INSTITUTE  
OF TECHNOLOGY

CASTLE POINT STATION  
HOBOKEN, NEW JERSEY

**CLEARINGHOUSE FOR FEDERAL SCIENTIFIC AND TECHNICAL INFORMATION, CFSTI  
INPUT SECTION 410.11**

*AD 616 636*

**LIMITATIONS IN REPRODUCTION QUALITY OF TECHNICAL ABSTRACT BULLETIN  
DOCUMENTS, DEFENSE DOCUMENTATION CENTER (DDC)**

- ☐ 1. AVAILABLE ONLY FOR REFERENCE USE AT DDC FIELD SERVICES.  
COPY IS NOT AVAILABLE FOR PUBLIC SALE.
- ☒ 2. AVAILABLE COPY WILL NOT PERMIT FULLY LEGIBLE REPRODUCTION.  
REPRODUCTION WILL BE MADE IF REQUESTED BY USERS OF DDC.
  - ☒ A. COPY IS AVAILABLE FOR PUBLIC SALE.
  - ☐ B. COPY IS NOT AVAILABLE FOR PUBLIC SALE.
- ☐ 3. LIMITED NUMBER OF COPIES CONTAINING COLOR OTHER THAN BLACK  
AND WHITE ARE AVAILABLE UNTIL STOCK IS EXHAUSTED. REPRODUCTIONS  
WILL BE MADE IN BLACK AND WHITE ONLY.

TSL-121-2/65

DATE PROCESSED:

PROCESSOR:

*6-29-65*  
*B. Lee*

DAVIDSON LABORATORY

Report 850

February 1965

PLASMA PRODUCTION BY  
KINETIC IMPACT

by

S.J. Lukasik  
and  
B.J. Pernick

Prepared for the  
Department of the Army  
Contract DA-30-069-ORD-3467  
(DL Project 414)

Approved

*S.J. Lukasik*

S.J. Lukasik, Chief  
Fluid Physics Division

v + 83 pages  
17 tables, 28 figures  
9 appendices (74 pages)  
References (6 pages)

## TABLE OF CONTENTS

	Page
Abstract	i
List of Figures	iii
List of Tables	v
Part I Experimental Techniques and Gross Observations	1
1.1 Introduction	1
1.2 Explosive Shaped Charge Jets	3
1.3 Experimental Configurations	6
1.4 Instrumentation	7
1.5 Observation of a Single Shaped Charge Jet	9
1.6 Jet Collision in Air	11
1.7 Jet Collisions in Helium Atmosphere	14
(a) Framing Camera and Spectrograph Observations	15
(b) Time-Resolved Spectrum of a Jet Collision	17
Part II Analysis of Time-Resolved Spectrum	20
2.1 Spectral Line Identification	21
2.2 Spectral Line Profiles from Time-Resolved Spectrum	23
(a) Photographic Intensity Calibration	24
(b) Measurement of Spectral Line Profiles	24
2.3 Line Broadening Mechanisms	26
(a) Resonance-Broadened Line Profiles	28
(b) Instrumentation Broadening	29

## TABLE OF CONTENTS (cont'd)

	Page
(c) Line Profile Fits to Selected Transitions	32
Single-Component Profiles	34
Multicomponent Profiles	36
(d) Influence of Plasma Ions on Spectral Characteristics	37
2.4 Neutral Atom and Ion Density Estimates	43
(a) Calculation of Neutral Atom Density	44
(b) Calculation of Ion Density	48
Holtsmark Theory - Linear Stark Effect	49
Folded Distribution - Linear Stark Effect	51
Holtsmark Theory - Quadratic Stark Effect	53
2.5 Error and Uncertainty Estimates	56
(a) Film Sensitivity	56
(b) Wavelength Calibration Effect on Line Width	57
(c) Spectrograph Slit Width	58
(d) Densitometer Slit Width	58
(e) Absolute Oscillator Strength	59
(f) Self-Absorption	59
(g) Wavelength Calibration Effect on Line Shift	64
(h) Effect of Fitting Sensitivity on Line Shift	65
(i) Precision of Stark Coefficients	65
(j) Validity of Stark Coefficient Measurements	66
(k) Validity of Assumption of Negligible Shift of Central Component	66

## TABLE OF CONTENTS (con't)

	Page
2.6 Plasma Temperature Estimates	68
Part III Discussion of Results	74
3.1 Pertinent Hypervelocity Impact Theory	74
3.2 Discussion of Experimental Results	77
3.3 Further Extensions and Applications	80

### Appendices

A	Summary of Experimental Firings
B	Direct-Vision Prism and Streak Camera Combination
C	Spectral Line Profile Program
D	Photometric Emulsion Calibration
E	Spectrograph Slit Image Width Calculations
F	Integrated Lorentzian Profile Computer Programs
G	Spectral Line Shift Calculations
H	Densitometer Slit Brodening Effects
I	Spectral Line Self-Absorption Calculations

### References

### Acknowledgements

### Biography

**BLANK PAGE**

## PLASMA PRODUCTION BY KINETIC IMPACT

### Abstract

High speed photographic and time-resolved spectrographic observations have been made of the head-on collision of two hypervelocity copper jets formed from metal-lined explosive charges. Streak camera records show that the jets are moving at about 8 mm/ $\mu$ sec, or equivalently, with a kinetic energy of 21 ev/atom. Framing camera observations of the collision in air and in a low pressure helium atmosphere indicate that a region of intense luminosity is created about the point of impact. Time-integrated spectrograph records show that the composition of the collision light over the visible region is that of a continuum with superposed copper spectral lines. A time-resolved spectral record in the 4400-5300Å region of a collision in helium shows that an intense continuum first appears for about 5  $\mu$ sec. The continuum intensity then decreases and a copper emission line spectrum emerges, consisting of both neutral and first-ionized copper lines. The ionized copper lines originate from energy levels that are about 25 ev above the neutral atom ground state.

Several neutral copper lines are shown to possess combined instrumentation and resonance-broadened profiles. Estimates of the neutral copper atom density in the jet collision plasma are derived from line halfwidth measurements resulting from theoretical profile fits to the observed line shapes. Neutral atom densities are of the order of  $4 \times 10^{19} \text{ cm}^{-3}$ . An intermolecular electric field created by copper ions and electrons in the plasma result in a Stark shift of the observed CuI 4531 line. The copper ion densities determined from measured



wavelength shifts of this line are about  $4 \times 10^{17} \text{ cm}^{-3}$ .

Oscillator strengths for two neutral copper transitions observed in the time-resolved spectrum are also determined. A comparison of the resonance-broadened halfwidths for the CuI 4525 and 4643 lines with that of the CuI 4651 line whose oscillator strength is known results in an estimate of the f-numbers for these transitions.

Conclusions derived from existing theoretical models of hyper-velocity impact are found to be in good agreement with the observations and detailed measurements obtained from these experiments. Applications of this work to other areas of interest are indicated.

Benjamin J. Pernick, Author

Stephen J. Lukasik, Thesis Advisor

## List of Figures

1. Explosive Shaped Charge Jet Formation
2. Explosive Mounting and Support Structure
3. Vacuum Chamber Used in Firing No. 109
4. Plan-View of Firing Chamber
5. Typical Timing Sequence
6. Framing Camera Record of Jet Formed by Copper-Lined Shaped Charge
7. Framing Camera Record of Jet Collision in Air
8. Streak Camera of Two Copper Jets Before and After Collision
9. Time-Integrated Spectrum of Jet Collision in Air
10. Framing Camera Record of Jet Collision in Firing No. 109
11. Framing Camera Record of Jet Collision in Firing No. 124
12. Recovered Support Structure
13. Time-Integrated Spectrum of Jet Collision in Helium
14. Time-Resolved Spectrum of Jet Collision in Helium
15. Densitometer Scans of Time-Resolved Spectrum
16. Copper Energy Level Diagram
17. Slit Image Width Variation with Wavelength
18. Cul 4587 Integrated Lorentzian Fits
19. Cul 4651 Integrated Lorentzian Fits
20. Cul 5153 Integrated Lorentzian Fits
21. Integrated Lorentzian Profile Cul 4643, 4651 at 6.7  $\mu$ sec
22. Integrated Lorentzian Profile Cul 4525, 4531, 4540 at 5.7  $\mu$ sec  
4531 Split and Shifted
23. Integrated Lorentzian Profile Cul 4525, 4531, 4540 at 6.7  $\mu$ sec  
4531 Split and Shifted

- 24. Integrated Lorentzian Profile CuI 4525, 4531, 4540 at 5.7  $\mu$ sec  
No Shift in 4531
- 25. Integrated Lorentzian Profile CuI 4525, 4531, 4540 at 6.7  $\mu$ sec  
No Shift in 4531
- 26. Time Variation of Neutral Copper Atom Density in Jet Collision  
Plasma
- 27. Variation of CuI 4531 Line Shift with Plasma Ion Density
- 28. Time Variation of Jet Collision Plasma Temperature
- D-1 Photometric Emulsion Calibration Setup
- D-2 Photometric Emulsion Calibration
- E-1 Optical Ray Trace Diagram
- H-1 Schematic Diagram of Densitometer
- I-1 Normalized Self-Absorbed CuI 4651 Profile
- I-2 Self-Absorbed CuI 4651 Profile
- I-3 Normalized Self-Absorbed CuI 5153 Profile
- I-4 Self-Absorbed CuI 5153 Profile

## List of Tables

- |      |                                                                                                                |
|------|----------------------------------------------------------------------------------------------------------------|
| I    | Explosive Shaped Charge Specifications                                                                         |
| II   | Summary of Jet Velocity Measurements                                                                           |
| III  | Absorption Lines in the Time-Integrated Spectrum of a Jet Collision in Air                                     |
| IV   | Emission Lines in the Time-Resolved Spectrum of a Jet Collision in Helium                                      |
| V    | Values of Emulsion Calibration Curve Slope $\gamma$                                                            |
| VI   | Values of the Constant in Eq (2-8)                                                                             |
| VII  | Resonance-Broadened Line Halfwidths as Determined from Integrated Lorentzian Profile Fits                      |
| VIII | Relative Intensities as Determined from Multicomponent Integrated Lorentzian Profile Fits                      |
| IX   | Stark Splitting and Shift for Selected Neutral Copper Lines                                                    |
| X    | CuI 4531 Wavelength Shift and Stark Component Separation as Determined from Integrated Lorentzian Profile Fits |
| XI   | Oscillator Strengths for Several CuI Lines                                                                     |
| XII  | Neutral Copper Atom Density in the Jet Collision Plasma                                                        |
| XIII | Oscillator Strengths for CuI 4643 and CuI 4525                                                                 |
| XIV  | Copper Ion Density in the Jet Collision Plasma                                                                 |
| XV   | Stark Coefficients of Several Copper Lines                                                                     |
| XVI  | Jet Collision Plasma Temperatures                                                                              |
| XVII | Comparison of Oscillator Strength Values                                                                       |

**BLANK PAGE**

## Part I Experimental Techniques and Gross Observations

The primary objective of this work is to investigate the possibility of plasma production by the direct collision of two high velocity high density metallic jets. This appears feasible on a simple energetic basis since the kinetic energy per atom in a jet is well in excess of the energy required to ionize the atom. The velocity of the jets used here corresponds to a kinetic energy of 21 ev/atom whereas the energy required to vaporize and ionize an atom from the jet material is of the order of 10 ev. Conversion to thermal energy of this directed kinetic energy upon collision was expected to result in excitation and ionization of the jet material. Primary reliance has been placed on the use of the time-resolved spectrum of the impact light as a diagnostic aid to determine the nature of the collision process.

### 1.1 Introduction

Recent experiments concerned with the impact of explosively driven, high speed metallic projectiles and targets have indicated that charged particles along with vaporized neutral atoms of the projectile and target materials are produced upon collision. Qualitative observations of the projectile-target impact by Clark, et al (1959) and Cook and Keyes (1959) have indicated that an intense luminosity is generated upon collision. Experiments by Allen, et al (1959) and Grow, et al (1960) have shown that spectral line radiation characteristic of neutral atoms of the projectile and target materials was generated by the impact. Keyes, et al (1960) and Friichtenicht and Slattery, (1963) have indicated that at high

projectile velocities ionized atoms of the projectile and target materials are present in the impact-generated vapor. It has been suggested by Koslov (1959) and others, (Allen, et al, 1959) that collision between solid materials moving at sufficiently high relative velocities could result in the production of plasmas with appreciably high ion concentrations. Development of this technique for the production of high density plasmas and the study of its nature is of considerable interest and value since this method represents a different procedure in the present day technology of plasma production, (Bishop, 1958; Fischer and Mansur, 1958; Lochte-Holtgreven, 1958).

Two potential applications have evolved from this work over and above the stated plasma physics interest. It will be shown that these experimental methods can be employed in the determination of atomic oscillator strengths or f-numbers for the material constituents of the collision plasma. Such results would add to the existing knowledge of oscillator strengths presently determined with different experimental techniques, (Allen and Asaad, 1957; Corliss and Bozman, 1962). Furthermore these methods could be used in principle for the determination of relative oscillator strengths of metallic ions for which information is relatively sparse (Dickerman 1961; Allen, 1963).

Lukasik, et al (1964), have shown that hydrodynamic pressures of the order of tens of megabars exist at the moment of impact for the jet velocities used in this work. These values are arrived at from an assumed equation of state for the jet material and using a hydrodynamic model of the collision process. The subsequent motion of the jet collision products was shown to be dependent upon the magnitude of this

initial impact pressure. Conversely, experimental observations of the motion of the collision products can from this hydrodynamic model result in a measure of the initial impact pressure. This procedure would be of importance for materials whose equation of state is not well established or for which no such measurements have been made at such high pressures. In addition, with the advent of hypervelocity projectiles at speeds higher than that used in this study (Jameson, 1963) it appears feasible that experimental measurements could be extended into the hitherto unattainable megabar pressure ranges.

The primary aim of this effort is to quantitatively determine the degree of ionization in a plasma generated by the impact of two bodies moving at high relative speeds. This is achieved from a detailed spectral analysis of the optical radiation from the collision-produced plasma. It will be shown that the predominant physical mechanisms that affect the observed spectral lines are due to resonance interactions and intermolecular ionic fields. Estimates for the neutral and ion particle density of the collision plasma are attained from a comparison of predicted and observed spectrum line profiles. Collision plasma temperature estimates are derived from the results of the analysis.

## 1.2 Explosive Shaped Charge Jets

Certain criteria of a general nature must be considered in the decision of what type of accelerator-projectile system should be used in this study. First, one must provide for an efficient conversion of kinetic to internal energy of the collision products in order to produce a high density plasma. If the projectile material density is that of a



gas then the "colliding" objects will in effect penetrate each other with little interaction and remain relatively uncoupled. On the other hand a strong, localized interaction and presumably a high degree of thermalization of the initial directed energy is expected from the collision of two solid projectiles.

In addition, the projectile velocity must be sufficiently high so that the kinetic energy per atom is at least greater than the energy necessary to vaporize and ionize the atom. Assuming the heat of vaporization or heat of sublimation as representative of the necessary energy to remove an atom from a solid projectile under impact conditions, then the minimum requisite kinetic energy sufficient to vaporize and ionize an atom is typically of the order of 10 eV for metallic projectiles.

Several different methods are available for producing high velocity projectiles. Gas guns (Boyd, et al, 1959; Crews, 1959), electrostatic and electromagnetic accelerators (Bergstrahl, et al, 1959), exploding wires (Chace and Moore, 1962), explosively driven pellets (Summers and Charters, 1959; Kineke, 1959), explosive shaped charges, and plasma guns have been used to accelerate materials to high speeds. Although very high velocity plasmoids can be obtained from plasma guns, it appeared that a significant degree of thermalization of the initial kinetic energy would be less likely to be achieved due to the low material density. Of the remaining possibilities, however, only explosive techniques have resulted in the production of high speed projectiles with a substantial density. This reflects the fact that the available energy density of a chemical explosive is extremely high, of the order of  $10^4$  joules/cm<sup>3</sup> of high explosive (Cook, 1958).

Metallic jets formed with explosive shaped charges were used as projectiles in this work rather than explosively driven pellets. This was desirable since the velocities attainable with shaped charge jets are much larger than that for pellets, typically  $8 \text{ mm}/\mu\text{sec}$  as compared to  $2\text{--}4 \text{ mm}/\mu\text{sec}$ . An additional factor of two increase in relative impact velocity was achieved by firing two jets directly at each other causing a head-on collision, rather than one jet into a stationary target. Thus, the kinetic energy per atom of a shaped charge jet moving with a velocity of  $8 \text{ mm}/\mu\text{sec}$  is  $0.33A \text{ ev/atom}$ , where  $A$  is the atomic weight of the jet material.

The formation of a shaped charge jet is described briefly as follows. Consider a block of high explosive with a metal liner embedded into one end as shown in Fig. 1(a). The explosive is initiated at the face opposite the liner and the detonation front moves as indicated. When the detonation reaches the liner, the liner is deformed and collapses inward as illustrated in Fig. 1(b). As the liner material arrives at the axial region a high speed jet is developed and moves in the indicated direction. A comprehensive review of the theory of shaped charge jet formation and experimental verification have been presented by Birkhoff, et al (1948); Pugh, et al (1952); Eichelberger and Pugh (1952); Walsh, et al (1953); Eichelberger (1955); and Cook (1958).

Cylindrical explosive shaped charges with a conical liner insert of copper were used in this experimental work. The choice of copper as a liner material was based on its ability to form reproducible and predictable jets and on the availability of standard explosive charges. Equally important aside from the charge technology is the fact that spectral line

and energy level information, ionization potential, and equation of state data are known for copper. Specifications of the explosive design are given in Table 1. These shaped charges produce a jet whose tip travels at about 8 mm/ $\mu$ sec or equivalently with a kinetic energy of about 21 ev per copper atom. This latter figure is of interest since it is representative of the explosively derived energy directly available to the impact-generated plasma.

### 1.3 Experimental Configurations

Two types of explosive charge mountings were employed in these jet collision experiments. For firings in air, both shaped charges were simply mounted onto a wooden support frame and secured in position. Alignment of the two opposing shaped charges was made by inserting between the charges a collapsible rod whose ends were machined to the liner cone angle.

For one firing in a low pressure atmosphere, (firing no. 109<sup>\*</sup>), the assembly shown in Fig. 2 was employed. The charges were mounted behind 1/2 in. thick aluminum plates which acted as baffles to delay the explosive reaction products from obscuring the jet collision region between the plates. A cone base-to-base separation of 4 in., or two charge diameters was used. It was felt that any significant deviation from axial jet motion would be small at these short standoff distances. The jet from each shaped charge passed freely through a hole in the center of each

---

\*A tabulated summary of experimental firings appears in Appendix A.

baffle plate into the region between the plates. The other rods and plates are supporting structures to hold the explosive charges securely in place.

A 3 ft section of steel pipe, 1 ft inside diameter, 1/2 in. wall thickness served as a vacuum chamber for this configuration, as shown in Fig. 3. Three rectangular observation ports were included in the pipe section to facilitate optical observations of the jet collision. In subsequent firings expendable vacuum chambers were used. These consisted of a cylindrical section of clear lucite, 2 ft in length, 1 ft outside diameter, and 1/4 in. wall thickness. The explosive support mounts were similar to that described above. All vacuum systems were operated at pressures below 1 mm Hg.

#### 1.4 Instrumentation

All of the preparations involving explosive charges and firings were performed at a Picatinny Arsenal explosive facility.\* A plan-view of the firing chamber is illustrated in Fig. 4. Optical observation of the explosive system during a firing is possible by means of three lucite covered openings or ports in the firing chamber wall. The lines of sight through each port are coincident at the position of the explosive system, thereby allowing convenient, simultaneous observation of an explosive event by several optical systems. A firing is viewed with a Beckman and Whitley Model No. 189 Framing Camera located at one of the observation ports in

---

\*A detailed description of the facility is given in the "Proceedings of the 14th Meeting of Picatinny Arsenal Scientific Advisory Council" at Picatinny Arsenal 25, 26 April 1957.

in the camera room. This camera provides a film record that consists of 25 frames on 35 mm film. A time interval between frames of 1.4  $\mu$ sec was found appropriate for these experiments. The individual frame exposure time at this framing rate is about 0.5  $\mu$ sec.

A Hilger Medium Quartz Spectrograph mounted at an adjacent observation port provided a time-integrated spectrum of a shaped charge jet collision. Although a time-integrated spectral record is of limited use for a detailed interpretation of rapidly changing luminous events, it is nevertheless of some value in its ability to cover a wide wavelength range. Its chief function therefore is to aid in spectral line identification of jet collision luminosity over a broad wavelength band. The spectra of other light sources were recorded on the same plate as a jet collision spectrum for wavelength calibration.

A Beckman and Whitley Model No. 194 Continuous Writing Streak Camera was used in earlier experiments principally to measure the shaped charge jet velocity prior to impact. In subsequent firings the entrance optics to the streak camera were modified to include a direct-vision prism, which led to a time-resolved spectral record of a jet collision. A detailed discussion of this optical arrangement is given in Appendix B.

The high emulsion speed Kodak Tri-X or Pan-X 35 mm film was used for all streak and framing camera records; Tri-X alone was used for all time-resolved spectral records. The Hilger spectrograph accommodated 4 x 10 in. photographic glass plates, Kodak type 103-F and, on one occasion, type 103-0 emulsions were employed. All photographic records were developed in Kodak D-19 developer for 7 minutes under normal development conditions.

Initiation of detonation achieved with electronic firing units\*, is synchronized with the framing camera such that the camera is ready to record the explosive event at a predetermined time after the initiation of the detonation. Rutherford Model A2 Time Delay Generators were employed to provide this timing synchronization. Since the streak camera is continuous writing, no special time synchronization is required.

A typical timing sequence for a jet collision experiment is illustrated in Fig. 5, the indicated time delays are those for firing no. 109. The explosive configuration is to be viewed by the framing camera starting at a time when the jets first appear from behind the baffle plates. The time required for the framing camera rotating mirror to be in position after a firing pulse is generated (at zero time) was 153  $\mu\text{sec}$ . However, the time interval in which the jets first appear after initiation of detonation was found to be 21  $\mu\text{sec}$ . Thus the firing pulse must be delayed 132  $\mu\text{sec}$  by the delay generator before it initiates the explosive detonator for proper camera synchronization. The generation of an 82  $\mu\text{sec}$  delayed pulse supplied to an exploding wire is of importance for the time-resolved spectrum for this firing and is described below.

### 1.5 Observation of a Single Shaped Charge Jet

To obtain a description of the jet characteristics and to experimentally verify timing estimates, a single shaped charge was fired in air, (firing no. 56). Time delays were established so as to have detonation

---

\*A description of these firing units is given by Walbrecht (1959).

of the explosive completed when the framing camera is in position to expose the first frame. The framing camera record for this firing is shown in Fig. 6. The view is normal to the charge axis and hence to the direction of detonation and jet motion. The edge of the explosive charge is located at the extreme left-hand side of each frame. The direction of detonation and jet travel is from left to right in the figure.

The base of the undetonated charge is just visible on the extreme left side of the first frame in the figure. In the second frame the luminous reaction products extending from the base of the charge are visible. Thus completion of the charge detonation occurred in the time interval between the first two frames. The luminous tip of the jet is first observed to emerge from behind the expanding reaction products at the fourth frame; the jet is seen to lead the reaction products at subsequent times. The jet tip is luminous and comet-like in appearance, due to radiation. The narrow jet stem, whose diameter is of the order of 2 mm near the tip, is readily seen in later frames. The jet has traversed a distance of one charge diameter from the base of the charge just prior to the ninth frame, 11  $\mu\text{sec}$  after the first frame. Since the charge was initiated 17  $\mu\text{sec}$  prior to camera synchronization, a shaped charge jet is formed and travels a distance of one charge diameter from the base of the charge in a time interval of 28  $\mu\text{sec}$  after initiation of the explosive train. An uncertainty of the order of one to two microseconds is ascribed to this time estimate, reflecting the uncertainty in framing camera synchronization time and in the delay generator setting.

A measurement of the jet velocity has been obtained from the streak camera record of this firing. A summary of jet velocity measurements

obtained from this and other streak camera records is given in Table II. A nominal jet speed of 7.9 mm/ $\mu$ sec was found from these results. This value of jet speed and the above time estimates were used as a basis for establishing the timing sequence in succeeding experiments.

### 1.6 Jet Collision in Air

A number of colliding jet experiments were performed in air in order to observe the main features of jet impact. Framing and streak camera records of the collision were obtained. In addition, a time-integrated spectral record of the collision was obtained for one of these firings, the intent of which was to ascertain the presence of characteristic radiation from the copper atoms resulting from the collision.

A framing camera record for one of these experiments, (firing no. 77), is shown in Fig. 7. The direction of jet motion as shown is vertical. The approaching jets first appear from behind the expanding reaction products in the second frame. A conventional explosively-shocked argon source provided back lighting for the framing camera record. As was observed before, the jet tips are luminous and comet-like in appearance. The jet stem is readily noticeable in later frames. Collision occurs between the thirteenth and fourteenth frames, with a high luminous collision region first observed at the fourteenth frame. This region expands in time, and its extreme brightness persists for the duration of the film record. The growing dark areas apparent in the last three frames, are presumed due to expansion cooling and interaction with the encroaching explosive reaction products.



A streak camera record of another jet collision experiment, (firing no. 59), is shown in Fig. 8. On the left side of the figure appears an image of a marker scale, which physically is located at the explosive setup. This feature provides a calibration between spatial position at the explosive event and transverse distance on film. The time scale calibration is known in terms of the streak camera rotational speed. The direction of increasing time is from left to right. The streak camera entrance slit is oriented in the direction of jet motion. The approaching jets are represented by two narrow light trails that start at the left side of the figure; the light comes from the luminous jet tips. Jet collision is characterized by the intersection of these trails and subsequent intense exposure that lasts for about 50  $\mu$ sec. A region of intense luminosity, approximately centered about the impact point, is seen to remain roughly localized for the length of the record. Aside from the initial jet velocity information contained in a streak record, the extremely high light intensity of the collision products is apparent, even when viewed through a narrow streak camera entrance slit.

In firing no. 99, a time-integrated spectrum of a jet collision in air was obtained. Figure 9 shows the observed spectrum along with a densitometer scan and a comparison copper spark spectrum. The overall characteristic of the time-integrated spectrum is that of a continuum with a few weak superposed absorption lines over a wavelength range from 3600 to 5000Å. The lack of radiation beyond 5000Å is due to a decrease in sensitivity of the Type-0 emulsion beyond this wavelength. Glass and lucite in the optical path of the spectrograph are primarily responsible for the decrease in photographic sensitivity below 3600Å. Absorption

lines in the spectrum were identified by both direct association with known copper spark lines on the spectral record, (Shenstone, 1936; 1948), and by measurements of line position on the wavelength-calibrated densitometer trace.

Table III presents the absorption lines observed in this time-integrated spectrum along with associated known lines of copper. Deviations in wavelength from the known copper lines are predominantly due to poor definition of the center of these absorption lines. The energy of the lower excitation level (Moore, 1952) for the observed lines is also given in the table. Most of the levels are of the order of 5 ev above the ground state of copper. Thus, the time-integrated spectrum of a jet collision in air shows that some of the jet material is vaporized, and furthermore a fraction of these gaseous copper atoms reside in excited levels energetically several electron volts above the neutral copper atom ground state.

Spectral line tabulations show a multitude of characteristic copper lines for the spectral region covered in this experiment that were not observed here. Moreover, these lines come from energetically similar excited states and have comparable tabulated relative intensities, hence observation of these lines was expected. That these transitions are not seen either in emission or absorption is attributed to at least two factors. A time-integrated spectrum indiscriminately records light from other phases and parts of the collision luminosity. This may have blotted out or made indistinct any indication as to the presence of these missing spectral transitions. Also, masking of collision luminosity, due to the presence of an air shock created at the time of collision and propagated

along with the collision products and quenching due to energy transfer to the surrounding atmosphere are of importance. Spectral characteristics of the radiation emerging from the shocked air envelope can be substantially different from that of the enclosed luminous collision products (Bethe, et al, 1947). In the extreme case of an optically thick shock zone, the observed spectral radiation would be characteristic of the shock rather than of the jet collision products.

### 1.7 Jet Collisions in Helium Atmosphere

Two modifications were introduced in subsequent experiments that were designed to alleviate the above mentioned difficulties. First, a direct-view prism was added to the streak camera entrance optics to enable time-resolved spectroscopic observations to be made, (see Appendix B). Thus, knowing the time sequence of events in a collision experiment, a time-resolved spectral record enables one to separate, in time, radiation from the collision products and from other luminous phases of the experiment. Secondly, to eliminate the influence of air shock luminosity and shock opacity, experiments were performed in a low pressure helium atmosphere. Such an environment should be transparent to collision radiation. Optical transitions for helium in the visible region are associated with helium energy levels that are about 20 ev above its ground state. In addition, no appreciable population of these highly excited levels is expected during the course of the experiment since the density of helium atoms at the residual pressures is low, of the order of  $10^{16} \text{ cm}^{-3}$ . The vacuum systems employed for these firings were described above.

(a) Framing Camera and Spectrograph Observations

In firing no. 109, two shaped charge jets collided in helium at a residual pressure of 0.7 mm of Hg. The framing camera record for this experiment is shown in Fig. 10. The view is through one of the rectangular ports on the side of the vacuum chamber. An outline of the port is readily discernable in later frames of the record. Initial jet motion is horizontal as presented in the figure. The jets are not visible prior to impact since no backlighting was used in this firing.

In the first two frames only light from the explosive reaction products and reflections from portions of the support structure is observed. Jet impact is first seen in the third frame, as evidenced by the small, centrally located, luminous region. A brilliant flash of light is seen that persists for about four frames or  $6 \mu\text{sec}$  after first impact light. After this there is a decrease in intensity over the collision region lasting for a few frames. An apparent relighting occurs between the tenth and eleventh frame, about  $10 \mu\text{sec}$  after collision. The intensity remains high throughout the remainder of the record although the view becomes complicated by detonation products entering the collision region and possible mechanical failure of the vacuum chamber at these later times.

A vertical, luminous line structure at the position of first impact light is observed on the sixth frame. The light intensity and definition of the strip are enhanced in following frames. Lukasik, et al (1964) have presented a hydrodynamic model for the impact of two high speed projectiles in which they suggest that a radially-symmetric expanding sheet, traveling outward from the collision point, is formed at impact. Other

evidence for the formation of a sheet-like structure in a jet collision can be seen in the framing camera record of firing no. 124, shown in Fig. 11 where two shaped charge jets collided in an expendable lucite vacuum chamber. As before, initial jet motion is horizontal as presented in the figure. Jet impact is first seen in the sixth frame, as indicated by the small, intensely luminous region centered between the explosive reaction products. As early as the second frame after initial impact a vertical, luminous strip is apparent, originating at the point of impact. The intensity of the light from this sheet increases rapidly and becomes the most prominent feature of the record in later frames. Further evidence of a mechanical nature for the formation of a sheet-like structure was found in the remains of the support structure recovered after firing no. 125. Figure 12 shows the recovered structure. Jet collision was not head-on and so the sheet was not normal to the direction of jet travel. It appears that the expanding sheet collided with one of the support plates; the narrow region of impact is most obvious in the photograph.

A time-integrated spectral record of a jet collision in helium, (firing no. 109), together with a densitometer trace and copper spark reference spectrum is shown in Fig. 13. The spectral record contains many pronounced absorption lines and a number of emission lines superposed upon a continuous background. The correspondence between lines in the collision spectrum and in the copper reference spectrum is readily seen. A type 103-F photographic emulsion was used here, extending the wavelength range covered to about 7000Å. Many more distinct spectral lines are seen in this record than in the previously shown time-integrated spectrum for a collision in air. The comparatively rich spectral content of this

record indicates that the choice of helium as a residual gas in the vacuum chamber was reasonable. No detailed line identification was made from this record or other similar time-integrated records. Instead, major emphasis was directed towards an extensive analysis of the time-resolved spectral record of firing no. 109, presented below.

#### (b) Time-Resolved Spectrum of a Jet Collision

A time-resolved spectrum of a jet collision in helium is shown in Fig. 14. The wavelength range extends from about 4400 to 5300Å. This range was chosen for two reasons. A number of prominent neutral copper lines appear in this interval, (Shenstone, 1948) which encompass all of the salient features of the energy level structure of neutral copper. In addition, a number of ionized copper lines also appear in this range (Shenstone, 1936). In particular, there are a large number of ionized copper lines in the 4900 to 5000Å region with no interfering neutral copper lines. Thus, this spectral region serves as an excellent indicator for the presence of singly ionized copper in the collision plasma.

Included on the film record are zinc and helium calibration lines, a copper spark reference spectrum, and an exploding gold wire spectrum. The exploding wire spectrum served as a time fiducial mark. Its purpose was to enable one to correlate spectral information on the record with the overall time sequence of events in the experiment. (The timing sequence for firing no. 109 was previously shown in Fig. 5.) The gold wire was fired 50  $\mu$ sec before initiation of detonation, a sufficient time interval in advance of detonation to assure that light from the exploding wire does not overlap light from the jet collision. Allowing for a 28  $\mu$ sec interval in which the shaped charge jets are formed and travel a distance

of one charge diameter, a total estimated time between initiation of the exploding wire and initial jet impact is 78  $\mu\text{sec}$ . The observed time interval of 79  $\mu\text{sec}$  on the spectral record is in agreement with these known time delays. Thus, one can be certain that the observed time-resolved spectrum is that of the impact-generated light.

The rate at which the entrance slit image traverses the film plane is 1 mm/ $\mu\text{sec}$ . Thus, the time required for the slit image to traverse its full length of 1.8 mm is 1.8  $\mu\text{sec}$ . Since any given point on the film is exposed only in the interval during which the entrance slit image crosses that point, the time resolution for this record is 1.8  $\mu\text{sec}$  (Smith, 1925; Seay, et al, 1961). The entrance slit of the streak camera was centered at the collision point and oriented with its length perpendicular to the direction of initial jet motion, i.e. parallel and in line with the expanding collision sheet. A projection of the entrance slit at the collision point extended over a 1.0 by 0.1 in. area and is indicative of the spatial resolution of the collected optical radiation.

The initial portion of the collision spectrum is seen to be a very intense continuum that lasts for some 5 to 6  $\mu\text{sec}$ . Recall that the framing camera record for this experiment, described above, shows an initial brilliant flash of light for about the same time interval. The continuum then appears to fade and a rich emission spectrum is observed. At about 10  $\mu\text{sec}$  a relighting phase commences, consisting of a continuum of lower intensity than the initial continuum. At about 13  $\mu\text{sec}$  after impact the continuum fully extends over the wavelength range covered. Finally, emission lines are seen to revert to absorption lines at later times.

The emission lines seen after 6  $\mu\text{sec}$  are shown below to be mainly

lines of neutral copper atoms. There is, in addition, conclusive evidence of ionized copper in the spectral range between about 4900 and 4950Å. A narrow band of light in this region is seen to emerge from the initial continuum. The intensity of this band increases at later times and subsequently blends into the reflight continuum. There are about twenty-five ionized copper lines in this spectral range (Shenstone, 1948). Since the wavelength resolution of the time-resolved spectrum does not allow these lines to be seen individually, they appear as an unresolved group 50 to 60Å wide. Further evidence indicating the presence of ionized copper in the jet collision products has also been obtained and is presented below.

Thus, high speed jet impact results in a varied and rich spectral history. Qualitative evidence exists for the presence of ionized and excited neutral atoms in the jet collision plasma. A detailed analysis of this time-resolved spectrum is presented in the following sections.



## Part II Analysis of Time-Resolved Spectrum

A study of the jet collision time-resolved spectrum of firing no. 109 was made. The spectrum is rich in detail and contains important information regarding the nature of the jet collision process. In particular an examination of the shapes and shift of several spectral lines in a time interval of importance was undertaken. The results of this study lead to a measurement of the time-varying neutral and ion particle density in the plasma.

Only a time interval from about 6 to 13  $\mu\text{sec}$  after impact was extensively investigated. Little information could be derived from the early continuum phase of the spectrum before 6  $\mu\text{sec}$  since the film record was greatly overexposed. The later portions of the record after 13  $\mu\text{sec}$  were not considered since as will be shown later the collision of the expanding plasma with the vacuum chamber wall would occur at these times and hence would greatly complicate the analysis of the observed spectrum.

Radiation observed by the time-resolved spectrograph originates from a particular volume element in the collision event as will be shown later. The projection of the spectrograph entrance slit onto the object plane at the impact region determines the cross-sectional dimensions of this volume. The effective depth of the radiating volume is small in comparison with the overall size of the collision region. Light from interior points of the collision region is strongly absorbed upon passage through the intervening material and does not contribute significantly to the emerging radiation. Only a thin section located near the front of the expanding products is effective in producing the observed light. Thus the particle density measurements derived from the time-resolved spectral

data represent spatial mean values for this thin region under observation. The above mentioned time resolution of the spectrograph will introduce a further modification; that is, the numerical density estimates will be averaged in time as well as in spatial position.

## 2.1 Spectral Line Identification

Densitometer scans of the time-resolved spectrum at two time intervals after initial impact, and of the copper reference spectrum are shown in Fig. 15. Each scan of the collision spectrum is seen to consist of a background continuum with superposed emission lines. The increased intensity of the continuum at 11.5  $\mu$ sec corresponds to the relight phase of the spectral record. About sixteen prominent emission peaks can be distinguished at both time intervals, all of which have rather broad profiles, typically of the order of 10 to 20 Å wide. Comparison of these with the densitometer scan for the copper reference spectrum illustrates the relatively large breadth of these lines. Both the background continuum and emission lines persist throughout the time interval from 6 to 13  $\mu$ sec.

With the aid of the calibration spectra on the film record these emission lines have been identified mainly as neutral copper transitions and are tabulated in Table IV. All known prominent transitions of neutral copper for the spectral range covered in this experiment were observed. Due to the width of the spectrum lines and the limited wavelength resolution of the system, however, some of the expected lines are not completely separated. This is reflected in Table IV by showing a number of neutral copper transitions in close proximity to the observed lines. The upper

level designation and excitation energy (Moore, 1952) for the spectral lines with the highest tabulated intensities (Shenstone, 1948) are also shown in the table.

The presence and growth of ionized copper lines is most effectively illustrated in the spectral region between 4900 and 4950A, as noted previously. At 6.7  $\mu$ sec there is little evidence for any characteristic ion transitions in this spectral region, whereas at 11.5  $\mu$ sec a pronounced increase in intensity above the background continuum is most obvious. This increased intensity represents the growth of an unresolved group of about twenty-five copper ion lines in the 50A wide region. Also the similar appearance and growth of other ion transitions can be seen in the vicinity of the CuI 4651 transition. At 11.5  $\mu$ sec a distinct hump in this line is apparent, as indicated in Fig. 15. This satellite growth is the result of three known copper ion lines at about 4660A. Spectral lines profiles of this emission line presented later will show the growth of these ionized lines more distinctly.

An energy level diagram that contains the more intense spectral transitions given in Table IV is given in Fig. 16. Also included are the observed groups of copper ion lines. Several indicated transitions in this figure are of concern in the work presented below. A large number of both neutral and ion energy levels are seen to have been excited. For the neutral copper lines, some of these levels are as high as or slightly above the copper first ionization potential at 7.7 ev (Moore, 1952).\*

---

\*Levels that appear above the ionization potential are associated with the anomalous term or two-electron excitation configuration of the copper atom, (Shenstone, 1932; White, 1934; Herzberg, 1937). These anomalous terms are grouped towards the right in the portion of Fig. 16 that corresponds to neutral copper. The normal terms appear below the ionization potential, (i.P.), at 7.7 ev.

For the observed ion lines, the corresponding upper energy levels are about 25 eV above the ground state of neutral copper. Other energy levels for both neutral and ionized copper could not be observed since the light resulting from transitions out of these levels does not lie within the spectral range of the time-resolved spectrograph.

## 2.2 Spectral Line Profiles from Time-Resolved Spectrum

A number of profiles for the prominent emission lines in the time-resolved spectrum were derived from the densitometer traces. The film record was scanned at 1  $\mu$ sec intervals, from 5.7 to 12.7  $\mu$ sec after first impact light. Typical densitometer scans were previously shown in Fig. 15. Horizontal position on each film scan is related to the wavelength. The wavelength calibration was established for each record using the wavelength identifications previously given in Table IV. Vertical displacement on each scan is proportional to photometric density units. A density scale calibration was established by inserting calibrated neutral density filters into the optical train of the densitometer and recording the corresponding response.

To obtain the profile of a given emission line the measured densities were first converted to intensity values by means of a photometric film emulsion calibration described in Appendix C. The background continuum level for each densitometer scan was established at wavelength regions in which emission lines were absent and this background level, after being converted to intensity was subtracted from the total observed intensity.

### (a) Photographic Intensity Calibration

Several Hurter and Driffeld (H-D) emulsion calibration curves relating density with relative intensity at certain wavelengths were experimentally determined for the Tri-X emulsion and the developing process used to obtain the time-resolved film records. A description of the calibration technique and experimental results are given in Appendix D. A rotating step-sector wheel method was employed. A light source and step-sector wheel were mounted in front of the direct-vision prism and streak camera entrance optics. The interrupted light was recorded with the streak camera after being dispersed by the direct-vision prism. Zinc, mercury-cadmium, and helium spectral lamps were used as light sources. Emulsion calibration curves were constructed at discrete wavelengths for the various spectral lamp sources. The results were checked for self-consistency as suggested by Sawyer and Vincent, (1943). These emulsion calibration curves were found to be in agreement with similar measurements of other investigators, (Kodak, 1962; Pressman, 1962). Values for the slope of the emulsion calibration curve,  $\gamma$ , found from repeated photometric measurements at several wavelengths are given in Table V. The average value of  $\gamma$  is  $1.0 \pm 0.1$  for the wavelength range studied. This value was used in all spectral line profile calculations.

### (b) Measurement of Spectral Line Profiles

Horizontal and vertical position measurements on a densitometer record were obtained with the use of a Gerber Scanner and punched onto cards for subsequent analysis. At a given wavelength position vertical displacements corresponding to both the total density and to the background continuum were measured. Approximately fifty to one hundred points

were used to reproduce a line profile. In addition, the vertical displacements of the photographic density calibration steps on the densitometer record were recorded. This information was used to establish a vertical height to density scale calibration. For a wavelength scale calibration, the horizontal positions at the maximum points of each prominent emission line were also recorded.

Spectral line profiles were constructed from these densitometer measurements. A listing of the IBM 1620 Fortran program together with a brief description and the results of a typical calculation are given in Appendix C. It was found in all cases that the observed density values fell within the linear portion of the emulsion calibration curve. Hence a density value,  $D$ , and its corresponding relative intensity,  $J$ , are related by, (Mees, 1946; Sawyer, 1951)

$$D = \text{const} + \gamma \log J \quad (2-1)$$

where  $\gamma$  is the slope of the emulsion calibration curve in the linear region. Equation (2-1) was then used to evaluate the relative background and total intensities,  $J_B(\lambda)$  and  $J_T(\lambda)$  respectively, at the given wavelength,  $\lambda$ . That is,

$$J_B(\lambda) = \text{const} \times 10^{D_B/\gamma} \quad (2-2)$$

$$J_T(\lambda) = \text{const} \times 10^{D_T/\gamma} \quad (2-3)$$

where  $D_B$  and  $D_T$  are the corresponding density values. The spectral line intensity,  $J(\lambda)$ , is simply the difference between the total and background intensities

$$J(\lambda) = \text{const} \left\{ 10^{D_T/\gamma} - 10^{D_B/\gamma} \right\} \quad (2-4)$$

It was found convenient to normalize the line intensities to the maximum computed value  $J_0$  at a wavelength  $\lambda_0$  for the spectral line under study, and also to deal with wavelength deviations,  $\epsilon$ , from the wavelength of the maximum, viz.

$$\epsilon = \lambda - \lambda_0 \quad (2-5)$$

Thus the spectral line profile program yields the relative line intensity,  $J(\epsilon)/J_0$ , at a wavelength deviation,  $\epsilon$ , for each emission line on a given densitometer trace.

### 2.3 Line Broadening Mechanisms

In general, a number of causes result in the broadening of a spectral line. They can be classified as follows, (Mitchell and Zemansky, 1934; White, 1934; Aller, 1953; Penner, 1959; Breene, 1961).

- A. Doppler broadening
- B. Foreign atom collision broadening
- C. Natural line breadth
- D. Resonance broadening
- E. Stark broadening
- F. Instrumentation broadening

The first two phenomena can be disregarded as giving rise to the observed broadening for this work since their contributions to the line width are inconsequential. Doppler broadening effects due to the thermal motion of the emitting atoms are usually small and limited to the narrow center or core of the spectral line. The halfwidth of a Doppler-broadened line is proportional to the square root of the temperature of the

radiating gas. A Doppler halfwidth of the order of several angstroms observed for the copper spectrum lines in the time-resolved spectrum would imply an unrealistically high temperature of  $10^7 - 10^8$  °K. Also, in view of the low density of foreign atoms in the vicinity of the jet collision, (the residual helium gas in the vacuum chamber), foreign atom collision broadening is extremely small and is thus ineffective in producing the large observed line widths.

The natural line breadths for most of the observed copper transitions have also been shown to be comparatively small, (Allen, 1932). However several copper lines are known to possess unusually large natural widths, of the order of 1Å, due to autoionization of the upper energy level of the spectral transition, (Shenstone, 1932). A few of these lines appear in the time-resolved spectrum and their observed halfwidths may be due in part to their large natural line width.

In the presence of atoms that are identical to the emitting atoms a spectral line will be resonance or self-broadened. This type of broadening, due to the strong interaction between an emitting atom and its nearby perturbing atoms, can result in line breadths of the order of the observed breadths if the density of identical atoms is sufficiently high.

Similarly, Stark broadening, due to the intermolecular electric fields of electrons and ions in the collision plasma, must also be considered since Stark-broadened lines are also known to possess broad profiles. In addition, a wavelength displacement of a spectral line can occur due to the Stark splitting and shift of the energy levels of the transition under the influence of the intermolecular electric fields.

Finally, distortions or modifications of a spectral line profile



due to the spectrographic instrumentation must be taken into account.

It will be shown in the following sections that the principal mechanism giving rise to the observed spectral line shapes is resonance-broadening. This is achieved by matching resonance-broadened line profiles to several neutral copper transitions in the time-resolved spectrum of firing no. 109, where modification of the form of the resonance profile due to spectrographic instrumentation has been included.

#### (a) Resonance-Broadened Line Profiles

The profile of a resonance-broadened spectral line as derived from either line broadening impact theory or statistical theory is given by the Lorentz formula, (Margenau and Watson, 1936; Breene, 1961)

$$J(\nu) = \text{const}/((\nu-\nu_0)^2 + (A/2)^2) \quad (2-6)$$

where  $\nu_0$  is the frequency at the center of the symmetrically-broadened line and  $A$  is the halfwidth of the line in frequency units.\* Normalizing the intensity  $J(\nu)$  to its maximum value  $J(\nu_0)$

$$J(\nu)/J(\nu_0) = (A/2)^2/((\nu-\nu_0)^2 + (A/2)^2) \quad (2-7)$$

The halfwidth is linearly related to the number density of perturbing atoms of the same kind as the emitter,  $N$ , and to the oscillator strength,  $f$ , of the spectral transition as,

$$A = \text{const} (e^2 f / m \nu_0) N \quad (2-8)$$

where  $e, m$  are the electronic charge and mass respectively. The constant in eq (2-8) has been evaluated from both statistical and impact broadening

---

\*The term halfwidth as used here refers to the full width of the line at half of its maximum intensity.

theory. Comparative results given by Breene are shown in Table VI and are seen to be in close agreement.

#### (b) Instrumentation Broadening

Before attempting to fit resonance-broadened profiles to the emission lines in the time-resolved spectrum of firing no. 109 modifications due to the spectrographic instrumentation must be taken into account. In particular, if the image of the entrance slit is comparable in size to the actual spectral line width then the resultant line profile will be influenced by the characteristics of the spectrograph. Consider a spectrograph entrance slit of finite width irradiated by a light source that contains several discrete frequency components  $\nu_i$ . If the slit is of sufficient width so that diffraction effects can be neglected then slit images of width  $\Delta_i$ , will appear in the image plane of the spectrograph at positions corresponding to the frequencies  $\nu_i$ . The light intensity of the  $\nu_i$ -component will be zero outside of each strip  $\Delta_i$  and of magnitude  $J(\nu_i)$  within the strip, (Baly, 1905; Slater, 1925; Forsythe, 1932; Clark, 1960; Brügel, 1962). If there is no overlapping of slit images then the distribution of light intensity along the image plane is simply described by the array of strips of width  $\Delta_i$  and intensity  $J(\nu_i)$ . When the several slit images overlap, the component intensities are superposed. The resultant light intensity at a frequency  $\nu$  in the region of overlap is

$$\Phi(\nu) = \sum_i J(\nu_i) H(\Delta_i/2 + (\nu_i - \nu)) H(\Delta_i/2 - (\nu_i - \nu)) \quad (2-9)$$

where  $H$  is the unit step function. The summation extends over the number of intensity components whose slit image width includes the frequency position  $\nu$ . In the limit as the number of spectral components

increases indefinitely, the resultant intensity becomes (Dalton, 1963)

$$\bar{I}(\nu) = \int_{\nu-\Delta/2}^{\nu+\Delta/2} J(\nu') d\nu' \quad (2-10)$$

Thus the resultant light intensity at a given frequency is simply the integrated or average intensity over a narrow frequency band.\*

The modification of a resonance-broadened profile is obtained by evaluating eq (2-10) where the intensity distribution of the light source  $J(\nu')$  is given by the Lorentz formula, eq (2-7). The resultant integrated Lorentzian function is

$$\begin{aligned} \bar{I}(\nu) = J(\nu_0)(A/2) \left\{ \tan^{-1} \left\{ \frac{\nu-\nu_0 + \Delta/2}{A/2} \right\} \right. \\ \left. - \tan^{-1} \left\{ \frac{\nu-\nu_0 - \Delta/2}{A/2} \right\} \right\} \end{aligned} \quad (2-11)$$

---

\*Equation (2-10) can be expressed in a more general form as

$$\bar{I}(\nu) = \int S(\nu, \nu') J(\nu') d\nu' \quad (2-10a)$$

The slit function  $S(\nu, \nu')$  represents the weighted contribution to the resultant intensity at the frequency  $\nu$  from radiation of frequency  $\nu'$ , (Dennison, 1928; Nielsen, et al, 1944; King and Emslie, 1951; Brodersen, 1953; Penner, 1959). Triangular and trapezoidal slit function shapes are commonly used for spectrographs with both entrance and exit slits. Gaussian shapes are used to approximate diffraction effects associated with small slits. A rectangular slit function shape representing a limiting form of a trapezoidal shape is useful for spectrographs with only an entrance slit. A rectangular slit function

$$\begin{aligned} S(\nu, \nu') &= 1 & \nu-\Delta/2 < \nu' < \nu+\Delta/2 \\ S(\nu, \nu') &= 0 & \text{otherwise} \end{aligned}$$

has been used in this work.

Normalizing  $\Phi(v)$  to its maximum value  $\Phi(v_0)$  one has

$$\frac{\Phi(v)}{\Phi(v_0)} = \frac{\tan^{-1} \left\{ \frac{v-v_0 + \Delta/2}{A/2} \right\} - \tan^{-1} \left\{ \frac{v-v_0 - \Delta/2}{A/2} \right\}}{2 \tan^{-1} \left\{ \frac{\Delta}{A/2} \right\}} \quad (2-12)$$

The halfwidth of the integrated Lorentzian profile  $\delta$ , evaluated directly from eq (2-12), is found to be

$$\delta^2 = \Delta^2 + A^2 \quad (2-13)$$

Thus the use of a finite-width entrance slit will alter the shape of a resonance-broadened profile and further increase the observed line half-width.

If two or more resonance broadened lines are not completely resolved the resultant profile is described by

$$\begin{aligned} \Phi(v) = \sum_i J(v_i) (A_i/2) \left\{ \tan^{-1} \left\{ \frac{v-v_i + \Delta/2}{A_i/2} \right\} \right. \\ \left. - \tan^{-1} \left\{ \frac{v-v_i - \Delta/2}{A_i/2} \right\} \right\} \end{aligned} \quad (2-14)$$

where  $A_i$  is the halfwidth,  $v_i$  the center frequency of the  $i$ th partially resolved line, and  $J(v_i)$  represents the relative intensity of the  $i$ th component. The summation includes all the partially resolved broadened lines that can contribute to the resultant line profile.

The width of the slit image is related to the entrance slit width and the optical parameters of the spectrograph. Evaluations of the slit image width have been made for the direct vision prism-streak camera combination, details of which are presented in Appendix E. Essentially what is done is to construct an image of the entrance slit by following the path of several principal rays through the optical system. This is

repeated at several wavelengths in the spectral range covered by the time-resolved spectrum to obtain the variation of slit image width with wavelength. The results of the calculations are illustrated in Fig. 17. Two families of curves are shown which correspond to slightly different values of the entrance slit width. Changes in the slit image width as a result of small deviations about the nominal angle of incidence are also included.

Experimental values of the slit image width have been independently determined from integrated Lorentzian profile fits to several lines in the time-resolved spectral record as described below, and are indicated in the figure. The accuracy of the slit image widths determined in this manner is limited by the sensitivity of the line profile fitting process, (see section 2.5). Uncertainties in slit width values are indicated by the error flags in Fig. 17. In view of the fact that nominal values for the optical parameters of the direct vision prism-streak camera combination were used in the calculations, the agreement between the calculated and experimental values is good.

#### (c) Line Profile Fits to Selected Transitions

Integrated Lorentzian profiles were matched to several of the observed neutral copper lines in the time-resolved spectrum. This established that resonance broadening is the principal mechanism responsible for the breadth and shape of the spectral lines. These profiles were computed from either eq (2-12) or eq (2-14). Fortran listings of the programs for both the single component and multicomponent profiles are given in Appendix F, together with a brief description of the programs.

The procedure for calculating a single-component line profile is as follows. A time in the spectral record for which the observed line half-width is smallest is first examined. The resonance halfwidth,  $A$ , is then computed from eq (2-13) for an assumed slit width  $\Delta$ , and an assumed total halfwidth  $\delta$ . A line profile described by eq (2-12) is then constructed. By appropriately varying both the slit width and total half-width values, a profile that best matches the observed line shape is generated. This results in a measure of the slit width at the wavelength under consideration and an evaluation of the true resonance halfwidth of the line at the particular time studied. Line profile fits for the same line at other times are then achieved by varying just the total halfwidth, keeping the slit width fixed, until a best match with the observed line shape is obtained.

If contributions to the observed line shape due to partially resolved neighboring lines are taken into account, a multicomponent line profile given by eq (2-14) is employed. In this case values for the resonance halfwidth  $A_i$ , and relative intensity  $J(v_i)$ , of each spectral line that contributes to the observed line are needed. First estimates for these quantities are established by matching a single-component line profile to the most prominent spectral line. The difference between the observed line shape and the single-component profile fit indicates the relative amplitude and width of the nearby partially-resolved line or lines. A line profile is then constructed with these data. Appropriate variations in all the resonance halfwidth and relative intensity values are then made in order to generate a profile that best matches the observed line shape.

### Single-Component Profiles

Integrated Lorentzian fits to the observed transitions CuI 4587, 4651 and 5153 were generated in the above manner, at 1  $\mu$ sec intervals over a time period from about 6 to 13  $\mu$ sec after initial jet impact. The CuI 4587 line was specifically chosen since there are no nearby transitions of neutral or ionized copper in the wavelength region of the observed broadened line. Hence a single-component integrated Lorentzian profile fit is most appropriate for this line. However, the natural width of the CuI 4587 transition is known to be relatively large due to autoionization of its upper level, (Allen, 1932; Shenstone, 1932). Thus, the observed line profile, aside from instrumentation broadening, is the result of a combination of natural broadening and resonance broadening interactions.

The CuI 4651 line was considered next since it is a component of the same multiplet as the CuI 4587 transition, but is associated with an upper energy level that does not exhibit autoionization. Thus, natural broadening of this line has little influence on the overall observed line shape. Although several partially resolved copper lines are present and spaced about 10A on both sides of the CuI 4651 line, only single-component integrated Lorentzian profile fits were performed. In determining the best match to the observed line shape in this case, attention was directed towards the fitting over a wavelength region that encompassed no neighboring lines rather than the overall line shape.

Integrated Lorentzian profiles to the CuI 5153 line were also made. This transition was specifically chosen since it originates from a lower energy level and involves a configuration in which only one electron is involved in an optical transition as distinct from the two-electron

configuration of the previous two lines. As with the CuI 4651 line, the best fit determination was made over wavelength regions that contained no nearby partially-resolved spectral lines. For all three lines the slit width contribution to the observed line shapes was first established as previously indicated. Values of the slit widths determined and used in these profile fits were shown in Fig. 17.

The integrated Lorentzian fits to these lines are presented in Figs. 18, 19, and 20. Observed line shapes in the time-resolved spectrum are represented by the data points while the solid curves show the fitted integrated Lorentzian profiles. The corresponding time after initial jet impact is shown in each figure. The relative position and amplitudes of known spectral transitions of copper that fall within the spectral range studied are also indicated.

The integrated Lorentzian profiles shown in Fig. 18 adequately represent the observed CuI 4587 line shape over the time interval studied. Irregularities in the observed line shapes at the later time intervals are believed to be the result of impact of impact between the expanding jet collision sheet and the vacuum chamber window.

The observed CuI 4651 line shapes and corresponding integrated Lorentzian profiles shown in Fig. 19 are also seen to be in good agreement over a substantial portion of the theoretical line profile. Of particular importance is the appearance and growth of three ionized copper transitions, (CuII 4660, 4661, 4663), which are present as an unresolved cluster in the observed line shapes. The relative intensity of these unresolved lines is seen to increase rapidly at the later times. The appearance of the partially resolved CuI 4643 line during early times is also of interest.



Contributions from this transition to the observed line profiles are considered in the following section.

The observed line shapes for the CuI 5153 transition shown in Fig. 20 are also seen to be adequately represented by an integrated Lorentzian profile. Contributions to the line shape from nearby broadened neutral and ion spectral lines are not as pronounced as in the case of the CuI 4651 line.

Part (a) of Table VII lists values of the resonance-broadened half-width  $A$ , obtained from the above integrated Lorentzian profile fits. Accuracies for the halfwidths found by this procedure are limited by the sensitivity of the line fitting process and are of the order of  $\pm 10$  percent, (see section 2.5).

#### Multicomponent Profiles

Single-component profile fits to the CuI 4651 transition shown in Fig. 19 indicate that the partially resolved CuI 4643 line noticeably contributes to the observed line shape at early time intervals. Fits to the observed line shapes with a multicomponent profile fit that included both the CuI 4643 and 4651 transitions were made. Values for the resonance halfwidth of the CuI 4651 line determined from the above single-component profile results were initially used. Estimates for the resonance halfwidth and relative intensity of the CuI 4643 line were first obtained from a comparison of the single-component profiles and the observed line shapes. By appropriate variations of the resonance-broadened halfwidth values and relative intensity a best match to the observed line shape over an extended wavelength range was achieved. Multicomponent fits at 5.7, 6.7, and 7.7  $\mu\text{sec}$  were made, the resulting fit at

6.7  $\mu\text{sec}$  is shown in Fig. 21. Agreement between the observed line shapes and the fitted curves is good in all three cases. The resonance-broadened halfwidth values and relative intensities for the CuI 4643 and 4651 transitions used to obtain the best multicomponent profile match are listed in Table VII, part (b) and Table VIII respectively. The intensity of the CuI 4651 line was arbitrarily chosen as unity in all three profile fits.

Resonance-broadened halfwidths for several other observed lines in the time-resolved spectrum have also been obtained from further multicomponent line fits. Halfwidth values and relative intensities for the partially resolved components CuI 4525, 4531, and 4540 at three times are also shown in part (b) of Table VII and in Table VIII. The relative intensity of the principal CuI 4540 line was taken as unity. The resultant multicomponent fits to the observed line shapes are shown in Figs. 22 and 23. The study of these lines is of importance in subsequent work and is discussed in the following sections.

In conclusion, an integrated Lorentzian profile has been shown to adequately represent the shape of a number of broad and overlapping lines in the time-resolved spectral record. When the natural line breadth can be neglected, the observed line breadths are the results of a combination of instrument broadening and resonance broadening. Slit image widths obtained from these line fits have been previously shown to be in agreement with calculated slit width values.

#### (d) Influence of Plasma Ions on Spectral Characteristics

The presence of charge particles in the jet collision plasma will influence the nature of the spectral line radiation in general as a broadening and shift of a spectral line. These effects are related to the

Stark splitting and displacement of the energy levels of the spectral transition. The splitting and shift are in turn a consequence of the fluctuating intermolecular electric fields created by the charged particles in the vicinity of the emitting atom. The Stark effect for several neutral copper transitions in the wavelength region under consideration is known. The pattern and magnitude of the line splitting with an applied electric field has been measured by Takamine (1919), some results of which are given in Table IX. Three of the lines are split into two components asymmetrically displaced with respect to the original wavelength.

An atom in an excited state is influenced simultaneously by collisions with both identical neutral atoms and charged particles in the jet collision plasma. Thus the spectral line profile for the transition from this excited state will in general reflect both broadening effects and would be described in a complicated way by the resonance and charged particle interactions. Previous results however have shown that instrumentation and resonance-broadening are the predominant mechanisms affecting those lines studied; in particular, line profile fits to the Cu I 5153 transition, which exhibits a Stark splitting and thus could be expected to show Stark broadening, were given in Fig. 20. Hence superposed Stark broadening contributions in the time-resolved spectrum are not apparent. This result is not surprising in view of the magnitude of the Stark splitting for this spectral line. Comparative Stark splitting for hydrogen for which Stark broadening effects have been well established. (Edels and Craggs, 1951; Griem, 1954; Henkel, 1954; Margenau and Lewis, 1959) are several orders of magnitude greater than the Stark splitting for copper. Alyamovskii and Kitaeva (1959), have experimentally generated ionic

Stark-broadened  $H_{\beta}$  lines with a halfwidth of about 50Å corresponding to an intermolecular electric field of the order of 100 kv/cm. Similarly Holtsmark and Trumpp (1925), have found Stark-broadened halfwidths of about 1Å with an intermolecular field of the order of 25 kv/cm for the CuI 4023 and 4062 transitions. The magnitude of the Stark splitting for these copper lines is larger than that for the lines shown in Table IX by approximately a factor of ten. Hence line broadening contributions due to ions and electrons in the jet collision plasma are expected to be negligibly small for all the observed lines compared to the predominant resonance and instrumentation broadening.\*

The asymmetric splitting of the transitions given in Table IX suggest that line shifts may be present in the observed spectrum. Since these lines are instrument and resonance-broadened the individual Stark components are not resolved. However superposition of the shifted Stark components will result in a spectral line profile that has a net wavelength displacement in the direction of the Stark component shifts. The net spectral line shift can then be related to the component splitting and hence to an estimate for the intermolecular electric field that is responsible for the observed shift. Evidence for a net wavelength shift affords an excellent example of the influence of charged particles on the observed jet collision spectrum since resonance-broadened lines exhibit no wavelength shift (Margenau and Watson, 1936; Foley, 1946). Thus in contrast to the situation for line broadening, resonance interactions and charged particle effects are decoupled in a line shift measurement.

---

\*Further evidence for this conclusion is contained in the results of the next section.

Of the several lines given above for which Stark effect information is known the CuI 4531 line appeared to be the best choice for further study. This line occurs as a partially resolved component of the CuI 4540 transition along with another nearby line, CuI 4525. No Stark effect data has been given by Takamine for these companion lines. It is presumed that the Stark splitting for these lines is much smaller than that for the CuI 4531 line, and hence was not observed in Takamine's experiments.\* With the assumption that these companion lines exhibit negligible shift in the time-resolved spectrum, the position and shift of the resonance broadened CuI 4531 line with respect to these two adjacent lines can be measured. Furthermore, due to the close proximity of these three lines a line shift measurement would be unaffected by the uncertainty and error in the wavelength scale associated with the observed spectral records.

For the CuI 5153 transition no nearby comparison lines were found in the spectral data. Hence a line shift determination over extended wavelength intervals would be necessary and consequently significant wavelength scale errors would be included in a line shift measurement. The CuI 5218, 5220 transitions which appear as one unresolved emission line on the spectral record, were not considered since Stark effect data for CuI 5220 appears incomplete.

The resonance-broadened CuI 4531 line was split into its two Stark components, both of which were shifted in the direction of higher wavelengths. If  $\lambda_p$  and  $\lambda_n$  represent the two Stark component wavelengths

---

\* Other Stark-effect experiments at slightly higher electric fields were performed by Nagaoka and Suglura (1924), Fujioka and Nakamura (1927), but were restricted to wavelengths below about 4100Å.

and  $\lambda_o$  the original wavelength, then assuming a linear Stark shift for this transition

$$\begin{aligned}\lambda_p &= \lambda_o + C_p F \\ \lambda_n &= \lambda_o + C_n F\end{aligned}\tag{2-15}$$

where  $C_p$ ,  $C_n$  are the respective line shifts per unit electric field and  $F$  is the electric field at the emitting atom.

The mean displacement can be conveniently expressed as

$$\delta_s = (\lambda_p + \lambda_n)/2 - \lambda_o\tag{2-16}$$

or

$$\delta_s = (C_p + C_n)F/2\tag{2-17}$$

The separation of the Stark components is simply

$$d = \lambda_p - \lambda_n\tag{2-18}$$

or

$$d = (C_p - C_n)F\tag{2-19}$$

Hence the ratio of component separation to mean displacement is

$$d/\delta_s = 2(C_p - C_n)/(C_p + C_n)\tag{2-20}$$

For a quadratic Stark shift of the CuI 4531 line one has

$$\begin{aligned}\lambda_p &= \lambda_o + K_p F^2 \\ \lambda_n &= \lambda_o + K_n F^2\end{aligned}\tag{2-15a}$$

where  $K_p$ ,  $K_n$  are the respective line shifts per unit electric field squared for the p- and n- Stark components. The resultant ratio of component separation to mean displacement is of a similar form to that of eq (2-20), namely

$$d/\delta_s = 2(K_p - K_n)/(K_p + K_n)^* \quad (2-20a)$$

In fitting an observed spectral profile, the CuI 4531 line was split and shifted in accord with the above relations. The wavelength positions of the CuI 4525 and 4540 transitions were unaltered. A multicomponent Lorentzian profile match to the observed profile at several times was made. The procedure used in fitting the line profiles was as follows. A single-component fit was first matched to the principal CuI 4540 line over a wavelength region that included no partially resolved components. This resulted in a first estimate for the CuI 4540 halfwidth. Comparison of the observed line shape and this single-component fit indicated the contributions of the partially resolved CuI 4525 and 4531 components to the observed profile. Initial estimates of the relative intensities and halfwidths for these two components were then made from this comparison. A multicomponent fit to the observed line profile was made using these initial estimates. The CuI 4531 line was shifted and split into two components, each having the same halfwidth as determined above. The relative intensities of the  $\lambda_n$ - and  $\lambda_p$  lines were taken in the ratio of two to one since a Stark split n-component has double the statistical weight of a p-component, (Greenstein, 1960).

By varying the resonance-broadened halfwidth values for all the lines, the relative intensities of the CuI 4525 and 4531 components, and the line splitting and shift of the CuI 4531 transition, a best fit to the observed line shape was achieved. Resonance halfwidth values and

---

\* From Takamine's data in Table IX this ratio is for the CuI 4531 line numerically  $d/\delta_s = 2/7$ .

relative intensities for these spectral lines used to obtain the best profile match were previously given in Table VII, part (b) and Table VIII respectively. Final values of the mean shift  $\delta_s$ , and component separation  $d$ , for the CuI 4531 line used in the profile fits are shown in Table X. The resultant multicomponent profiles at 5.7 and 6.7  $\mu\text{sec}$  were shown above in Figs. 22 and 23. For comparison, spectral line profiles in which the CuI 4531 line was not split or shifted in wavelength are presented in Figs. 24 and 25. The shift in the observed CuI 4531 line at each time interval is most obvious in these comparative profiles. Thus the observed wavelength displacements can be attributed to a Stark effect that results from an intermolecular electric field created by charged particles in the jet collision plasma.

#### 2.4 Neutral Atom and Ion Density Estimates

Estimates of the neutral copper atom density in the jet collision plasma can be obtained from the resonance-broadened line-halfwidth measurements. The linear dependence of a line halfwidth on the neutral particle density discussed previously will be used in the calculations. Observed spectral lines whose upper energy level is effected by autoionization and hence exhibit a large natural line width will not be considered. In addition, oscillator strengths for two of the spectral lines studied will be obtained from their measured halfwidths. This is of particular importance since experimentally determined oscillator strengths for excited transitions of copper are relatively scarce.

Observed Stark wavelength shifts lead to estimates of the density



of copper ions in the plasma. Results of Stark broadening theory will be used to obtain the number density of copper ions and electrons in the jet collision plasma.

(a) Calculation of Neutral Atom Density

Halfwidth values of the CuI 5153, 4651, and 4531 spectral lines were used to calculate the neutral copper atom density in the collision plasma. The relation between the neutral particle density and a resonance-broadened line-halfwidth was previously given in eq (2-8), with numerical values of the constant in the equation shown in Table VI. Although there are small differences between the values of the constant, Margenau and Watson's statistical result was considered to be appropriate for further calculations. This choice is preferable since in evaluating the constant a linear halfwidth-neutral particle density relation was shown to be a natural consequence of a statistical theory and requires no assumption of an optical collision diameter, as in the impact theories. Furthermore, in view of the high particle densities that will be shown to result from the application of eq (2-8), frequent close encounters between emitter and perturber particles occur and hence a statistical line theory is appropriate.

A resonance-broadened line-halfwidth and neutral atom density are from eq (2-8) related as\*

$$A = \frac{\pi}{3} (e^2 f / m v_o) N = \frac{\pi}{3} (e^2 f \lambda_o / m c) N \quad (2-21)$$

For the calculations reported here the consistent set of oscillator strengths given by Corliss and Bozman (1962) for the CuI 5153, 4651, and 4531 lines presented in Table XI were used. Halfwidth values for both

CuI 4651 and 4531 at 5.7, 6.7, and 7.7  $\mu\text{sec}$  after initial jet impact were taken from the multicomponent profile matches, part (b) of Table VII. At later times halfwidth values from single component fits were used for the number density calculations.

The resultant neutral copper atom densities obtained for each of the three spectral lines are listed in Table XII and also illustrated in Fig. 26. Error estimates included in the figure indicate the sensitivity of the line profile match in the determination of a halfwidth and do not reflect possible systematic errors in the measurements and data reduction techniques. Variations due to the fitting sensitivity are of the order of  $\pm 15$  percent. Further discussion of the uncertainties in these results is presented below in section 2.5. The overall agreement in the density estimates from these three spectral lines is good. Results derived from the CuI 5153 and 4651 halfwidths are especially close throughout most of the time interval studied. The neutral atom density in the jet collision plasma is seen to be of the order of  $4 \times 10^{19} \text{ cm}^{-3}$ .

The structure and radiative transport processes in the expanding jet collision sheet have been studied by Lukasik, et al (1964). The time variation of material density along the radius of the expanding sheet has been calculated from a fluid-dynamic model of the jet collision. Typical

---

\*For  $A$  in angstrom units one has numerically

$$A = (4.68 \cdot 10^{-6}) f \lambda_0^3 N \quad (2-21a)$$

where  $A(\text{angular frequency units}) = 2\pi A (\text{sec}^{-1})$  and

$$A(\text{angstrom}) = 10^8 A(\text{cm}) = \lambda_0^2 / c \times 10^8 \times A (\text{sec}^{-1})$$

profiles show a moderate increase in material density in a radially outward direction from the point of jet impact, i.e. the center of the expanding sheet. After reaching a maximum value at about 50 percent of the radial distance from the center to the front of the sheet, the density profile falls rapidly to zero at the front. Numerical solutions of the radiative transport equations using these density profiles and calculated optical opacity values were performed by Lukasik, et al. The results of these calculations indicate that the observed spectral radiation comes from a spatially narrow region between the expanding front of the collision sheet and the radial position of peak density. Thus the neutral copper atom densities measured from resonance-broadened halfwidths are indicative of conditions in this region.

A variation of the neutral atom density with time is apparent in Fig. 26. The particle density initially decreases until about 9  $\mu\text{sec}$  after jet impact and then increases. This feature of the spectral record is in accord with results of the fluid-dynamic model. In particular one can show that the front of the expanding sheet moves with a constant velocity. The calculated time of arrival of the expanding sheet at the vacuum chamber wall is 8.8  $\mu\text{sec}$  from jet impact. This is in excellent agreement with the observed time for a minimum atom density of about 9  $\mu\text{sec}$ . What is thought to occur physically is that after the expanding sheet strikes the chamber wall a compressive shock is reflected radially inward along the sheet. This inward-moving shock compresses the material in the sheet. The observed increase in neutral atom density after 9  $\mu\text{sec}$  is in agreement with this qualitative prediction. Furthermore, a wall collision will result in radiative recombinations of the excited jet

material and heating of the chamber wall, which would correspond to the onset of a background continuum during the relight phase. At the same time the increase in atom density leads to the copper absorption lines in the time-resolved spectrum (Fig. 14).

Since the observed halfwidths are governed by eq (2-21) coupling halfwidth measurements of other lines with the now known number densities can be used to determine transition probabilities. Oscillator strengths for the CuI 4643 and 4525 transitions have been determined in this manner. At a given time after jet impact the ratio of halfwidths for two resonance broadened lines  $\lambda_i$ ,  $\lambda_j$  can be expressed as, (see eq (2-21a))

$$A_i/A_j = f_i/f_j \times (\lambda_i/\lambda_j)^3 \quad (2-22)$$

If the oscillator strength of one of the lines is known then the oscillator strength of the second line can be obtained from this halfwidth ratio. The CuI 4651 transition was chosen as a reference line since its oscillator strength is known and its wavelength is close to the CuI 4643 and 4525 lines. Comparison line halfwidths were taken from part (b) of Table VII; the CuI 4651 oscillator strength was given in Table XI. Halfwidth ratios  $A_{4643}/A_{4651}$  and  $A_{4525}/A_{4651}$ , were calculated at the three times for which multicomponent profile fits were made. The oscillator strengths obtained for these lines are given in Table XIII. The three values indicated for each line are derived from the measured halfwidths at the three early times. A weighted mean oscillator strength for each spectral line is also shown in the table. The relative intensities of the observed spectral lines given in Table VIII, were used to weight the individual f-number values in determining the mean. This reflects the sensitivity of the fitting process in a determination of parameters that define a

resonance-broadened line profile.

(b) Calculation of Ion Density

The observed wavelength displacements of the CuI 4531 transition are due to a Stark splitting and shift of this line, a consequence of the intermolecular electric field that exists in the jet collision plasma. The resultant line shifts are a measure of this field strength which in turn is established by the density of charged particles in the plasma. Copper ions and hence electrons are known to exist in the jet collision products as evidenced by the appearance of characteristic ion lines in the time-resolved spectrum. Contributions to the intermolecular field from the low pressure helium gas in the vacuum chamber which may have been partially ionized by collisions with the expanding jet plasma are extremely small in view of the low helium density and the high copper ion density found to exist in the plasma.

Consider an emitting (neutral) atom in the presence of a number of perturbing ions and electrons. The net electric field at the position of the emitter is the sum of individual contributions from all particles. For every charged particle configuration there will be a corresponding net electric field strength. By virtue of the motion of these charges their positions will change with time and so also will the value of the electric field strength. As a result there is a probability distribution for the field at the emitter; Stark splitting and shifts will be governed by this distribution. Each Stark component of a spectral line will be broadened and displaced in accord with the local field distribution. In the absence of other broadening mechanisms the sum of the contributions from each Stark component will form the total line profile. If the Stark

component lines are symmetrically displaced about the center wavelength, (as is the case for hydrogen), then the line profile will only be broadened by the presence of charged particles. On the other hand if the pattern of the Stark splitting is asymmetric about the center wavelength the total line shape will indicate in addition a wavelength displacement determined by the form of the electric field distribution.

#### Holtzmark Theory-Linear Stark Effect

Holtzmark (1919, 1924) first derived a probability distribution from a statistical theory for the electric field strength at the emitter due to the presence of nearby ions.\* If  $F$  represents the magnitude of the field and  $F_0$  an average field strength given by

$$F_0 = 2.61 e N_i^{2/3} \quad (2-23)$$

where  $e$  is the electronic charge in cgs units and  $N_i$  the number density of ions then the Holtzmark distribution, usually represented as  $W(\beta)$ , can be expressed as a function of the dimensionless ratio,

$$\beta = F/F_0 \quad (2-24)$$

Tables, graphs and asymptotic representations of the function  $W(\beta)$  can be found in the literature (Margenau and Lewis, 1959; Greenstein, 1960; Breene, 1961). Under the influence of this electric field distribution each Stark component of a spectral transition will be shifted to various frequencies in accord with the probability function  $W(\beta)$ . If  $\Delta\nu_0$  is the shift due to the average field  $F_0$  then for a linear Stark effect

---

\*For most physically realizable plasma densities and temperatures, including that plasma reported here, electron effects cannot be treated by a statistical theory but are described by an impact theory, (Margenau, (1959)).

where

$$\Delta\nu = C_i F \quad (2-25)$$

one has

$$\Delta\nu/\Delta\nu_0 = F/F_0 = \beta \quad (2-26)$$

$\Delta\nu$  is the frequency difference from the normal position of the line and  $C_i$  is the Stark displacement per unit electric field for the  $i$ th Stark component of a line. The spectral line intensity distribution  $J(\Delta\nu)$ , is given in terms of the Holtsmark function as (Henkel, 1954; Griem, et al, 1959; Penner, 1959; Greenstein, 1960)

$$J(\Delta\nu) = \sum_i \frac{S_i}{C_i} W\left(\frac{\Delta\nu}{C_i}\right) \quad (2-27)$$

where  $S_i$  is the relative intensity of the  $i$ th Stark component. The peak of each component will be displaced by an amount

$$(\Delta\nu)_i / C_i F_0 = \beta_{\max} \quad (2-28)$$

where  $\beta_{\max}$  is the value of  $\beta$  for which  $W(\beta)$  is a maximum. Thus for a spectral line with only two Stark components the mean line shift is

$$\delta_s = \frac{1}{2} \{ (\Delta\nu)_p + (\Delta\nu)_n \}$$

or

$$\delta_s = \frac{1}{2} (C_p + C_n) F_0 \beta_{\max} \quad (2-29)$$

A value for the average electric field can be obtained from a measured shift  $\delta_s$ . The ion density corresponding to this field strength can then be calculated from eq (2-23). Copper ion densities in the jet collision plasma were computed in this manner from the measured line shifts of the CuI 4531 line given in Table X.\* The results shown in Table XIV

---

\*A value of  $\beta_{\max}$  of 1.5 was used for the calculations (Breene, 1957)

Indicate that ion densities of the order of  $5 \times 10^{18} \text{ cm}^{-3}$  are obtained from such a treatment of linear Stark displacements using Holtsmark's theory.

#### Folded Distribution-Linear Stark Effect

In certain situations the Holtsmark theory has proven to be quite adequate in the description of the influence of ionic fields on spectral lines (Edels and Craggs, 1951; Olsen and Huxford, 1952; Lochte-Holtgreven, 1958). Recent investigations have shown that a reliance on the Holtsmark theory is possible for low charged particle densities, of the order of  $10^{16} \text{ cm}^{-3}$  or less; however for higher densities electron effects should be included into a more comprehensive theory. Combined ion and electron effects at high densities on the Stark broadening of hydrogen lines have recently been studied by Greim (1954), Kolb (1956), Baranger (1958), Kolb and Griem (1958), Griem, Kolb and Shen (1959). Comparative experiments performed by Henkel (1954), Turner (1956), and Bogen (1957) have shown that the inclusion of electronic contributions to hydrogen line profiles result in a substantially improved fit than just the Holtsmark profile alone and that the added electron broadening is comparable in magnitude to the ionic broadening in the wings of a spectral line. Their Stark broadened hydrogen lines were found to be well represented by an expression of the form

$$J(\nu) = \text{const} \times \int_0^{\infty} W(F) J(\nu, F) dF \quad (2-30)$$

where  $W(F)$  is the Holtsmark distribution function and  $J(\nu, F)$  is the electron contribution to the line broadening. From impact theory the electron broadened profile is given by (Margenau and Lewis, 1959),



$$J(\nu, F) = \text{const}/((\nu - \nu_0 - CF)^2 + \gamma^2) \quad (2-31)$$

where  $\gamma$  is the halfwidth of the electron-broadened profile and  $C$  is the Stark displacement per unit field for a Stark component of a line. A complete line profile is generated by evaluating the folded distribution, eq (2-30) for all Stark components.

Direct evidence for spectral line shifts due to the presence of a high electron density is not apparent in their experiments since the linear Stark splitting for hydrogen is symmetric about the central wavelength. Line shifts in helium and argon which exhibit an asymmetric quadratic Stark pattern have been experimentally studied by Seay, et al (1961) and Petschek, et al (1955). Seay, et al investigated several helium lines and compared their experimentally-determined line profiles and shifts with computed profiles and shifts, using quantum mechanical electron halfwidth and shift calculations of Klvel (1955). The uncertainties in the necessary matrix elements for argon made theoretical comparisons with the measurements of Petschek, et al somewhat difficult. Nevertheless, it was shown in both cases that the observed line shifts were greater than those predicated from Holtsmark's theory alone and indicated that high electron densities can also contribute to a spectral line shift.

Estimates of line shifts in the time-resolved spectrum due to the simultaneous action of copper ions and electrons present in the jet collision plasma were also made. The calculations consisted of a determination of the combined electron-ion broadened line profile for both Stark split components of the CuI 4531 transition, by application of eqs (2-30) and (2-31). For a given charged particle density\* the shift of the peak

---

\*Equal ion and electron densities were assumed.

position of the line were found. Kolb's expression for the electron broadened halfwidth  $\gamma$  was used (see Appendix G). The variation of CuI 4531 mean line shift  $\delta_s$ , with particle density found in this manner is given in Fig. 27. For comparison, line shifts predicted by Holtsmark's theory (eq (2-29)), are also shown. Thus the measured line shifts given in Table X lead to the revised numerical estimates for the ion and electron density shown in Table XIV. Charged particle densities in the jet collision plasma of the order of  $4 \times 10^{18} \text{ cm}^{-3}$  are indicated and are about 15 percent smaller than the corresponding density estimates found using Holtsmark's theory alone as was illustrated in Fig. 27. Descriptions of the Fortran programs employed in these computations are given in Appendix G.

#### Holtsmark Theory -Quadratic Stark Effect

The nature of the dependence of the CuI 4531 line shift with applied electric field bears further investigation. The displacement of an energy level under the influence of an electric field depends upon the proximity of other nearby perturbing energy levels with opposite parity to that of the emitting level (Condon and Shortley, 1959; Minnhagen, 1964). If these perturbing levels are energetically close to the excited level of concern then the spectral transition originating from this level will exhibit a linear Stark shift with applied field.\* If on the other hand the excited level is far removed from other perturbing levels, then higher order line

---

\*The Stark displacements of lower energy states are in general much smaller than those of the upper states so that the observed shifts are for the most part indicative of the Stark displacement of the upper level of a transition.

shifts are prevalent. For example, hydrogen spectral lines exhibit large linear Stark displacements at low field strengths due to the degeneracy of excited levels in the absence of an electric field. As the field strength is increased this degeneracy is removed, i.e., the initially overlapping levels are further separated. As a result of this increased level separation a quadratic variation of the line shift with electric field becomes important (Kolb, 1956). Alternately, the NaD-lines show only a quadratic Stark effect since the upper levels for these transitions are far removed from other perturbing states (White, 1934).

CuI energy level tabulations (Moore, 1952) indicate that the nearest perturbing states of opposite parity to the  $6s^2S$  upper level for the CuI 4531 line are the  $6p^2P^o$  states, some  $2000\text{ cm}^{-1}$  removed. Whether this energy separation is sufficient to indicate a clear choice between a linear or higher order Stark effect for the CuI 4531 line is not certain. However, the following considerations strongly suggest that the CuI 4531 line exhibits a quadratic Stark effect.

Hydrogen term separations for which a linear Stark effect predominates are extremely small, of the order of  $0.05\text{ cm}^{-1}$ . The  $7d^3D$  levels of helium interacting with nearby levels at a separation of about  $150\text{ cm}^{-1}$  produce a first order Stark effect in fields of about  $100\text{ kv/cm}$ . Somewhat closer to the copper level spacing under consideration are the interacting  $5s^2S$ ,  $5p^2P^o$ , and  $5d^2D$  states associated with the principal series of potassium. Typical energy separations are of the order of  $4000\text{-}5000\text{ cm}^{-1}$ . These levels show quadratic Stark displacements in fields of the order of  $100\text{ kv/cm}$ . At the upper extreme perturbing level spacings about the  $3p^2P^o$  states for the NaD-lines which show a quadratic Stark

effect are in excess of  $10,000 \text{ cm}^{-1}$ .

Thus, these comparisons indicate that the CuI 4531 line exhibits a quadratic Stark shift with electric field. Although both Holtsmark and Trumpy (1925), and Margenau and Watson (1936) have considered Takamine's Stark effect measurements to imply a linear variation with applied electric field, Fujioka and Nakamura's measurements for several spectral lines of silver show a mixture of linear and non-linear Stark component displacements under experimental conditions similar to those for which the copper line shifts were measured.

Previous ion density estimates must be revised to reflect the quadratic nature of the CuI 4531 Stark splitting and shift. In analogy to eq (2-29) the mean line shift is now given by

$$\delta_s = \frac{1}{2} (K_p + K_n) (F_0 \beta_{\max})^2 \quad (2-32)$$

where  $K_p$ ,  $K_n$  are the line shifts per unit electric field squared for the p- and n- Stark components respectively. Copper ion densities in the jet collision plasma were computed from the measured line shifts of the CuI 4531 line given in Table X and from the relation between the average intermolecular field strength and the ion density by means of eqs (2-32) and (2-23) respectively. The results given in Table XIV indicate that ion densities of the order of  $4 \times 10^{17} \text{ cm}^{-3}$  are present in the jet collision plasma. These estimates are lower by a factor of ten from previous results. The variation of the CuI 4531 mean line shift  $\delta_s$ , with ion density found in this manner is also given in Fig. 27. Estimates of the electron contribution to the observed line shift, obtained from an evaluation of the folded distribution for a quadratic Stark effect, were not made since the electronic contributions were previously found to be small.

## 2.5 Error and Uncertainty Estimates

A number of systematic errors in the measurements and data reduction procedures are inherent in the above results. The extent to which these errors influence the overall accuracy of these results is discussed here. No attempt has been made to ascertain limits of error in each detailed measurement and calculation; instead uncertainty estimates arrived at by studying typical situations were considered to be applicable to all other similar measurements.

### (a) Film Sensitivity

The halfwidth of a spectral line as determined from a line profile will depend upon the value of the slope of the photometric emulsion calibration  $\gamma$  used to obtain the line shape. A variation in  $\gamma$  will in general alter this profile and hence the observed halfwidth of the spectral line. Photometric calibration studies summarized in Table V indicate that the uncertainty in  $\gamma$  is of the order of 0.1 density unit about a mean value of unity. To ascertain the sensitivity of a measured line halfwidth to this  $\gamma$ -uncertainty three profiles of the CuI 5153 line at 8.7  $\mu$ sec were constructed using values for  $\gamma$  of 0.9, 1.0, and 1.1. The total observed halfwidth of this line is about 14A. The maximum deviation in the total halfwidth were found to be of the order of 0.3A or about 2 percent of the total halfwidth. This estimate is considered to be representative of the error in all halfwidth measurements since the line profiles studied extended over comparable ranges in film density. Thus, the uncertainty in a total halfwidth determination is of the order of  $\pm 2$  percent over the total range of observed line halfwidths.

### (b) Wavelength Calibration Effect on Line Width

Errors in the wavelength scale calibration of a densitometer trace will also distort the observed profile and affect the accuracy of the halfwidth measurement. The transformation from a horizontal position measurement to wavelength on each densitometer record was attained with a dispersion curve of the form

$$\nu = a + bx + cx^2 \quad (2-33)$$

where  $\nu$  is the wavenumber of reciprocal wavelength corresponding to the position  $x$ . The coefficients  $a, b, c$  were determined from a least square fit of eq (2-33) using the measured positions of known spectral lines on each densitometer trace, (see Appendix C). The error in a given wavenumber measurement can be expressed in terms of the uncertainties in the numerical coefficients and the error in a position measurement, (Beers, 1958). Position errors were negligibly small as evidenced by the resolution of the densitometer record scanning device (Gerber model S-10-C) and the repeatability of successive position measurements. It was found that the quadratic term in eq (2-33) was comparatively small and could also be neglected in estimating errors. From the approximate relation

$$\nu \approx a + bx \quad (2-34)$$

the contribution to the overall accuracy in wavelength due to uncertainties in the coefficient  $a$  were of the order of 1Å. Error contributions due to uncertainties in  $b$  were much smaller, of the order of 0.05 to 0.10Å for the range of observed line widths. This latter estimate is of importance here since wavelength differences from a center wavelength value were used for all data points describing a line profile. Thus the distortions of an observed line profile in the wavelength direction and

the consequent uncertainties in the total line halfwidth are of the order of 0.05 to 0.10Å. This amounts to about 1 percent of a typical line halfwidth.

#### (c) Spectrograph Slit Width

For a given line shape errors in the slit width value at the wavelength of the observed line contribute to the error in a measured resonance halfwidth as determined from a Lorentzian profile fit. Fits to the sample CuI 5153 line were made in which ten percent variations were introduced for both the assigned slit width and resonance halfwidth values. All three profiles appeared to adequately represent the observed line shape. Larger variations resulted in a degradation of the quality of the profile fit. Experience in the determination of a number of single component Lorentzian line profiles have indicated in general that the construction of a given profile with approximately ten percent variations in either the slit width or resonance halfwidths can result in an acceptable profile match. For multicomponent Lorentzian line profiles small changes of the order of ten to fifteen percent in the slit width, resonance halfwidths, and relative intensities of the spectral component were also found to yield acceptable line fits.

#### (d) Densitometer Slit Width

The finite width of the densitometer entrance slit will modify the shape and hence the breadth of a spectral line. This comes about due to an averaging of the film density across the densitometer entrance slit. Estimates of the densitometer slit broadening given in Appendix H indicate that the error in the calculated profile  $I(\nu)$ , depends upon the square of the dimensionless ratio of the densitometer slit width (in wavelength

units) to resonance halfwidth  $A$ . For the slit width used in obtaining the densitometer records and typical resonance halfwidths as given in Table VII the maximum error in the calculated profile is less than one percent.

#### (e) Absolute Oscillator Strength

The accuracy of the neutral atom density estimates is in part given by the above variations in resonance halfwidths. Errors in the oscillator strength values used in the density calculations can also afford significant contributions. Corliss and Bozman (1962) have assessed the accuracy of their oscillator strength determinations and have found that their absolute  $f$ -values can be in error by as much as a factor of two due to uncertainties in their measurements and the associated data reduction. This is by far the largest source of error in the neutral atom number density evaluations.

#### (f) Self-Absorption

In view of the relatively high particle densities found to exist in the jet collision plasma, the effects of self-absorption on the collision luminosity must be considered. The intensity of the spectral line radiation from interior portions of the plasma will, in general, be diminished upon passage through the absorbing exterior regions. This will result in a distortion of the observed line profile and consequently an error in a measured line halfwidth. The overall agreement in the neutral atom number density estimates for the three lines studied offers indirect evidence that absorption effects have not significantly altered the observed line shapes. In particular, the close agreement in particle density values derived from halfwidth measurements of the CuI 4651 and 5153 lines is



encouraging since these lines represent transitions with lower energy levels that are about 2ev apart and have oscillator strengths that differ by a factor of two. Thus, these lines could be expected to exhibit differences due to varying amounts of self-absorption. Nevertheless, it is of importance to further investigate the extent to which self-absorption could modify the observed spectral line radiation. A decrease in intensity of a spectral profile about the line center will lead to an error in a line halfwidth measurement. This will result in an overestimate of the true line halfwidth and consequently of the neutral particle density value derived from this estimate.

In order to study the effects of self-absorption consider an array of plane-parallel absorbing regions which are traversed by radiation with an initially-known profile  $J_0(\nu)$ . Let the number of absorbing particles and temperature of each region differ from that of adjacent regions. After passage through the first absorbing section, the profile of the emerging radiation will be given by (Chandrasekhar, 1939; Aller, 1953)

$$J_1(\nu) = J_0(\nu) e^{-\tau_1(\nu)} \quad (2-35)$$

where  $\tau_1(\nu)$  is the optical depth and  $J_1(\nu)$  the resultant intensity. The optical depth is frequency-dependent, i.e., the spectral line is selectively absorbed. This intensity profile will in turn be further altered upon passage through the second absorbing section as

$$J_2(\nu) = J_1(\nu) e^{-\tau_2(\nu)}$$

In general, for the  $j$ th slab

$$J_j(\nu) = J_{j-1}(\nu) e^{-\tau_j(\nu)} \quad (2-36)$$

and hence for the radiation exiting from the regions of absorption after traversing a distance  $R$  from the entrance face

$$J_R(\nu) = J_0(\nu) e^{-\tau_R(\nu)} \quad (2-37)$$

The optical depth of the  $j$ th region,  $\tau_j(\nu)$ , is known in terms of the atomic absorption coefficient  $\alpha_j(\nu)$  and the number density of absorbing atoms  $N_a$ , as

$$\tau_j(\nu) = - \int_{r_{j-1}}^{r_j} N_a \alpha_j(\nu) dr \quad (2-38)$$

The atomic absorption coefficient is given as (Penner, 1959; Kuiper, 1962; Allen, 1963)

$$\alpha(\nu) = \frac{\pi e^2}{mc} \frac{\gamma}{4\pi^2} \frac{f_{abs}}{(\nu - \nu_0)^2 + (\gamma/4\pi)^2} \quad (2-39)$$

where  $\gamma$  is the collision damping constant or halfwidth due to broadening collisions,  $f_{abs}$  the absorption oscillator strength,\*  $\nu_0$  the center frequency of the line, and  $e, m, c$  have their usual meanings.

Self-absorption effects on spectral line radiation from the interior of the jet collision plasma upon traversal through the outer fringes of the plasma were derived from this one-dimensional representation. Particle density and temperature profiles obtained from the fluid-dynamic model

---

\*The magnitude of the emission and absorption oscillator strengths are related by

$$g_u f_{em} = g_L f_{abs}$$

where  $g_u$ ,  $g_L$  are the statistical weights of the upper and lower states of the transition.

of a jet collision were used in calculating absorption coefficients and optical depths. Previous results (section 2.4) have indicated that the observed radiation originates from a spatially narrow region between the expanding front of the collision sheet and the position of peak density. That is, the observed spectral line profile is fully developed in this narrow region. Thus the radiation incident upon the absorbing layers was assumed to have a resonance-broadened profile whose halfwidth was determined from the measured neutral atom density. The entrance face of the exterior absorbing layers was at the radial position at which the measured atom density was equal to the calculated density.\* This model appeared reasonable since the absorbing layers under consideration corresponded to a region of the calculated profiles where both the particle density and temperatures were rapidly decreasing as one progressed towards the exit face or front of the plasma. Furthermore, the observed profile would be a close reproduction of the incident profile if self-absorption effects are small, as is indicated by the above mentioned agreement in neutral atom density estimates derived from CuI 4651 and 5153 halfwidth measurements.

Numerical calculations for the optical depth and emerging spectral line profile determined by eqs (2-36), (2-38), and (2-39) were performed. Details of the computer program used and typical results are contained in Appendix I. The computed spectral profiles of the CuI 4651 and 5153 transitions for two values of the time after impact are shown in the

---

\*This assumption will tend to overestimate the amount of absorption since one neglects the decrease in the number of absorbing particles due to ionization. The effect is small, however, for the degree of ionization found to exist in the collision plasma.

figures of this appendix. The magnitude of the temperature of the material at the entrance face of the absorbing layers appeared as a parameter in the calculation and is indicated in the figures. Each line profile was normalized to the maximum intensity value appearing as a result of the computation to facilitate comparison with previously displayed line profiles.

For the CuI 4651 line absorption effects are negligible below a temperature of about  $4000^{\circ}\text{A}$ ; the line center has been diminished by at most a few percent. In the temperature range between  $4000$  and  $5000^{\circ}\text{A}$  absorption becomes pronounced as indicated by the increased width of the line and the appearance of a characteristic dip or self-reversal at the line core. Above  $5000^{\circ}\text{A}$  the spectral line is strongly attenuated and distorted.

Similarly for the CuI 5153 transition, profile distortions due to self-absorption are small for temperatures below  $3000^{\circ}\text{A}$ . Between  $3000$  and  $4000^{\circ}$  absorption effects are noticeable, again as indicated by the increased width of the line and self-reversal at the line center. Above  $4000^{\circ}\text{A}$  the CuI 5153 line is strongly attenuated and distorted.

Estimates of the degree of self-absorption in the observed spectral lines can be obtained by a comparison of the observed line shapes and the computed profiles in the vicinity of the line center, under the assumption that observed distortions from the fitted curves are attributable to absorption effects. A few of the CuI 4651 line shapes in Fig. 19 exhibit a decrease in intensity at the line core, which the most pronounced dip appears with the  $6.7\text{ }\mu\text{sec}$  result (see also Fig. 21). The two side peaks separated by about  $1\text{A}$  for this profile. Keeping in mind that the

spectrograph entrance slit width has essentially smoothed variations in the observed line profiles, but that side peak separations are relatively unchanged by entrance modifications, comparison with appropriate computed absorption profiles suggests that errors in a halfwidth determination may be of the order of 40 to 50 percent in this case. For the CuI 5153 line profiles in Fig. 20 similar absorption effects are seen to occur. In particular the line profile at 7.7  $\mu$ sec shows a dip in the line center and a side peak separation of about 3A. Comparison with self-absorbed profiles again indicates a 40 to 50 percent error in halfwidth. Since radiation source contributions from the nearby exterior plasma layers have not been included in these absorption profile calculations these errors are at best crude and reflect extreme upper limits on the measured halfwidth uncertainty, i.e. line halfwidth errors due to selective absorption of an observed spectral line are significantly less than 50 percent.

(g) Wavelength Calibration Effect on Line Shift

There are several systematic uncertainties that can influence the determination of the ion density in the jet collision plasma. In order for the observed line shifts of the CuI 4531 transition to be meaningful, the magnitude of the shift must be significantly greater than the error in a wavelength position measurement. It has been previously indicated that uncertainties in the wavelength differences from a center wavelength value were small for the data points describing an observed line profile. In the vicinity of the CuI 4531 line, wavelength value errors are of the order of 0.05A. Such an error is small compared to the observed line shifts which are about 1A (see Table X).

#### (h) Effect of Fitting Sensitivity on Line Shift

Furthermore, it was found that uncertainties in the measurement of a line shift due to the line profile fitting procedure were also small, approximately 0.1 Å. That is, variations of the shift of the observed Cu I 4531 line of this magnitude could be tolerated in the determination of a best match line profile. Thus, the combined error in a line shift measurement due to the mechanics of the data reduction and profile fitting are about 15 percent. The corresponding uncertainty in an ion density value determined from a measured shift is of the order of 15 to 25 percent in view of the power law relations between line shift and ion density.

#### (i) Precision of Stark Coefficients

Another source of error appears in the values of the Stark coefficients for the spectral line used in the ion density calculations. In the laboratory measurements of these coefficients the wavelength splitting and shifts are very small (c.f. Table IX). In addition the simultaneous electric field measurements introduce another element of uncertainty. Hence the Stark coefficients can be subject to relatively large errors. To ascertain the magnitude of the variations in a measured Stark coefficient a comparison of the available Stark effect data for several copper lines obtained by different investigators was made. The results presented as linear Stark coefficients are given in Table XV. For each of the tabulated spectral lines there is agreement as to the direction of the line shift with applied electric field for both normal and parallel Stark components. However, factor of two variations in the magnitude of the line shift per unit field are seen to exist in several comparisons. It is unfortunate that only one of the investigators (Takamine) has measured

the Stark splitting and shift for the CuI 4531 transition. Thus a direct indication of the reliability of the Stark coefficients for this spectral line is lacking. If one assumes that the variations in the CuI 4531 Stark data used in the ion density determinations are at worst in error by a factor of two, then the resultant ion density values will be in error by approximately a factor of three.

#### (j) Validity of Stark Coefficient Measurements

There is another systematic uncertainty in the ion density calculations that deserve mention but for lack of sufficient data cannot be quantitatively evaluated. At such high ion densities the mean intermolecular electric field, i.e.  $F_0$  in eq (2-23), is very large. Typically for an ion density of  $10^{18} \text{ cm}^{-3}$  this field is about 375 kv/cm. This is much greater than the electric fields of the order of 50 kv/cm used to experimentally study the Stark effect for copper transitions. Thus there is a possibility that further line splitting and shifts may result with the extremely high fields that exist in the jet collision plasma. Takamine has observed the appearance of such additional Stark components at high field strengths for several other copper spectral lines. The net effect of these added Stark components on the mean shift of the observed CuI 4531 line will depend in detail upon the magnitude and wavelength direction in which the presumed line splitting progresses.

#### (k) Validity of Assumption of Negligible Shift of Central Component

In an effort to avoid large errors in the determination of the CuI 4531 line shift due to the limited wavelength resolution of the time-resolved spectrum, shifts relative to the nearby CuI 4540 transition were measured. This implies that the CuI 4540 line exhibits a negligible shift

---

under the physical conditions existing in the jet collision plasma. Consequently the adequacy of a CuI 4531 line shift measurement as a good indicator of the copper ion density in this experiment depends upon the degree of validity of this assumption. There are two factors which indicate that CuI 4540 line shifts are indeed negligible in this experiment. The nearest perturbing states of the  $e^4D$  upper level for the CuI 4540 transition are the  $x^4P^o$ ,  $D^o$ ,  $F^o$  levels in the anomalous term configuration for copper. Typical energy separations are about  $7000\text{ cm}^{-1}$  between these perturbing states and the  $e^4D$  level of concern. Since the Stark shift is inversely proportional to the separation of interacting levels one can therefore expect any shift in the observed CuI 4540 line to be smaller than the corresponding CuI 4531 shift for which the energy separation of the nearest perturbing level is, as pointed out previously,  $2000\text{ cm}^{-1}$ .

Furthermore there is evidence for a negligible line shift contained in the previous analysis of the time-resolved spectral data. The CuI 4651 transition, studied in conjunction with the CuI 4643 line, is a component of the same multiplet as the CuI 4540 line. Hence the magnitude and direction of its wavelength displacement in an electric field should be comparable to that for the CuI 4540 line (Lochte-Holtgreven, 1938). Multicomponent Lorentzian profile fits to the CuI 4651-4643 pair were shown to match the observed line profiles. No line shifts of either component were introduced into the profile match. Since the  $e^2D$  upper level of the CuI 4643 transition is a component of a different multiplet complex the wavelength direction of its Stark splitting and shift pattern could be different from that of either the CuI 4651 or 4540 line. Also this level is about  $7000\text{ cm}^{-1}$  removed from potential interacting states and hence the



magnitude of a Stark shift for this line would be comparable to that of the CuI 4540 shift. Since no relative line shift of the CuI 4643 line was necessary to achieve a good match to the observed CuI 4651 profile, the assumption of a negligible CuI 4540 line shift appears justifiable.

## 2.6 Plasma Temperature Estimates

Estimates of the temperatures that exist in the collision plasma can be obtained from previous results in several independent ways. If the neutral atoms are in thermal equilibrium then the relative populations of excited states are governed by Boltzmann factors. The ratio of the total light intensity of two spectral lines of the neutral atom originating from two upper energy levels in thermal equilibrium with energies  $E_i, E_j$  can be written as

$$I_j/I_i = (\nu_j^3 g_j f_j) / (\nu_i^3 g_i f_i) \exp(E_i - E_j / kT) \quad (2-40)$$

where  $I$  represents the total line intensity,  $\nu$  the center frequency,  $f$  the oscillator strength for the transition,  $g$  the statistical weight of the upper energy level,  $k$  the Boltzmann constant, and  $T$  the absolute temperature, (Lochte-Holtgreven, 1958; Donohue and Majkowski, 1962; Griem, 1964). The total light intensity is given by the integral of the spectral profile over the full extent of the line, i.e.

$$I = \int J(\nu) d\nu \quad (2-41)$$

For a resonance-broadened line whose profile is described by eq (2-7) the total light intensity is determined by the product  $A J(\nu_0)$  where  $A$  is the resonance halfwidth and  $J(\nu_0)$  the peak intensity at the center

frequency  $\nu_0$ . The ratio of total light intensities for two resonance-broadened lines is then given by

$$I_j/I_i = A_j J_j(\nu_j)/A_i J_i(\nu_i) \quad (2-42)$$

where  $\nu_i, \nu_j$  are the center frequencies of the two lines. Thus, if the oscillator strengths for the spectral transitions are known then a temperature  $T$  can be calculated from the intensity ratios of eqs (2-40) and (2-42).

Values of the temperature at 5.7, 6.7, and 7.7  $\mu\text{sec}$  after initial jet impact have been obtained from the measured resonance halfwidths and relative peak intensities of the observed CuI 4651-4643 and CuI 4531-4525 pairs. The resultant estimates given in Table XVI and Fig. 2B indicate that the temperature of the region from which the radiation originates is of the order of  $10^4$  °K and decreases with time.

The degree of ionization in a plasma in thermal equilibrium is governed by the Saha equation. Estimates of the temperature can also be obtained from the Saha equation relating the equilibrium distributions of ions, electrons, and neutral atoms as\*

$$\frac{N_i^2}{N} = \frac{2 U_i(T)}{U(T)} \left\{ \frac{2\pi m k T}{h^2} \right\}^{3/2} \exp(-E_\infty/kT) \quad (2-43)$$

where  $N_i$  is the number density of ions,  $N$  the number density of neutral atoms,  $U_i(T)$  and  $U(T)$  the partition function for the ion and neutral atom,  $E_\infty$  the ionization potential,  $T$  the absolute temperature, and the constants  $m, k$ , and  $h$  have their usual meanings. The ionization

---

\*Equal ion and electron densities are assumed.

potential, is given by the first ionization potential of the free atom reduced by the Coulomb interaction energy of the plasma  $\Delta E_\infty$  where

$$\Delta E_\infty \approx \frac{3e^2}{4\pi\epsilon_0} \left\{ \frac{4\pi}{3} N_i \right\}^{1/3} \approx 7.0 \times 10^{-7} (N_i)^{1/3} \quad (2-44)$$

for  $N_i$  in  $\text{cm}^{-3}$  and  $\Delta E_\infty$  in ev, (Allen, 1963).

Temperature estimates have been obtained from the Saha equation using the measured jet collision plasma ion and neutral atom densities, and are also given in Table XVI and Fig. 28 at several times after initial impact. Temperatures are seen to be of the order of  $6 \times 10^3$  °K and show a moderate decrease with time after impact.

The shape of the background continuum in the time-resolved spectrum can also yield a temperature estimate. For temperatures between 5000 and 7000°K a black body spectrum has a peak intensity that falls within the 4400-5300Å range of the time-resolved spectrum. In particular the wavelength at peak intensity  $\lambda_m$ , is given by Wien's law

$$\lambda_m T = 0.2896 \quad (2-45)$$

for  $\lambda_m$  in cm and  $T$  in °K (Joos, 1951). Ascribing a black body shape to the observed continuum in the time-resolved spectrum the peak intensity occurred at a wavelength in the vicinity of 5000Å at a time of 6.7 μsec after impact. The associated black body temperature is about  $5.8 \times 10^3$  °K and is in close agreement with previous temperature estimates at this time.

Jet collision plasma temperatures have also been obtained from the fluid-dynamic collision model. The variation with time of the temperature at the center of impact and at the spatial region in the expanding sheet from which the observed radiation originates is illustrated in

Fig. 28. Both curves show the expected decrease in temperature with increasing time, but the calculated temperature values are about a factor of seven lower in magnitude than the temperature estimates previously described. As will be shown this discrepancy can be expected since the fluid-dynamic calculations infer heavy particle temperatures, whereas the estimates derived from spectral observations are electron temperatures.

The temperature of a gas determines the distribution of internal energy for all the different constituents present in the gas in accord with a Boltzmann distribution. The internal energy is composed of the kinetic energy of the free electrons, ions, and neutral atoms, and of the excitation energy of the ions and neutral atoms. The partition of the internal energy is determined by collisional and radiative processes in the plasma. If collisions are the predominant mechanism in determining the state of the gas then thermal equilibrium can be expected, (Dewan, 1961).

Ambartsumyan (1958) has calculated the ratio of the rate of ionization by electron impact to the rate of ionization due to photo-absorption. For the electron densities and temperatures found to exist in a jet collision plasma, the electron-induced ionization rate exceeded that due to radiative absorption by about a factor of ten. Due to their relatively low velocities and hence collision frequencies, heavy particle collision-ionization rates are also negligible. Furthermore Griem (1964) has indicated that if the relative populations of the neutral atom ground state and first excited level are governed by a Boltzmann factor containing the electron temperature, then the relative populations of all higher

levels and the degree of ionization are also determined from appropriate thermal equilibrium relations in terms of the electron temperature. The condition that the collisional-excitation rate of the first excited level exceed the radiative-population rate leads to a minimum value of the electron density at a given temperature that is required to assure thermal equilibrium of all the excited states of the atom. The electron densities and temperatures in a jet collision plasma easily fulfill this minimum requirement. Thus the electrons, ions and atoms of the collision plasma are in thermal equilibrium and the above temperature estimates derived from relative line intensity measurements and neutral atom-ion equilibrium relations are to be interpreted as electron temperatures.

Electron-electron collisions will establish a Maxwellian velocity distribution for the electrons while the heavier particle collisions will also yield a velocity distribution for the ions and atoms but at a temperature that may differ from the electron temperature. The electrons will reach an equilibrium distribution more rapidly than the heavier atoms due to their greater velocity and collision frequency. Finally, energy equipartition between all the particles comes about by electron-ion and electron-atom collisions. The time scale in which energy equipartition comes about is much greater than the time scale in which electrons and heavy particles establish their Maxwellian distribution due to the small energy transfer in an electron-heavy particle encounter, a consequence of the large particle to electron mass ratio. Using Griem's estimate of the equilibration time for the electrons to attain their distribution via electron-electron collisions and the electron densities and temperatures found in this work, the estimated

electron equilibrium time is of the order of  $10^{-11}$  sec. To permit collisional excitation of the atoms and ionization to become established one should allow a somewhat longer time, about  $10^{-10}$  sec. Collisions of the ions and neutral atoms with electrons results in an energy equilibrium but at much later times. The equilibrium time for electrons and ions is found from Griem's estimates to be about  $2 \times 10^{-8}$  sec. whereas for atoms it is about  $2 \times 10^{-6}$  sec. Since these time estimates are in the nature of a time constant one would expect electron-ion equilibrium over a time span of  $10^{-7}$  sec, and electron-atom equilibrium in  $10^{-5}$  sec.

Thus, within the time-resolution of these experiments and for the time period after jet impact studied, the electrons and ions have the same kinetic temperature indicated in the above measurements. The neutral atoms on the other hand have not fully achieved the measured electron temperatures in this time period. Collision temperatures calculated from the fluid-dynamic collision model pertain to the neutral atoms in the plasma and were previously seen to be lower than the corresponding electron temperatures and decreasing with time. Both neutral atom and electron temperatures however appear to converge at somewhat later times in the experiment as indicated in Fig. 28.

## Part III Discussion of Results

An experimental study of the collision of two impinging shaped-charge jets has led to some understanding of a high velocity impact. The gross mechanical features of such a collision have been clearly illustrated and estimates of the neutral atom and ion densities in the collision-generated plasma were derived. Relative oscillator strengths for two neutral copper lines have been determined from line halfwidths in the time-resolved spectrum. The results of these experiments are to be compared with conclusions of other investigators.

### 3.1 Pertinent Hypervelocity Impact Theory

For the jet velocities in these experiments the jet material will act dynamically as a fluid upon impact. Goldsmith (1960) has briefly considered the analogous behavior of a cylinder striking a plane rigid target at lower speeds than those involved in the work presented here. As a result of this collision two regions are formed in the cylinder. Adjacent to the rigid wall the material is fluid-like and flows outward along the target interface, thereby simulating the formation of a radially expanding sheet. Upstream this fluid region is separated by a shock wave from the incoming undisturbed material. Goldsmith has indicated that the entire body can be treated as a fluid and the usual hydrodynamic shock relations (Courant and Friedrichs, 1948) used to describe material conditions in the vicinity of the shock wave reflected from the rigid wall into the advancing material.

Gilvarry and Hill (1956) have applied the hydrodynamic shock

equations to their model of a high speed projectile collision. They have calculated pressure, density, and temperature behind the reflected shocks created by the collision of two plane-parallel solid regions using an equation of state obtained from the statistical Thomas-Fermi model of the atom. Iron and silicon were chosen for these investigations. This one-dimensional shock model is applicable to a jet collision for a sufficiently short time after impact before rarefaction waves from the cylindrical jet boundaries are experienced at the original impact point. Due to these rarefaction waves the shock wave progressing up the jet stem is no longer planar and a one-dimensional collision model becomes unrealistic. At impact velocities in the range of 10 mm/ $\mu$ sec Gilvarry and Hill estimate the pressure behind the reflected shock wave to be of the order of 10 megabar, temperature somewhat greater than  $10^4$  °K, and the density compression ratio about 1.5. Furthermore the resultant shock temperatures were shown to be in excess of the estimated melting temperatures at such pressures and densities so that at least melting of the impacting material is to be expected. These extreme conditions representative of the earlier moments of a jet collision are soon reduced upon arrival of rarefaction waves and radial expansion of the impact material.

Lukasik, et al (1964) have created a fluid-dynamic model descriptive of a head-on jet collision. The early stage of the collision was represented by the impact of a plane-parallel solid region and a stationary rigid wall in a similar fashion to the work of Gilvarry and Hill. Upon impact a shock wave progresses into the solid region and the material between this shock front and the rigid wall comes to rest. For comparative purposes several equation of state representations were used in their



calculations of material properties in the shocked region. Tillotson's equations of state were considered to be most applicable for this work since they are based on both shock wave data up to about one megabar and theoretical results of Thomas-Fermi-Dirac theory at pressures in the vicinity of 100 megabars; thus the material properties at the 10 megabar pressures encountered here were probably correctly described. For a copper jet with a velocity of 8 mm/ $\mu$ sec the impacted material was found to have a Hugoniot pressure of about 12 megabar, temperature of  $1.3 \times 10^5$  °K, and a density compression ratio of 1.9. Since the shaped charge jet tip has a small diameter (of the order of 2 mm) these conditions exist only for a short period of time, typically less than 0.5  $\mu$ sec after which the ensuing expansion of the collision products will terminate this early phase of the collision process.

The second phase of the jet impact model is concerned with the expansion characteristics of the collision, where results of the one-dimensional calculations were employed as initial conditions. The expansion of a one-dimensional slab, of a cylinder, and a sphere of radius comparable to the initial jet tip radius were studied. Three important results were derived from these considerations; namely, the colliding jet material will be vaporized upon expansion; the velocity of the edge or front of the expanding region is the same for either geometry, and is about 17 mm/ $\mu$ sec. The density, pressure, and temperature of the collision products is extremely high in the vicinity of the impact point; for the expanding material near the front they fall off sharply as  $(1 - r/\bar{v}t)^n$ , where  $r$  is the radial distance from the collision center,  $t$  is the time after impact, and  $\bar{v}$  the velocity of the front. The exponent  $n$

has the values 4, 6 and 2 for the material density, pressure, and temperature profiles respectively.\*

### 3.2 Discussion of Experimental Results

These latter theoretical conclusions have been verified by the shaped charge jet collision experiments. The rich copper line spectral content of both the time-integrated and time-resolved records show that copper vapor is present in the collision products. The calculated time for the expanding products to reach the vacuum chamber wall was found to be in excellent agreement with the time at which the neutral atom density is a minimum. A subsequent increase in the neutral atom density is attributed to the pile-up of material at the window accompanying the creation of an inward moving compressive shock created by the wall collision. Furthermore, the extremely high pressure, density, and temperature conditions that are predicted to exist are made evident by the intense continuum radiation that appears on the early portion of the time-resolved spectral record, the appearance of an extremely bright region about the point of collision on the framing camera record, and the presence of highly excited neutral and ionized copper atoms with up to 25 ev excitation.

The emission lines of several spectral transitions in the time-resolved spectrum were shown to possess instrumentation and resonance-broadened contours. Integrated Lorentzian line profiles which combine

---

\*This density profile was the one used in the previously discussed spectral line absorption studies.

the effects of both broadening mechanism were seen to match the observed line shapes in the time interval studied. Values of the spectrograph slit width determined at several wavelengths were found to be in good agreement with calculated values obtained from an optical ray tracing through the direct view prism streak camera combination. Estimates of the neutral atom density for several microseconds after initial jet impact were derived from resonance-halfwidth measurements of three observed spectral lines with known oscillator strengths. The computed densities were found to be in close agreement, of the order of  $4 \times 10^{19}$  per  $\text{cm}^3$  over the time span considered. Since these spectral transitions arise from different excited levels and configurations of the neutral copper atom and have different oscillator strength values, this agreement indicates that the assumptions and methods used in the neutral atom density calculations are valid.

Lukasik, et al have further attempted a numerical solution of the radiative transport equation for the jet collision products using results of their hydrodynamic calculations and theoretical optical opacity estimates. They have shown that the observed spectral radiation has its origin in a narrow region near the front of the expanding collision products and have found the particle density in this region to be approximately two to three times larger than the atom densities derived from the spectral line halfwidth measurements. In view of the uncertainty in the opacity estimates the use of a one-dimensional model neglecting material expansion normal to the outward moving sheet, and the fact that the spectral data from which atom densities are obtained are averaged over time and space due to the finite extent of the spectrograph entrance slit,

the agreement in density estimates is considered to be reasonably good.

The magnitude of the copper ion density in the jet collision plasma has been determined from the measured wavelength shift of a neutral copper line for which some Stark effect data is available. Since the nature of the variation of Stark splitting and shifts with electric field strength is not well established, both linear and quadratic Stark effect characteristics were considered and their influence upon the calculated ion densities has been discussed. In addition, a comparison of the results of Holtsmark's theory for ionic perturbers and numerical evaluations of the folded distribution to include the additional effect of electrons was made, assuming a linear Stark effect for the affected spectral line. Use of Holtsmark's results was seen in this case to yield a slightly higher ion density estimate. Evidence exists however which indicates that a quadratic electric field dependence is more realistic. With this assumption ion densities were calculated using Holtsmark's theory. Copper ion densities of the order of  $4 \times 10^{17} \text{ cm}^{-3}$  were found to exist in the impact plasma indicating that the degree of ionization was about one percent over the time span under consideration.

Oscillator strength values for the CuI 4525 and 4643 spectral transitions of neutral copper have been determined from comparative line half-width measurements using as a basis the CuI 4651 transition whose f-number has been previously established. These results are to be compared with the only other known f-number measurements for these spectral lines obtained by Allen and Asaad (1957). Table XVII contains the oscillator strength values for the CuI 4525 and 4643 transitions found by Allen and Asaad and from this work. Comparative f-values for CuI 4651 from Corliss

and Bozman (1962), and from Allen and Asaad are also given. Corliss (1962) has indicated the existence of a large systematic discrepancy in Allen and Asaad's results due to their incorrect use of a constant normalization factor to establish absolute oscillator strengths from relative measurements. Furthermore, after correction for this systematic difference a residual discrepancy between Allen and Asaad's results and Corliss and Bozman's measurements of about a factor of three still remained. In view of these uncertainties\* it is difficult to assess the agreement between comparative oscillator strength determinations given in Table XVII. At best one can say that the results are not grossly out of line.

### 3.3 Further Extensions and Applications

There are a number of areas of physical interest to which the results of shaped charge jet collision experiments can be of value. A high velocity jet impact represents a new technique for the production of a plasma with a high particle density and moderate degree of ionization. The possibility of generating thermonuclear power from impacting materials as suggested by Harrison (1963) is of great interest and can be viewed as a goal of such efforts. The feasibility of such experiments must, however, await the development of still higher speed projectiles.

---

\*Allen and Asaad further estimate their f-numbers to be accurate to within about a factor of two due to their experimental uncertainties.

Some technological progress in this direction has been made by Walsh, et al (1953), and Jameson (1963) in their design of explosive accelerators and by Walsh, et al and Lukasik, et al in the choice of projectile materials.

A most obvious contribution to the field of atomic spectroscopy and allied areas in astrophysics is in the determination of oscillator strengths for spectral lines from excited energy levels of metallic atoms. At present oscillator strength values are determined either from electric arc experiments (Lochte-Holtgreven, 1958) or by numerical computations of questionable reliability (Allen, 1963). Spectroscopic observations of a hypervelocity projectile impact can offer both an independent experimental verification of existing results and also a continuing program of new *f*-number determinations for selected materials. With the advent of higher speed shaped charge devices and the anticipated increase in the collision plasma ion density, measurements of ionic spectral line oscillator strengths by the methods contained in this work appear possible. This is of particular importance since oscillator strength measurements for ionic spectral transitions are difficult to achieve with present day techniques.

Shaped charge jet collision experiments may also serve as a means of obtaining high pressure and density equation of state measurements for materials that can be made to form a jet under explosive loading. The extremely high pressures and densities experienced at the moment of jet impact are much greater than that obtained in present day experiments specifically oriented towards equation of state determinations, (Walsh and Christian, 1955). With the advent of higher velocity projectiles further extensions in the range of these quantities will be attainable.

Unfortunately direct pressure and density measurements are not possible and hence conditions in the vicinity of the impact center can only be inferred from a detailed analysis of spectroscopic observations and application of a fluid-dynamic model of a jet collision. Nevertheless, one can proceed in a manner similar to that used in this work and correlate experimentally derived particle densities with analogous results from the model calculations. These calculations would be performed parametrically for the various equations of state under study in order to determine the best representation. An alternate procedure would be to determine experimentally the time after initial impact when the material front from the jet collision reaches the vacuum chamber wall. The constant velocity of the front derived from the wall collision time can be related to initial conditions that exist during the early stages of the collision by the equations of motion descriptive of the expansion phase. These initial conditions in turn are determined by the usual hydrodynamic shock relations and the material equation of state.

There is one area of current interest for which the experimental and analytical procedures employed in this work can be directly applied. Extensive research efforts in exploding wire phenomena have led to a basic understanding of the important processes attendant upon a wire explosion. A large amount of theoretical development and experimental results pertaining to the electrical characteristics and dynamic properties of the wire are available (Chace and Moore, 1959, 1962). However scant attention has been given to the information that can be obtained from spectroscopic observations. Time-integrated spectral investigations and to a limited extent time-resolved spectral studies have been made,

but the analysis of these records has been restricted to the identification of spectral lines characteristic of the wire material (Anderson, 1920; Smith, 1925; Reithel, et al, 1959). Exploding wire spectra are rich in detail and the results derived from an analysis of the spectral data along the lines of approach used in this work would be an important contribution to the knowledge and understanding of the phenomenon.

Present day plasma physics applications and astrophysical requirements have placed an obvious emphasis on obtaining Stark effect measurements for certain elements such as hydrogen, helium, argon, etc. Determinations of the ion density in a jet collision plasma, however, have made use of experimentally-determined Stark splitting and shifts of a selected spectral line of copper. The lack of available Stark effect data for such uncommon plasma constituents is to be noted. It is hoped that this and future work in hypervelocity impact experiments will provide an incentive to obtain Stark effect measurements for spectral lines of these unusual plasma components.



**BLANK PAGE**

TABLE I

Explosive Shaped Charge Specifications

Designation	RC-338, E.I. DuPont de Nemours	
Material	Explosive	RDX
	Liner	Copper
Dimension		
Explosive	Cylindrical, 2 in. dia, 3-3/8 in. length	
Liner	0.063 in. wall thickness, 45° total included cone angle	
Mass	Explosive	approximately 200 grams
	Liner	approximately 44 grams

TABLE II

## Summary of Jet Velocity Measurements

Firing no.	Average Velocity (mm/ $\mu$ sec)
56	7.98
57	7.98
59	7.86
99	7.68
Mean	$7.9 \pm 0.1$ mm/ $\mu$ sec

TABLE III

Absorption Lines in the Time-Integrated Spectrum  
of a Jet Collision in Air

Observed Wavelength (A)	Assigned Copper Wavelength (A)	Lower Energy Level of the Transition (ev)
4022	4023	3.78
4067	4063	3.82
4276	4275	4.84
4513	4507	5.57
	4509	5.24
4580	4587	5.10
4646	4651	5.07
4682	4675	5.15
	4697	5.24
4703	4697	5.24
	4704	5.10

TABLE IV

Emission Lines in the Time-Resolved Spectrum  
of a Jet Collision in Helium

Observed Cul Line (A)	Upper Level Designation	Upper Energy Level (cm <sup>-1</sup> ) (ev)	
4507.35	$e^4D \ 1/2$	64472.3	7.99
4509.37			
4513.19			
4525.11	$f^2D \ 1 \ 1/2$	63584.6	7.88
4530.79	$6s^2S \ 1/2$		
4539.70	$e^4D \ 1 \ 1/2$		
4586.97	$e^4D \ 2 \ 1/2$	62948.3	7.80
4642.58	$e^2D \ 1 \ 1/2$	62403.3	7.73
4651.12	$e^4D \ 2 \ 1/2$		
4674.72	$e^4D \ 2 \ 1/2$		
4677.34	$e^4D \ 3 \ 1/2$	62403.3	7.73
4697.49			
4701.71			
4704.59	$f^2D \ 2 \ 1/2$	67142.7	8.32
4767.49	$e^2D \ 1 \ 1/2$	62260.1	8.09
4776.22			
4794.00			
4797.04	$f^2D \ 2 \ 1/2$	67142.7	8.32
4842.29			
4866.10			

TABLE IV (continued)

Observed CuI Line (A)	Upper Level Designation	Upper Energy Level	
		(cm <sup>-1</sup> )	(ev)
5016.61	$e^4D \ 1/2$	64472.3	7.99
5034.36	$e^4D \ 1 \ 1/2$	63584.6	7.88
5076.17	$e^2D \ 2 \ 1/2$	64657.8	8.01
5105.54	$4p^2P^o \ 1 \ 1/2$	30783.7	3.82
5111.91			
5115.49			
5144.12			
5153.24	$4d^2D \ 1 \ 1/2$	49935.2	6.20
5158.36			
5212.78			
5218.20	$4d^2D \ 2 \ 1/2$	49942.1	6.19
5220.07			
5292.52	$e^4D \ 3 \ 1/2$	62403.3	7.73

**BLANK PAGE**

TABLE V

Values of Emulsion Calibration Curve Slope  $\gamma$

Zn 4680	Zn 4722	Hg-Cd 4800
0.90	1.45	1.13
1.03	1.10	0.84
1.00		
0.98	1.28	0.99
Zn 4810	He 5016	Hg-Cd 5086
1.42	1.01	1.37
0.99	0.80	0.72
1.11		
1.17	0.90	1.04

Mean Value  $1.0 \pm 0.1$  density units



TABLE VI

Values of the Constant in Eq. (2-8)

Statistical Theory

Marganeu and Watson (1936)       $\pi/3 = 1.05$

Interruption Theory

Weisskopf (1932)      1

Furssow and Wlassow (1936)       $4/3 = 1.33$

Lindholm (1938)       $\pi/2 = 1.57$

TABLE VII

## Resonance-Broadened Line Halfwidths as

Determined from Integrated Lorentzian Profile Fits

Transition	Time ( $\mu$ sec)	(a) Halfwidth from Single Component Fits (A)		(b) Halfwidth from Multicomponent Fits (B)			
		5153	4651	4587	4651	4643	4540 4531 4525
5.7	11.2	6.60	6.40	5.60	4.60	8.20	3.90 7.00
6.7	12.5	3.46	3.80	3.46	3.40	3.70	1.80 2.80
7.7	9.77	3.26	2.00	3.10	2.74	3.60	4.20 6.00
8.7	8.72	3.06	1.40				
9.7	8.28	3.46	4.20				
10.7	11.2	4.64	4.40				
11.7	10.5	6.08	6.20				
12.7	14.9	7.60	6.80				

TABLE VIII

Relative Intensities as Determined  
from Multicomponent Integrated Lorentzian Profile Fits

Transition	4651	4643	4540	4531	4525
Time ( $\mu$ sec)					
5.7	1.00	0.38	1.00	0.44	0.34
6.7	1.00	0.23	1.00	0.56	0.035
7.7	1.00	0.18	1.00	0.39	0.075

TABLE IX

**Stark Splitting and Shift for Selected Neutral Copper Lines\***

Wavelength (A)	p-Component (A)	n-Component (A)	Maximum Field (kv/cm)
4531	+0.04	+0.03	44.0
5153	-0.10	-0.05	25.3
5218	-0.09	-0.07	25.3
5220	--	-0.06	--

\*From Takamine, (1919); p- and n- refer to directions parallel and normal to the applied field.

TABLE X

CuI 4531 Wavelength Shift and Stark Component  
Separation as Determined from Integrated  
Lorentzian Profile Fits

Time ( $\mu$ sec)	Mean Shift $\delta_s$ (A)	Component Separation d (A)
5.7	1.3	0.36
6.7	1.5	0.42
7.7	1.0	0.29

TABLE XI

Oscillator Strengths for Several CuI Lines\*

Wavelength (A)	g f	g	f
4530.78	0.20	2	0.10
4651.12	1.8	8	0.23
5153.24	1.9	4	0.48

\*From Corliss and Bozman (1962).

TABLE XII

Neutral Copper Atom Density in the Jet Collision Plasma

Time ( $\mu$ sec)	Neutral Copper Density ( $\times 10^{19} \text{ cm}^{-3}$ )		
	5153	4651	4531
5.7	3.6	5.2	9.0
6.7	4.1	3.2	4.1
7.7	3.2	2.9	9.7 *
8.7	2.8	2.8	
9.7	2.7	3.2	
10.7	3.6	4.3	
11.7	3.4	5.6	
12.7	4.9	7.0	

\* Not shown in Fig. 26.

TABLE XIII

Oscillator Strengths for CuI 4643 and CuI 4525

Transition	f-number
4643	0.19
	0.22
	0.20
	Weighted Mean $0.20 \pm 0.01^*$
4525	0.31
	0.20
	0.48
	Weighted Mean $0.33 \pm 0.08^*$

\*The relative intensities of the observed spectral lines given in Table VIII were used to weight the individual f-numbers.



TABLE XIV

## Copper Ion Density in the Jet Collision Plasma

Time ( $\mu\text{sec}$ )	Ion Density		
	Linear Stark Effect		Quadratic Stark Effect
	Holtsmark Theory ( $\text{cm}^{-3}$ )	Folded Distribution ( $\text{cm}^{-3}$ )	Holtsmark Theory ( $\text{cm}^{-3}$ )
5.7	$4.9 \cdot 10^{18}$	$4.2 \cdot 10^{18}$	$3.3 \cdot 10^{17}$
6.7	6.2	5.2	3.7
7.7	3.3	2.8	2.7

TABLE XV

## Stark Coefficients of Several Copper Lines\*

	4056.7			4022.67			4015.8			3861.75			3825.05		
	n	p		n	p		n	p		n	p		n	p	
Takamine (1919)	-0.019	-0.020		+0.014	+0.010		--	--		-0.0025	-0.0027		--	--	
Nagaoka and Sugiura (1924)	-0.020	-0.019		+0.010	+0.014		-0.013	-0.014		-0.0027	-0.0025		-0.0023	-0.0035	
Fujioka and Nakamura (1927)	-0.018	-0.018		+0.014	+0.016		-0.024	-0.015		--	--		-0.0036	-0.0023	

\* In units of A/kv/cm .

TABLE XVI

## Jet Collision Plasma Temperatures\*

Time ( $\mu$ sec)	Relative Line Intensity		Saha Equation	Black Body
	CuI4651-4643	CuI4531-4525		
5.7	12,000	14,000	6250	-
6.7	6,000	5,200	6220	5800
7.7	4,000	6,800	6130	-

\*Temperatures in  $^{\circ}$ K

TABLE XVII

## Comparison of Oscillator Strength Values

Cul Transition	This Work	Allen and Asaad	Corliss and Bozman
4651	--	1.7	0.23
4643	0.20	0.64	--
4525	0.33	0.32	--

**BLANK PAGE**

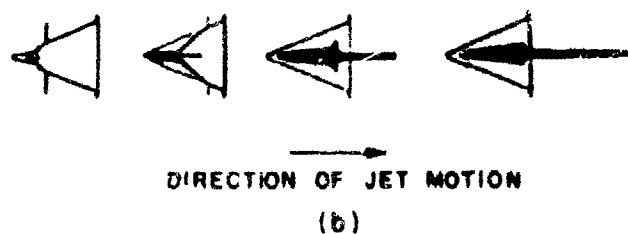
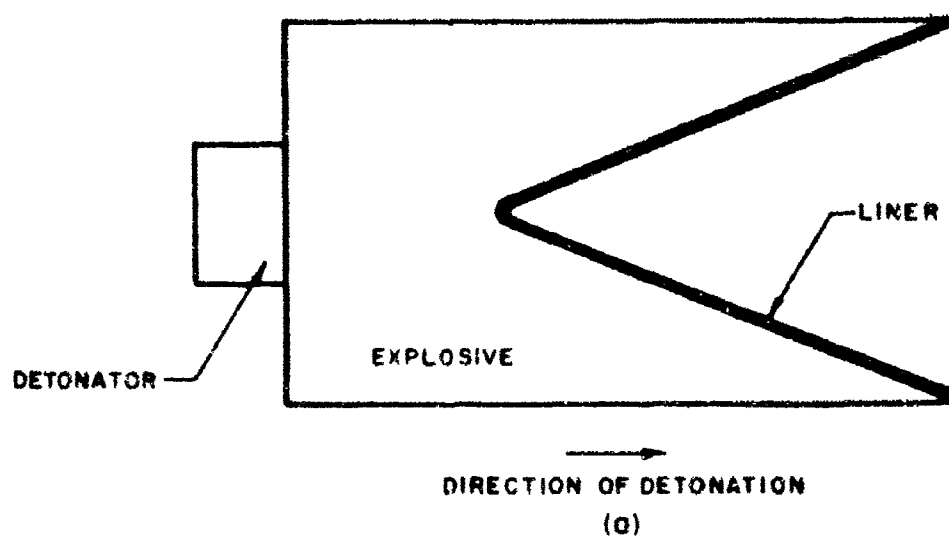


FIG. 1. EXPLOSIVE SHAPED CHARGE JET FORMATION  
 (part (b) from R.J.Eichelberger and E.M. Pugh,  
 J. Appl. Phys. 23, 537 (1952).)

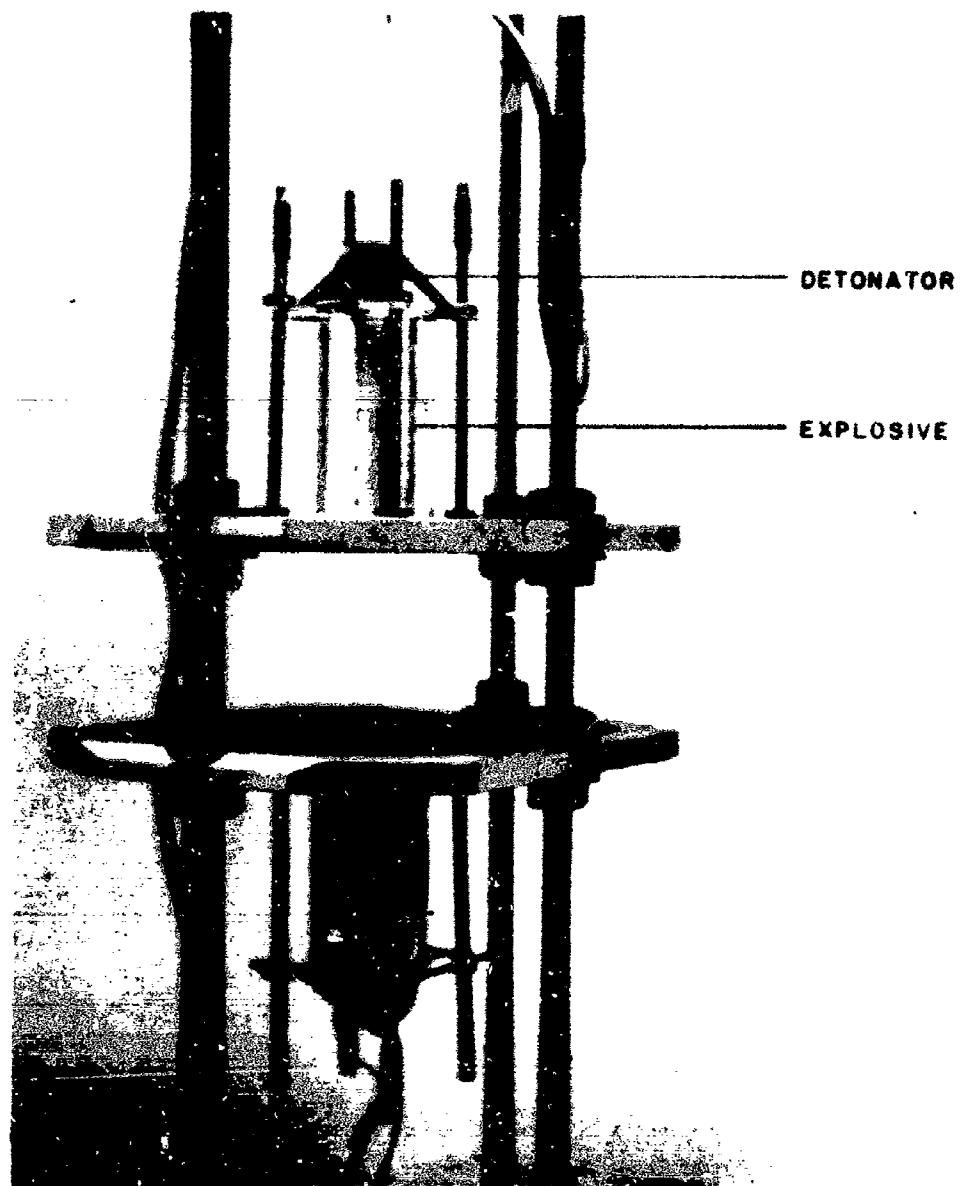


FIG. 2. EXPLOSIVE MOUNTING AND SUPPORT STRUCTURE

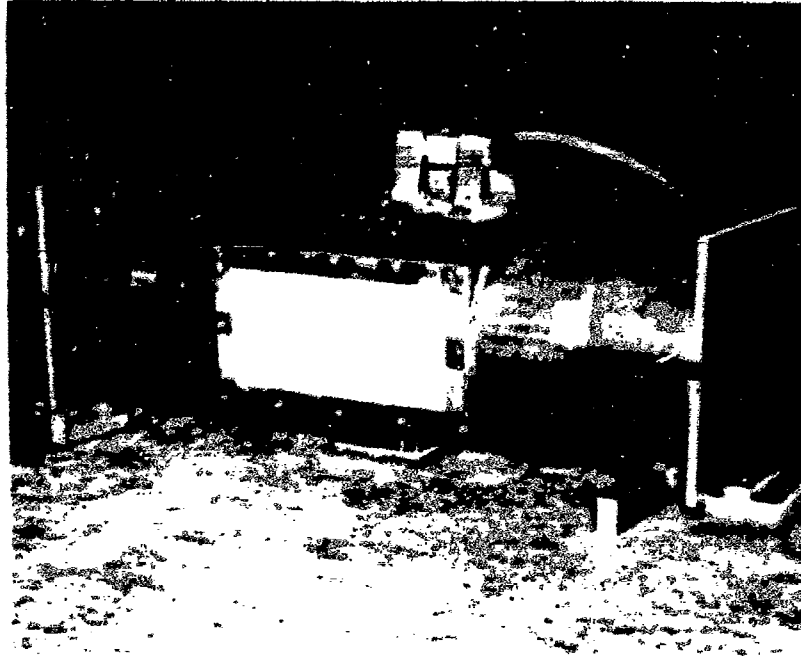


FIG. 3. VACUUM CHAMBER USED IN FIRING NO. 109



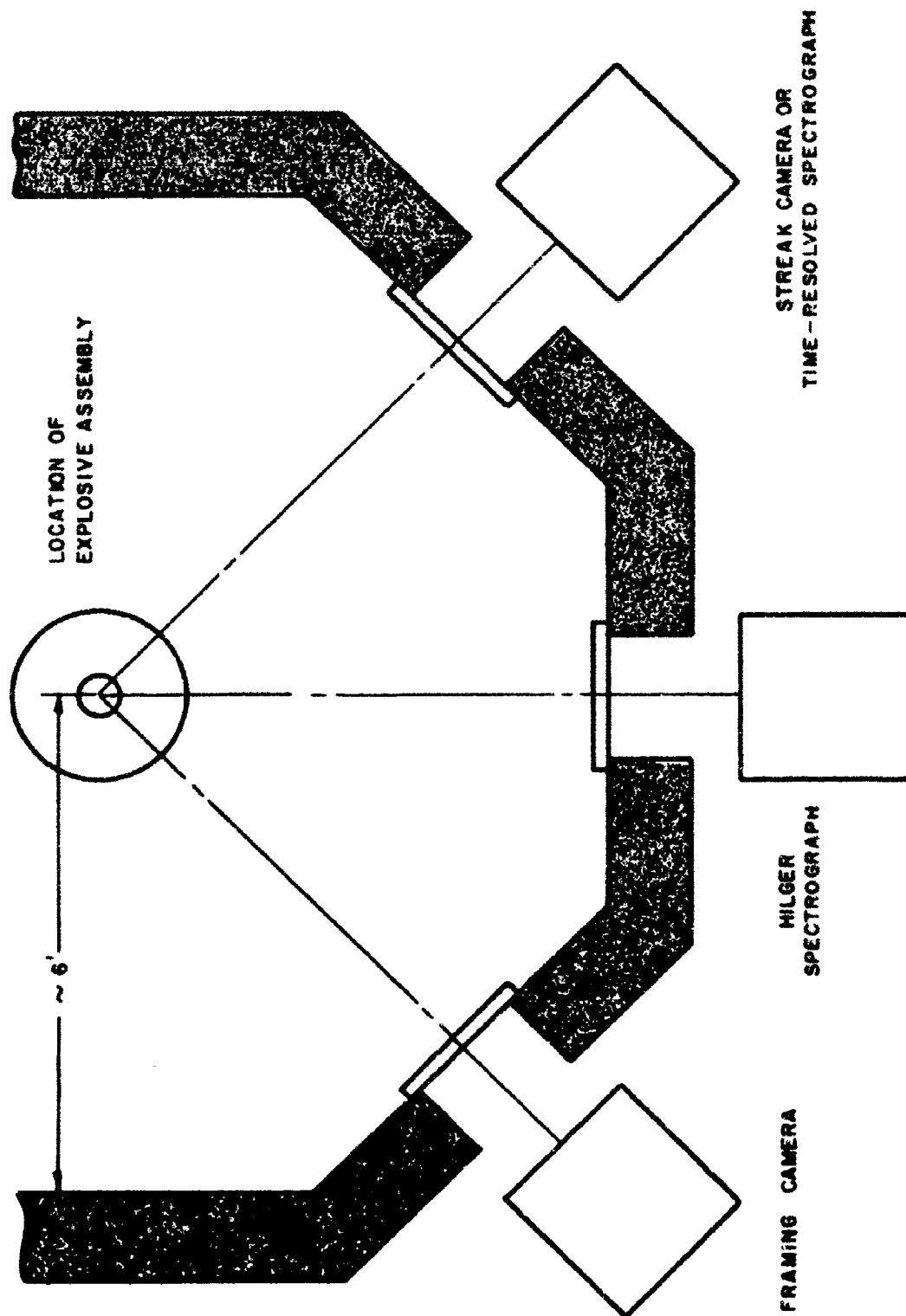


FIG. 4. PLAN - VIEW OF FIRING CHAMBER

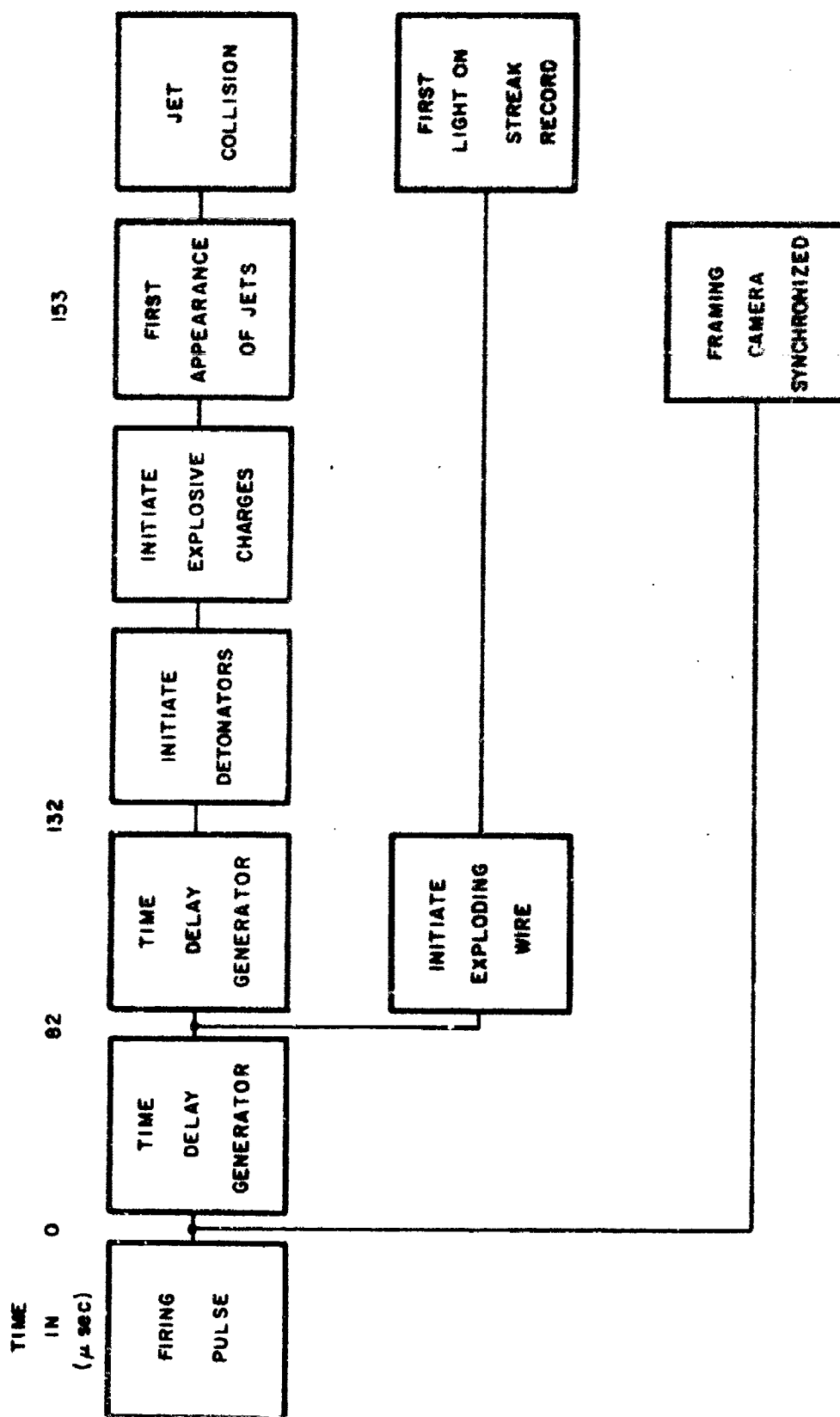


FIG. 5. TYPICAL TIMING SEQUENCE

TIME —→

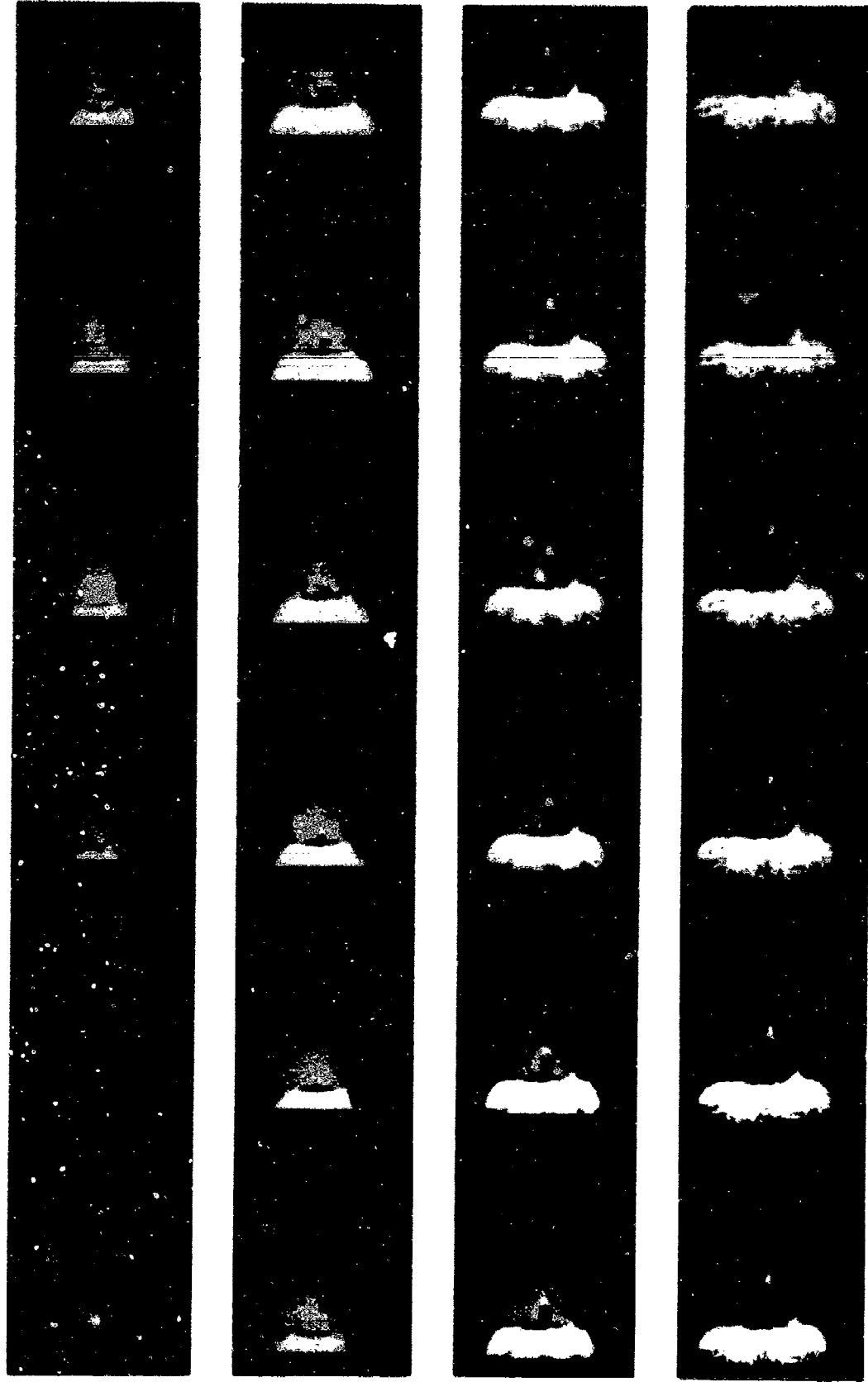


FIG. 6. FRAMING CAMERA RECORD OF JET FORMED BY COPPER-LINED SHAPED CHARGE  
(1.4  $\mu$ SEC PER FRAME)

TIME —————>

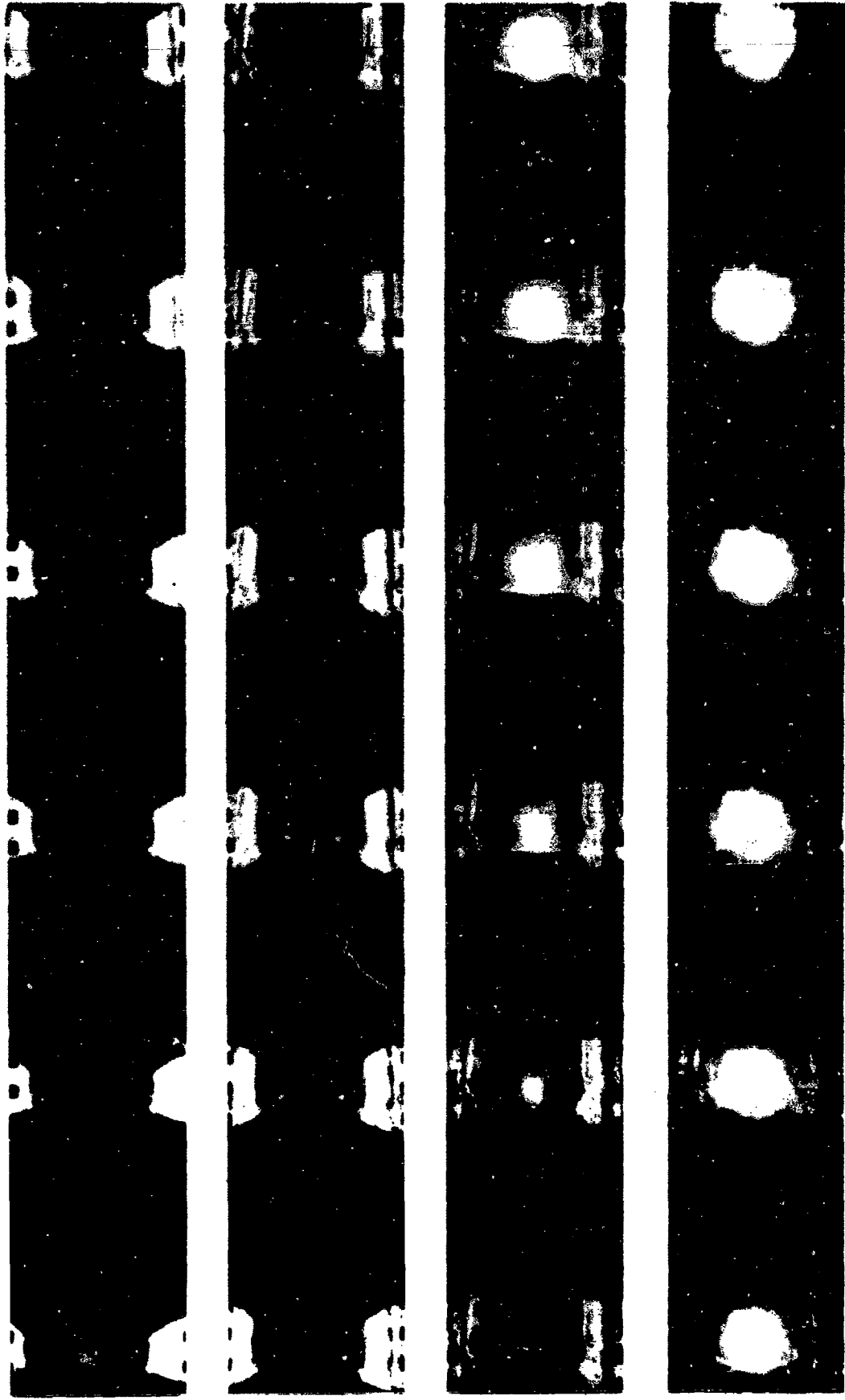


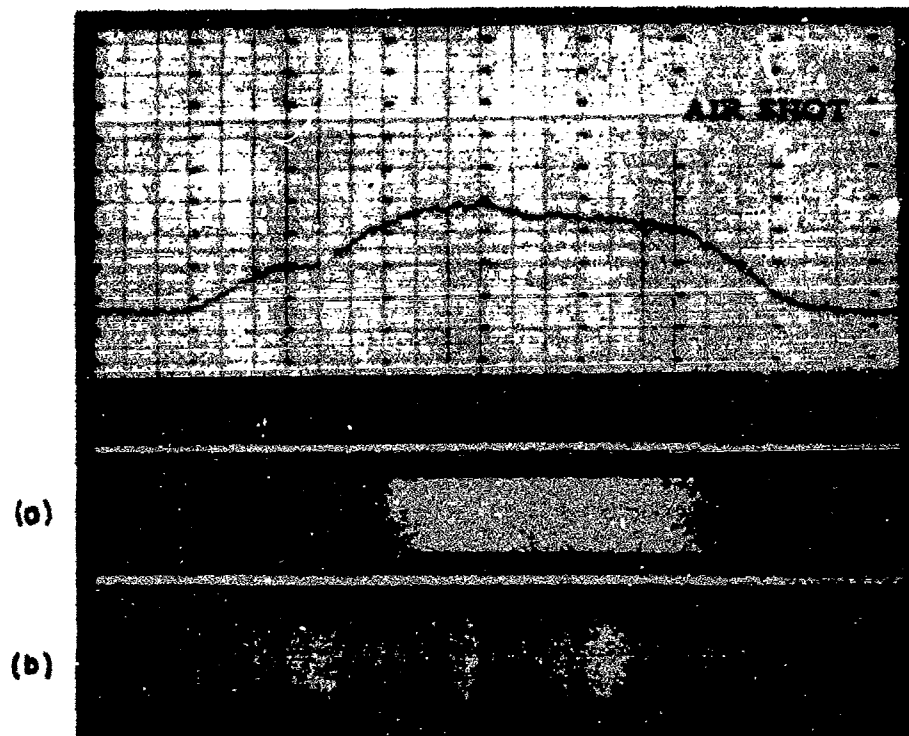
FIG. 7. FRAMING CAMERA RECORD OF JET COLLISION IN AIR  
(1.4  $\mu$ SEC PER FRAME)

— 10 $\mu$  SEC



TIME —→

FIG. 8. STREAK CAMERA OF TWO COPPER JETS BEFORE AND AFTER COLLISION



O = COLLISION SPECTRUM

b = Cu SPARK

FIG. 9. TIME-INTEGRATED SPECTRUM OF JET COLLISION IN AIR

TIME →

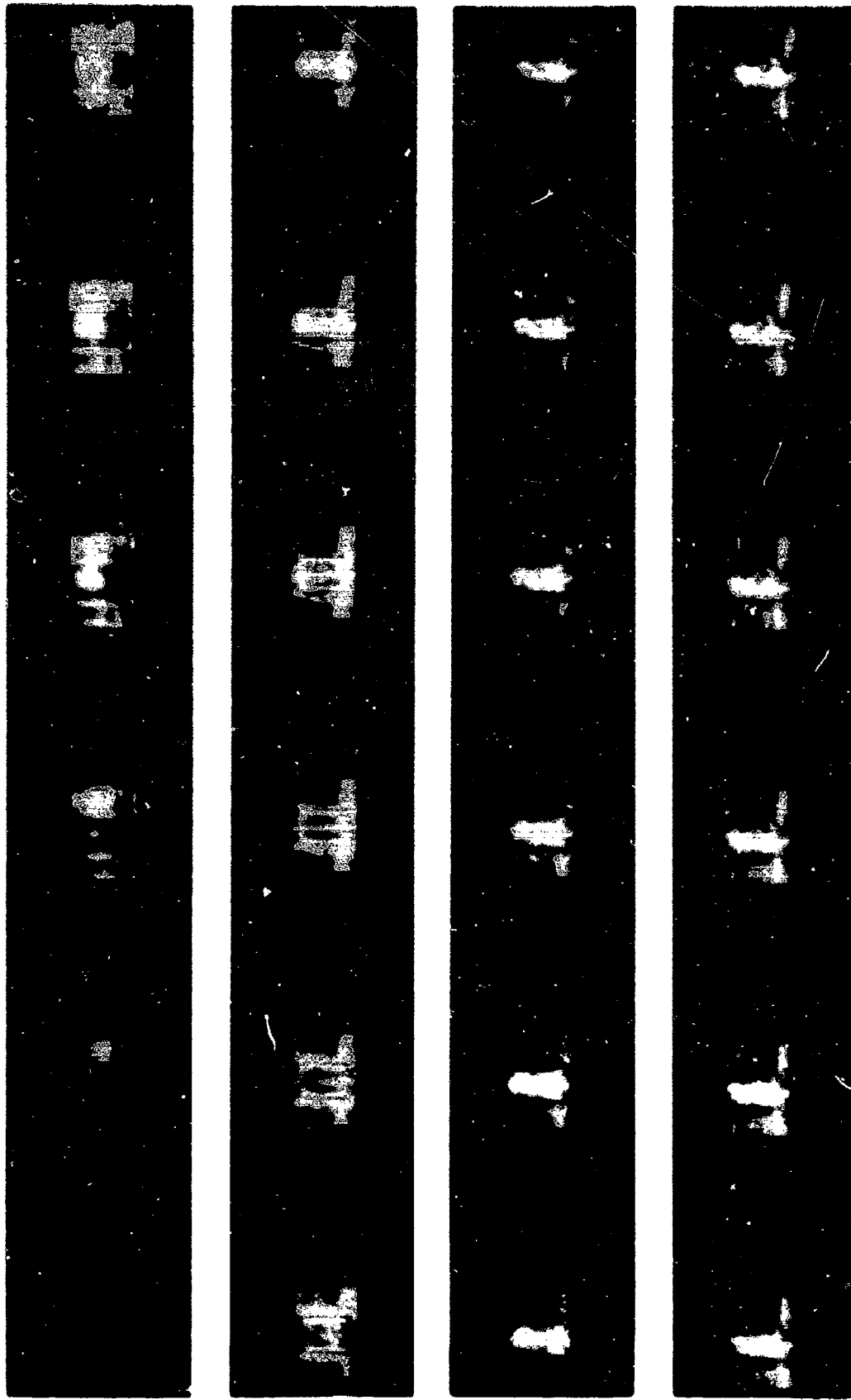


FIG. 10. FRAMING CAMERA RECORD OF JET COLLISION IN FIRING NO. 109  
(1.4  $\mu$ SEC PER FRAME)

TIME →

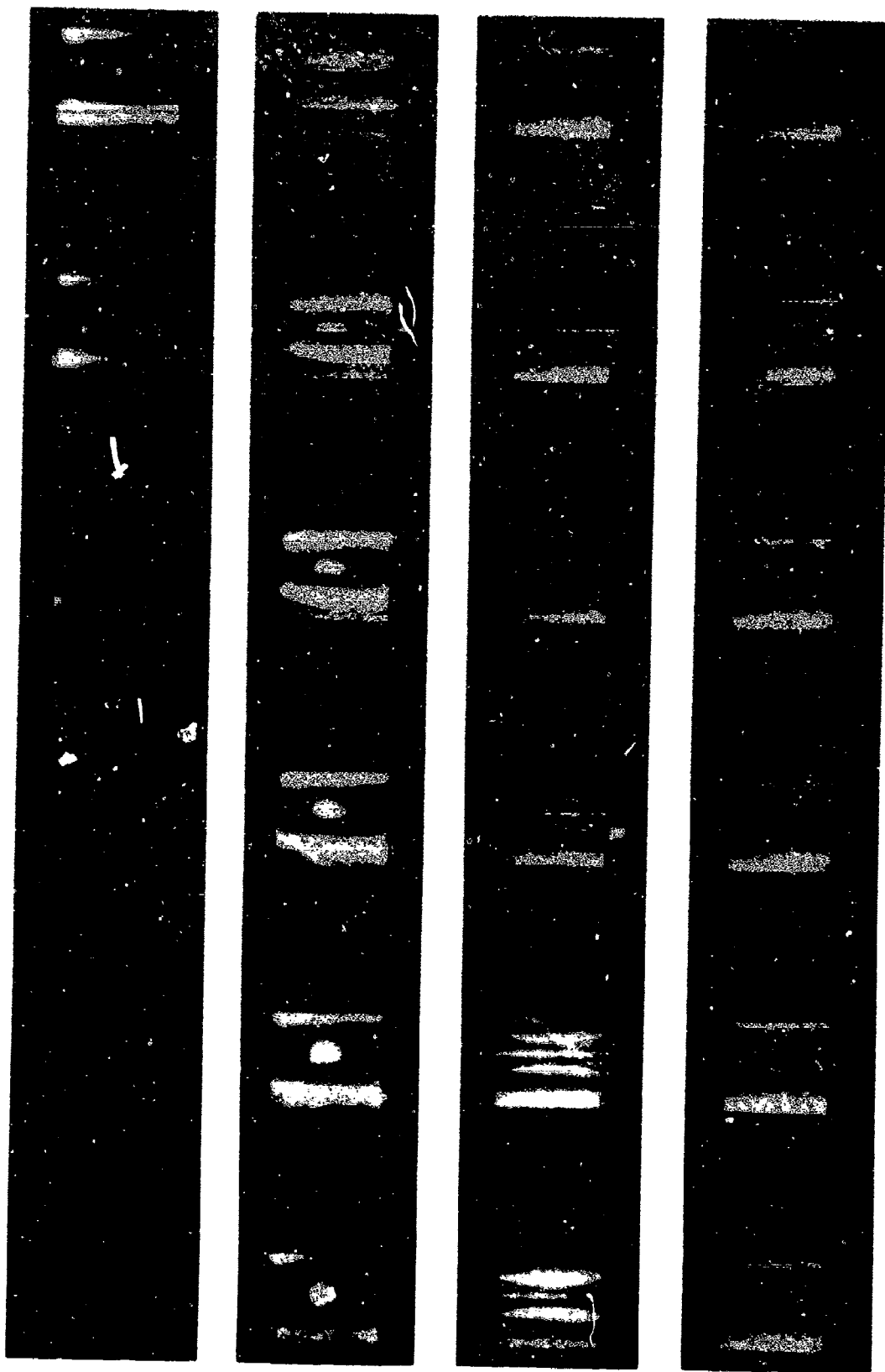
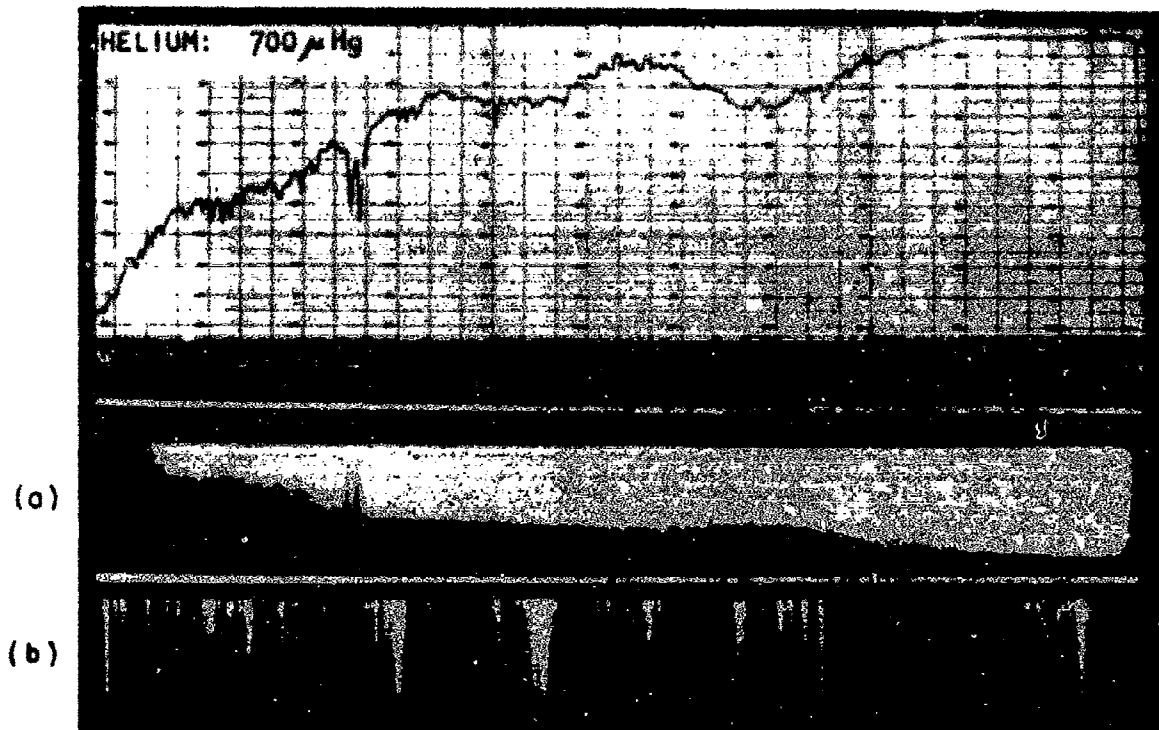


FIG. 11. FRAMING CAMERA RECORD OF JET COLLISION IN FIRING NO. 124  
(1.4  $\mu$ SEC PER FRAME)





FIG. 12. RECOVERED SUPPORT STRUCTURE



a = COLLISION SPECTRUM

b = Cu SPARK

FIG. 13. TIME-INTEGRATED SPECTRUM OF JET COLLISION IN HELIUM

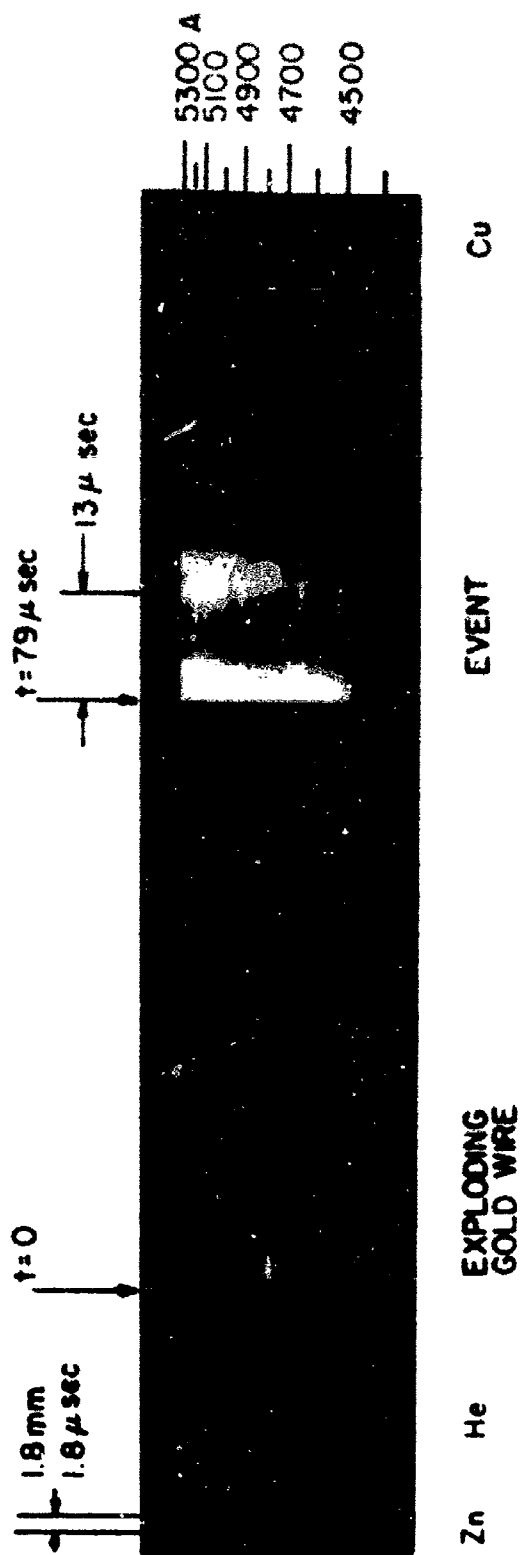


FIG. 14. TIME-RESOLVED SPECTRUM OF JET COLLISION IN HELIUM

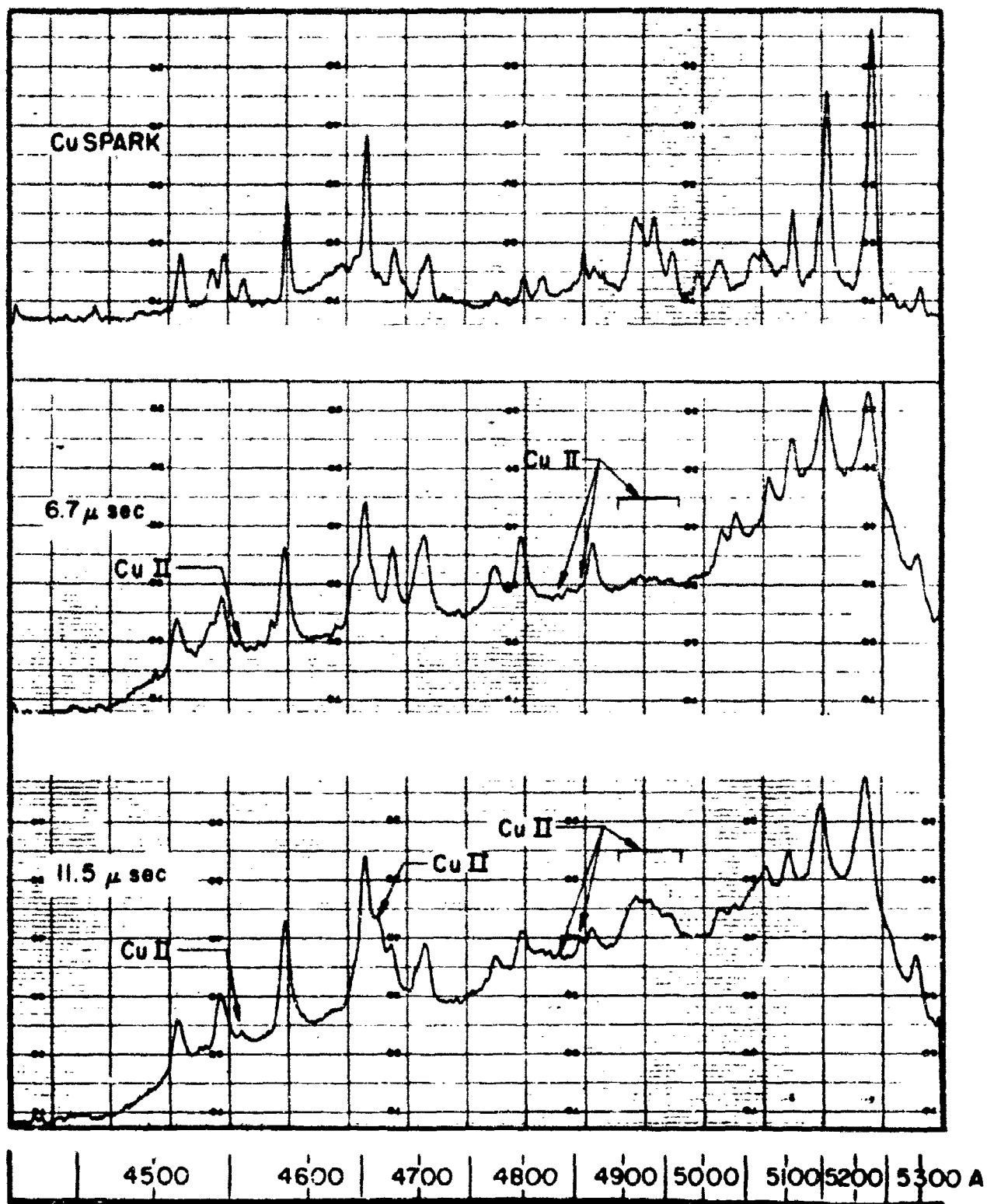


FIG. 15. DENSITOMETER SCANS OF TIME-RESOLVED SPECTRUM

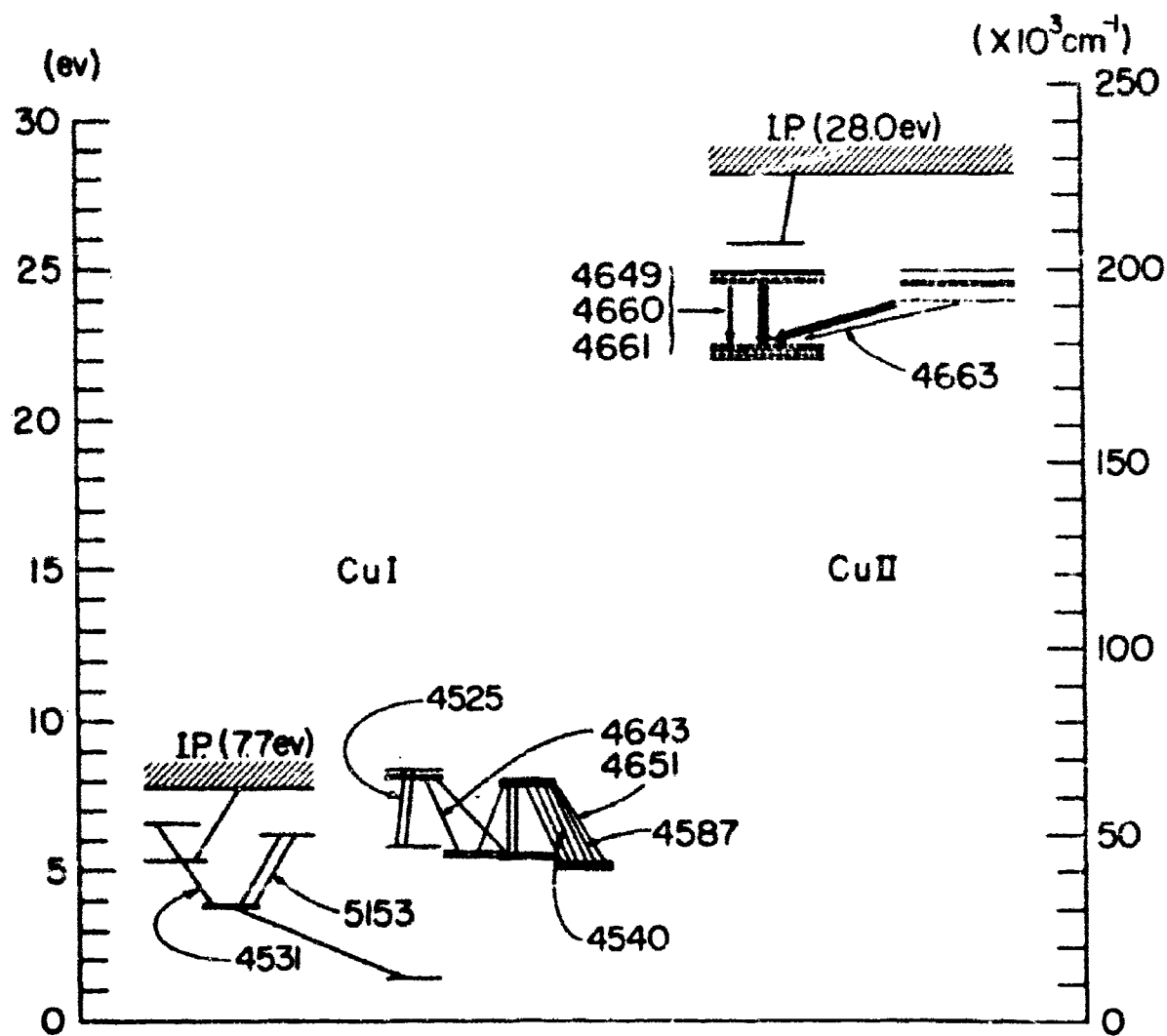


FIG.16. COPPER ENERGY LEVEL DIAGRAM

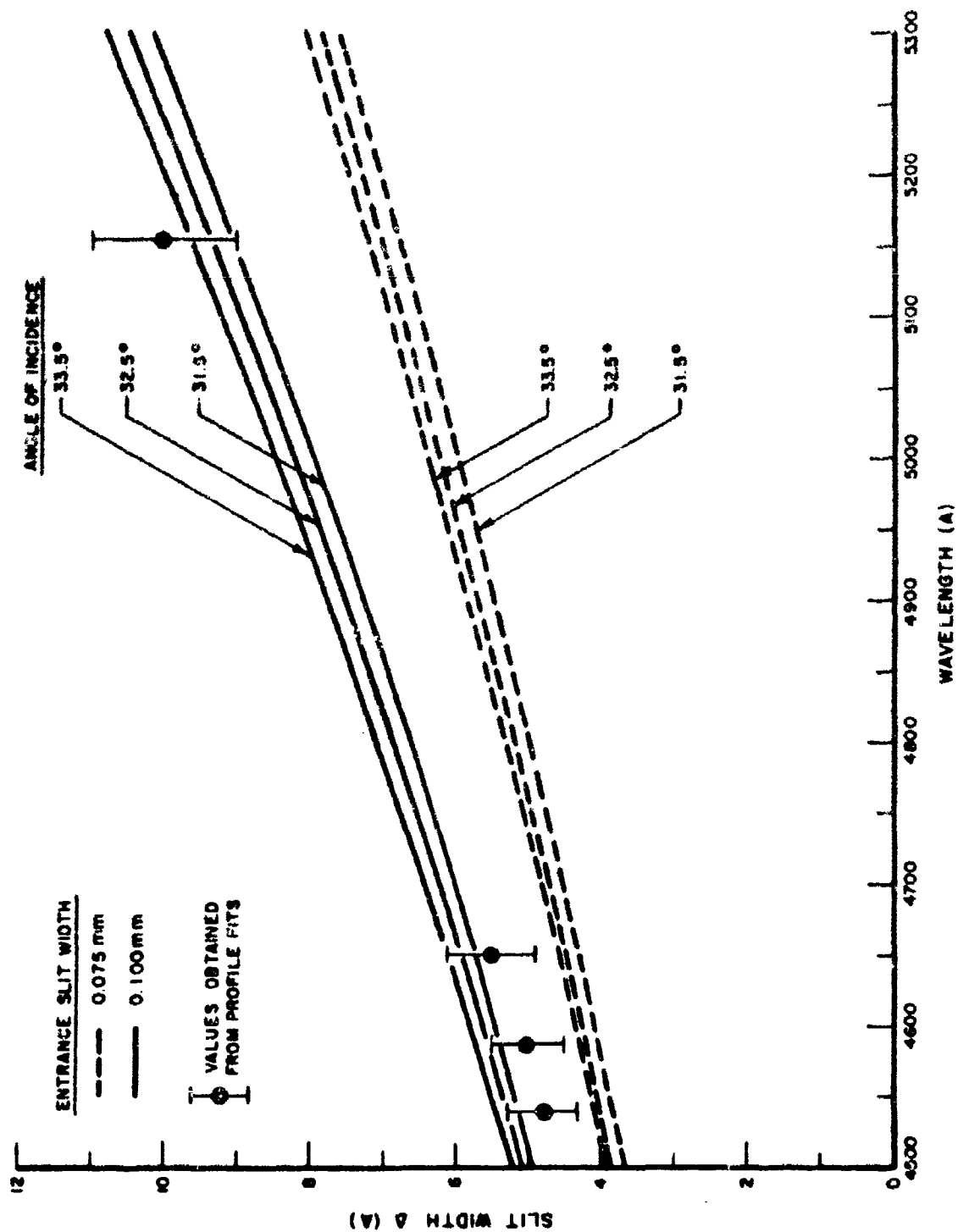


FIG.17. SLIT IMAGE WIDTH VARIATION WITH WAVELENGTH

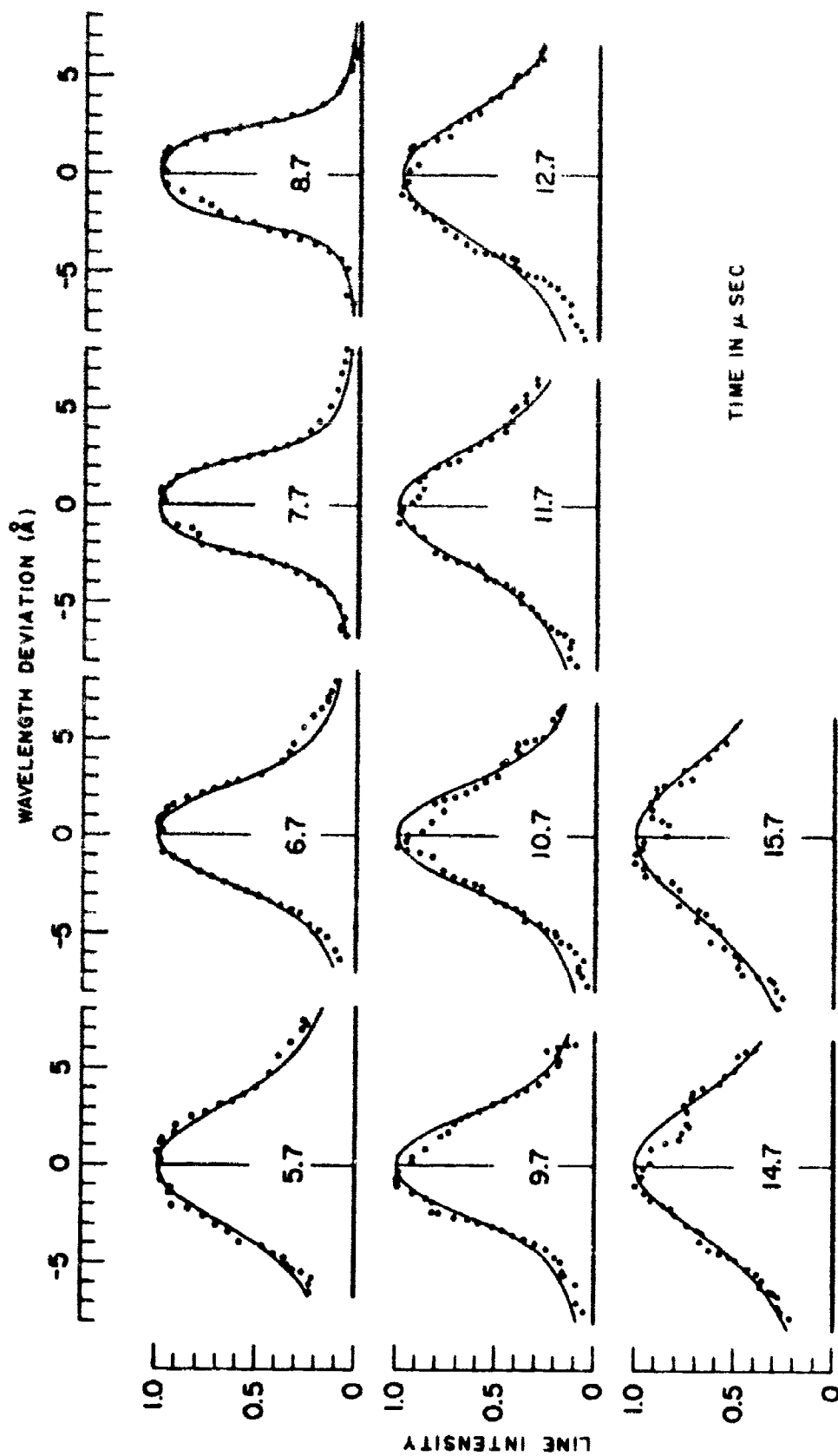


FIG. 18. CuI 4587 INTEGRATED LORENTZIAN FITS

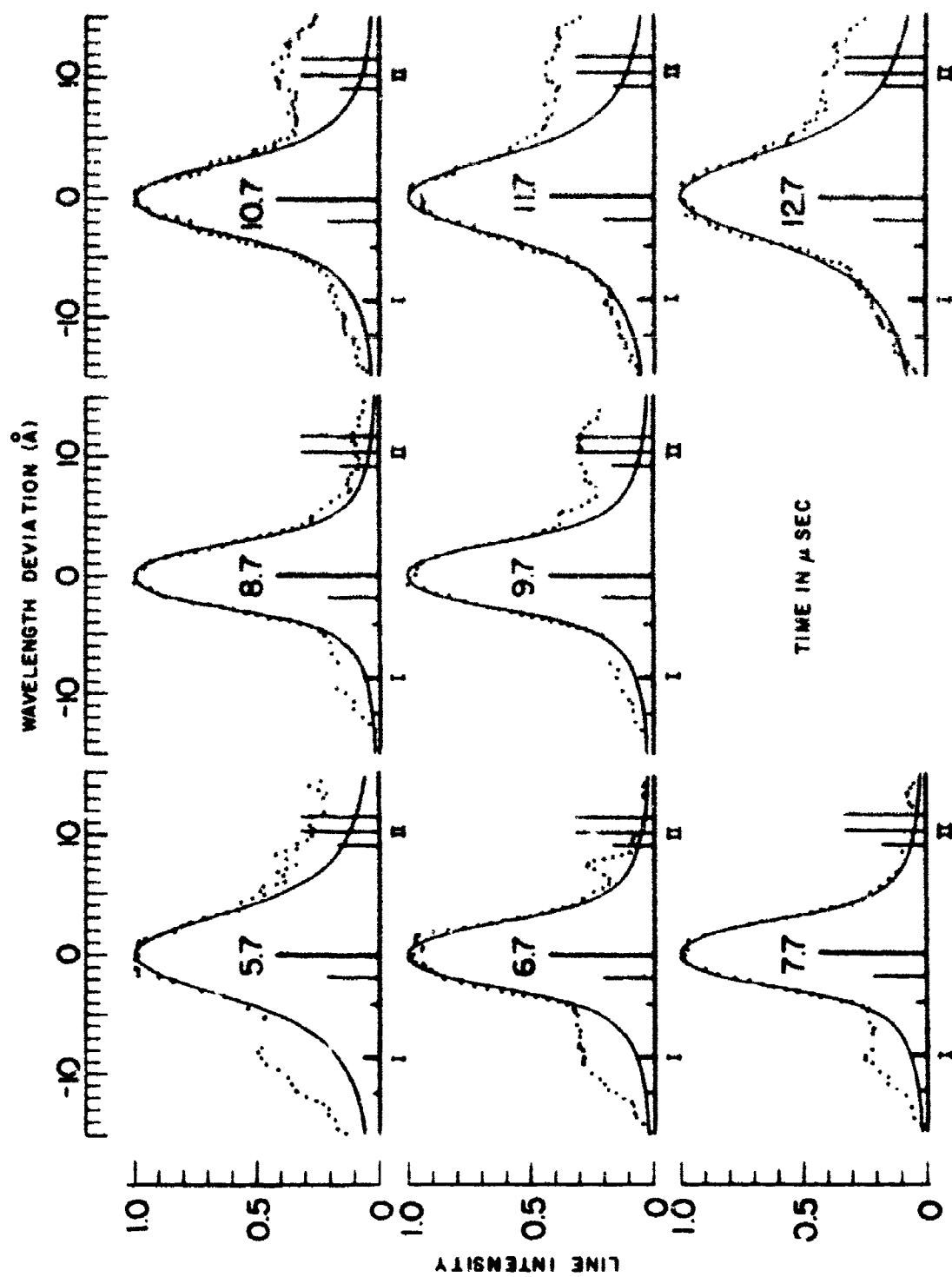


FIG. 19. CuI 4651 INTEGRATED LORENTZIAN FITS



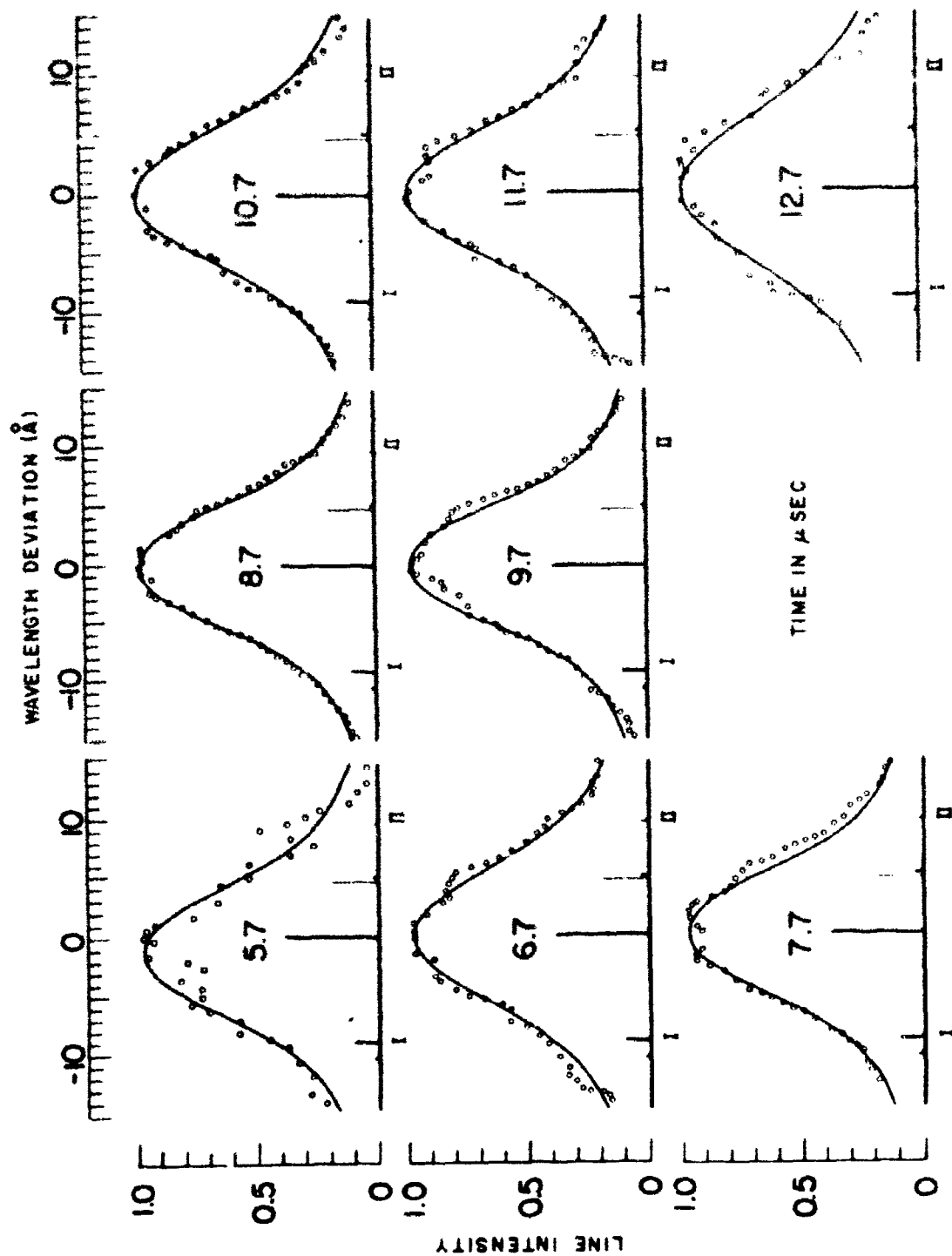


FIG. 20. CuI 5153 INTEGRATED LORENTZIAN FITS

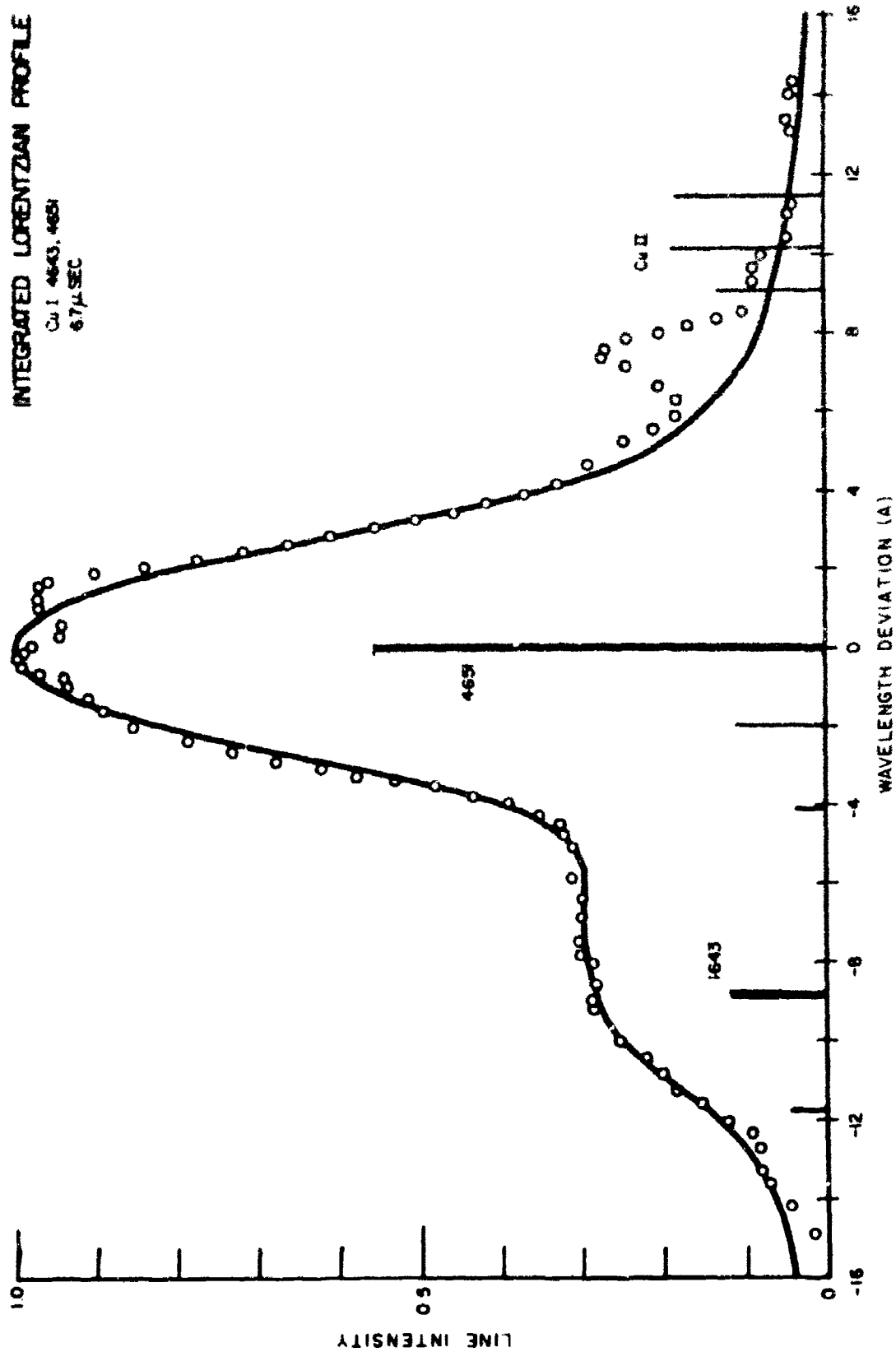


FIG. 21. INTEGRATED LORENTZIAN PROFILE Cu I 4643, 4651 AT 6.7  $\mu$  SEC.

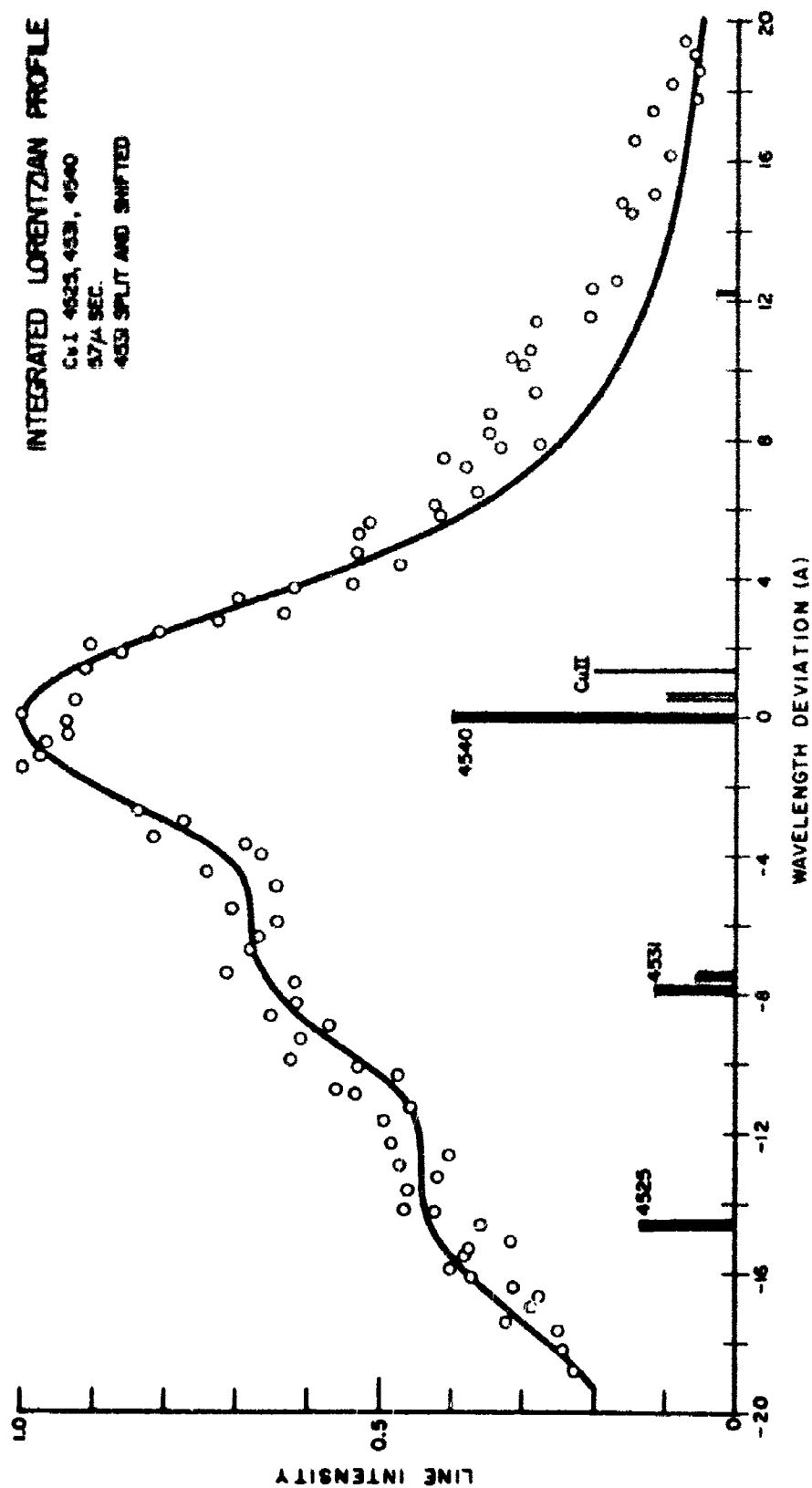


FIG. 22. INTEGRATED LORENTZIAN PROFILE Cu I 4525, 4531, 4540 AT 5.7  $\mu$  SEC. 4531 SPLIT AND SHIFTED

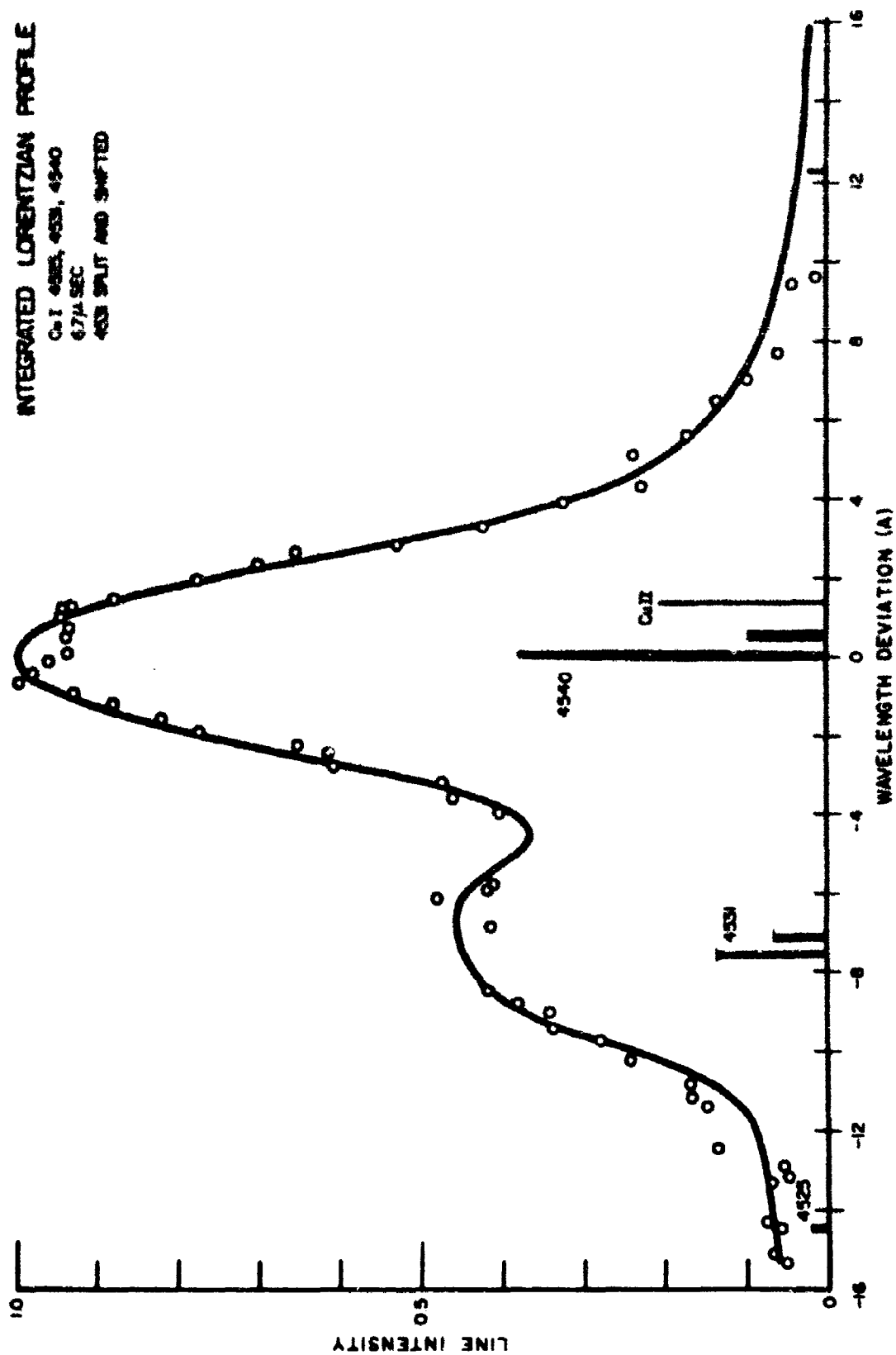


FIG. 23. INTEGRATED LORENTZIAN PROFILE Cu I 4525, 4531, 4540 AT 6.7  $\mu$  SEC. 4531 SPLIT AND SHIFTED

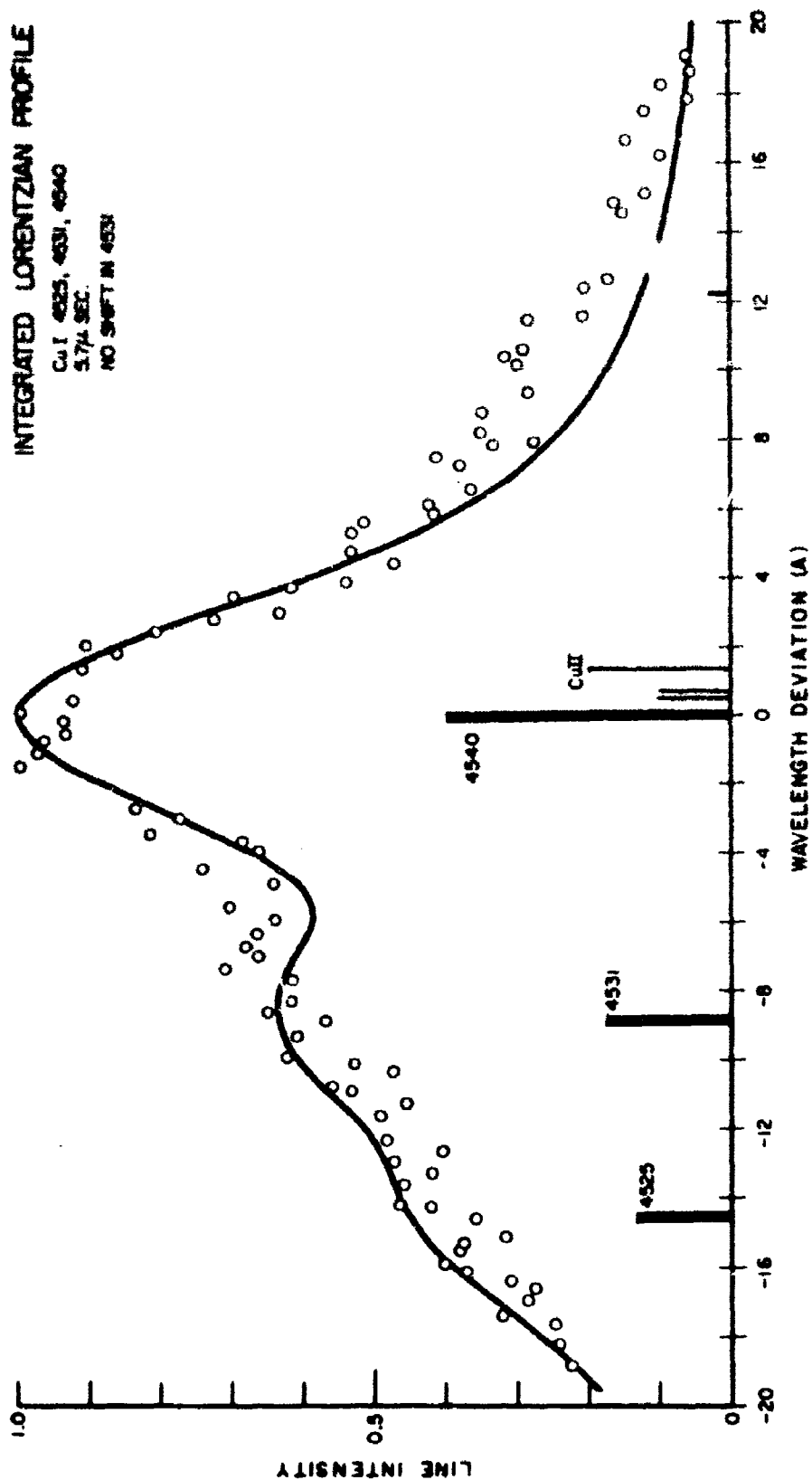


FIG. 24. INTEGRATED LORENTZIAN PROFILE Cu I 4525, 4531, 4540 AT 5.7  $\mu$  SEC. NO SHIFT IN 4531

INTEGRATED LORENTZIAN PROFILE  
 Cu I 4525, 4531, 4540  
 6.7  $\mu$  SEC.  
 NO SHIFT IN 4531

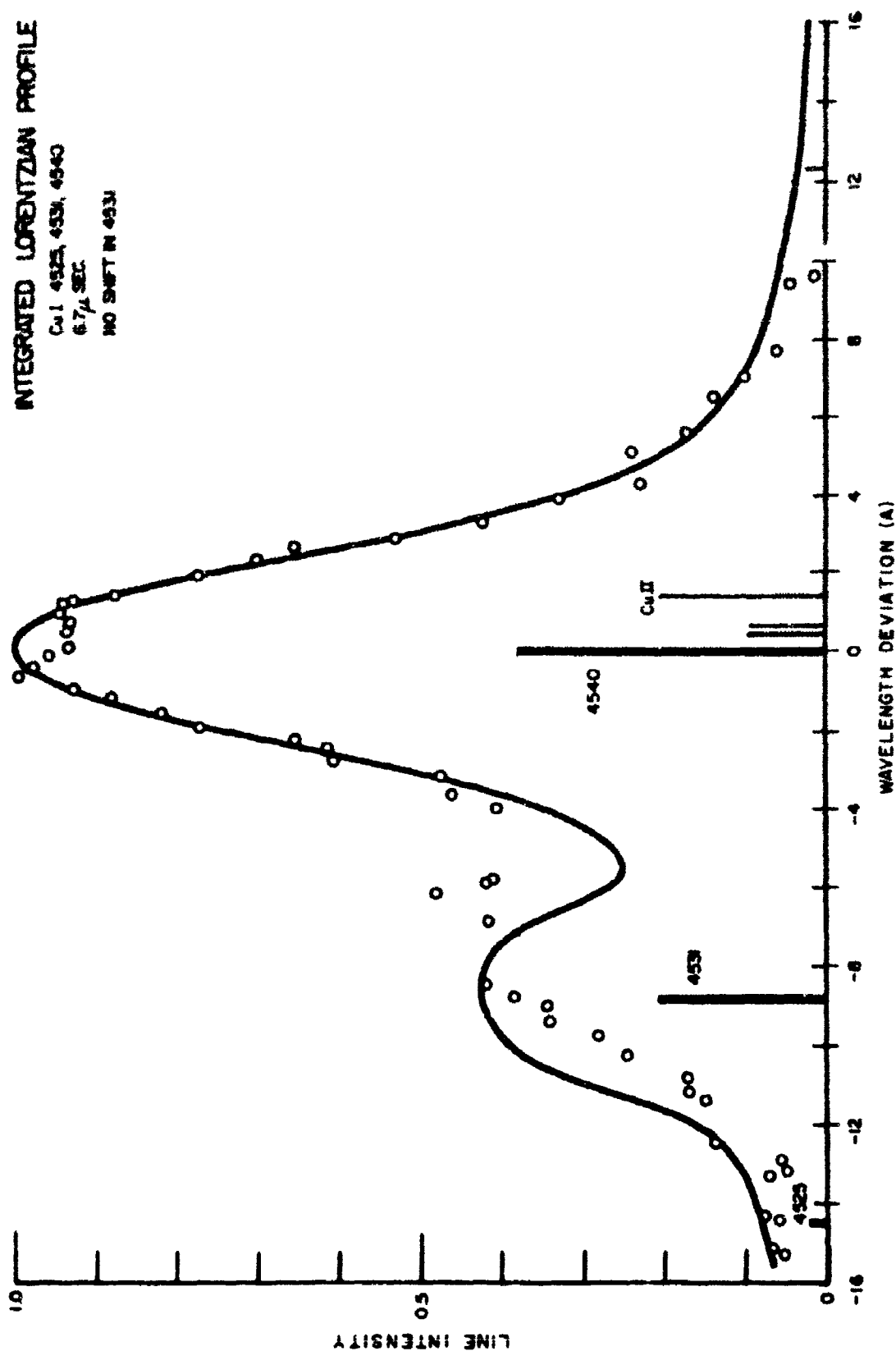


FIG. 25. INTEGRATED LORENTZIAN PROFILE Cu I 4525, 4531, 4540 AT 6.7  $\mu$  SEC. NO SHIFT IN 4531

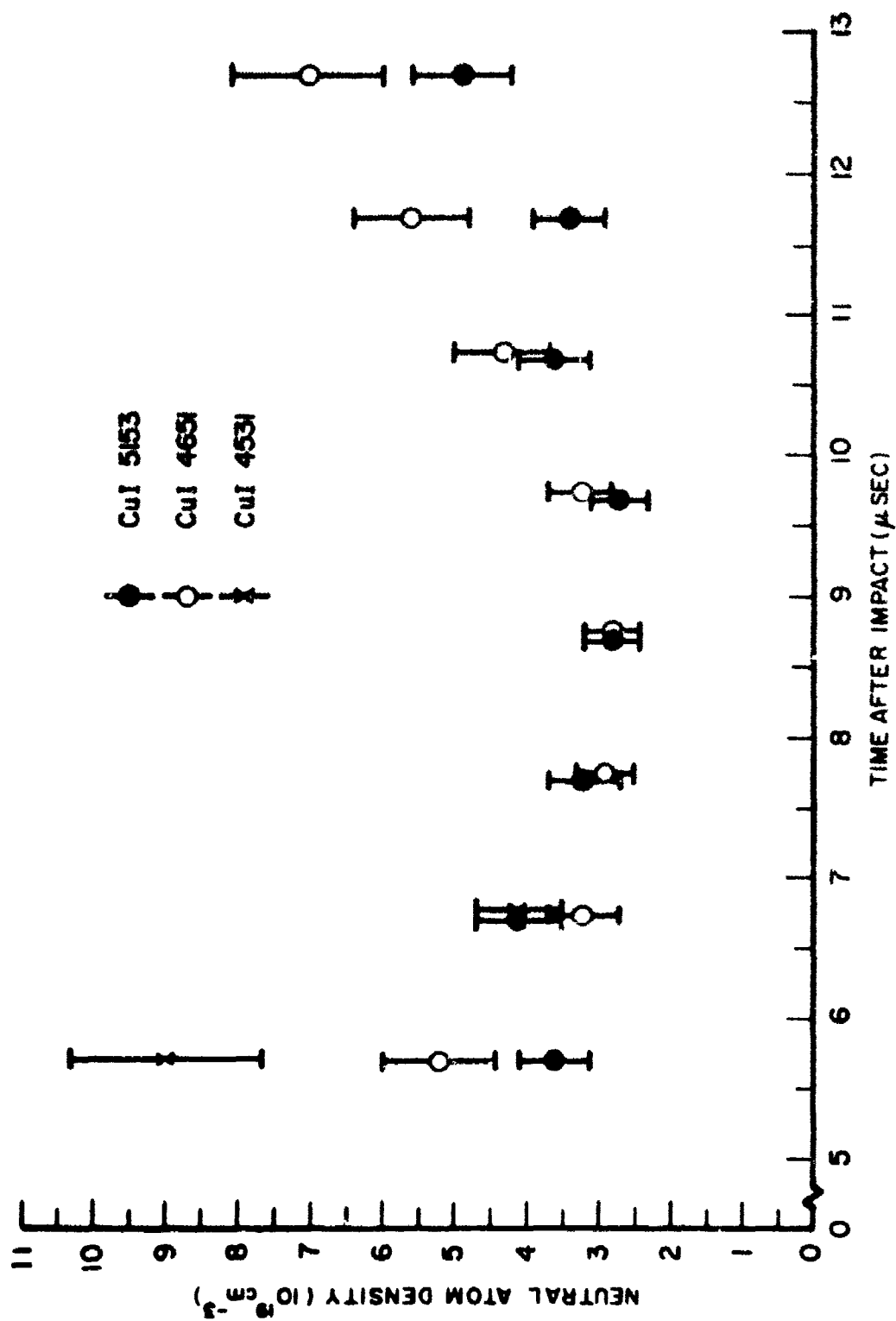


FIG. 26. TIME VARIATION OF NEUTRAL COPPER ATOM DENSITY IN JET COLLISION PLASMA

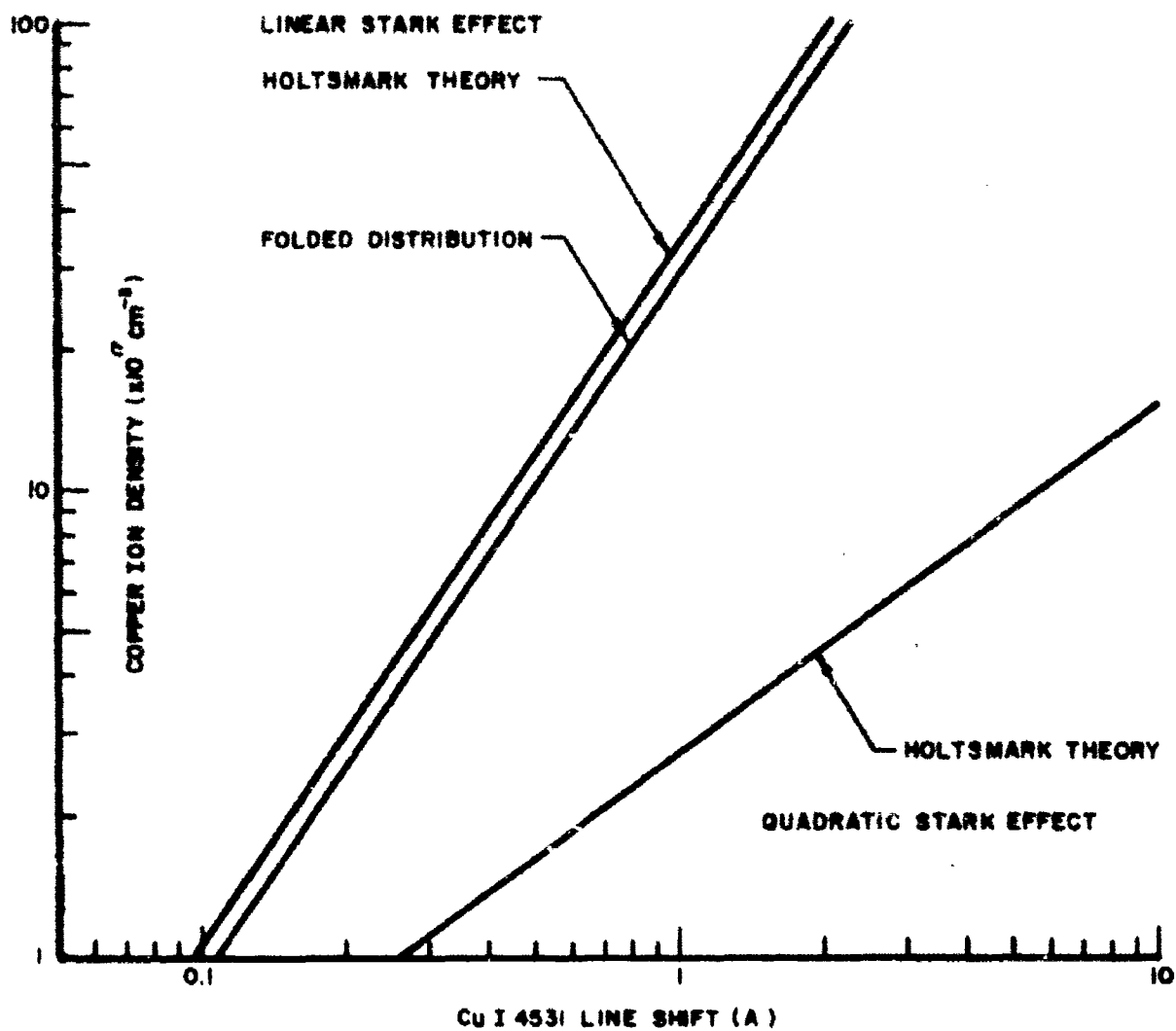


FIG. 27. VARIATION OF CUI 4531 LINE SHIFT WITH PLASMA ION DENSITY



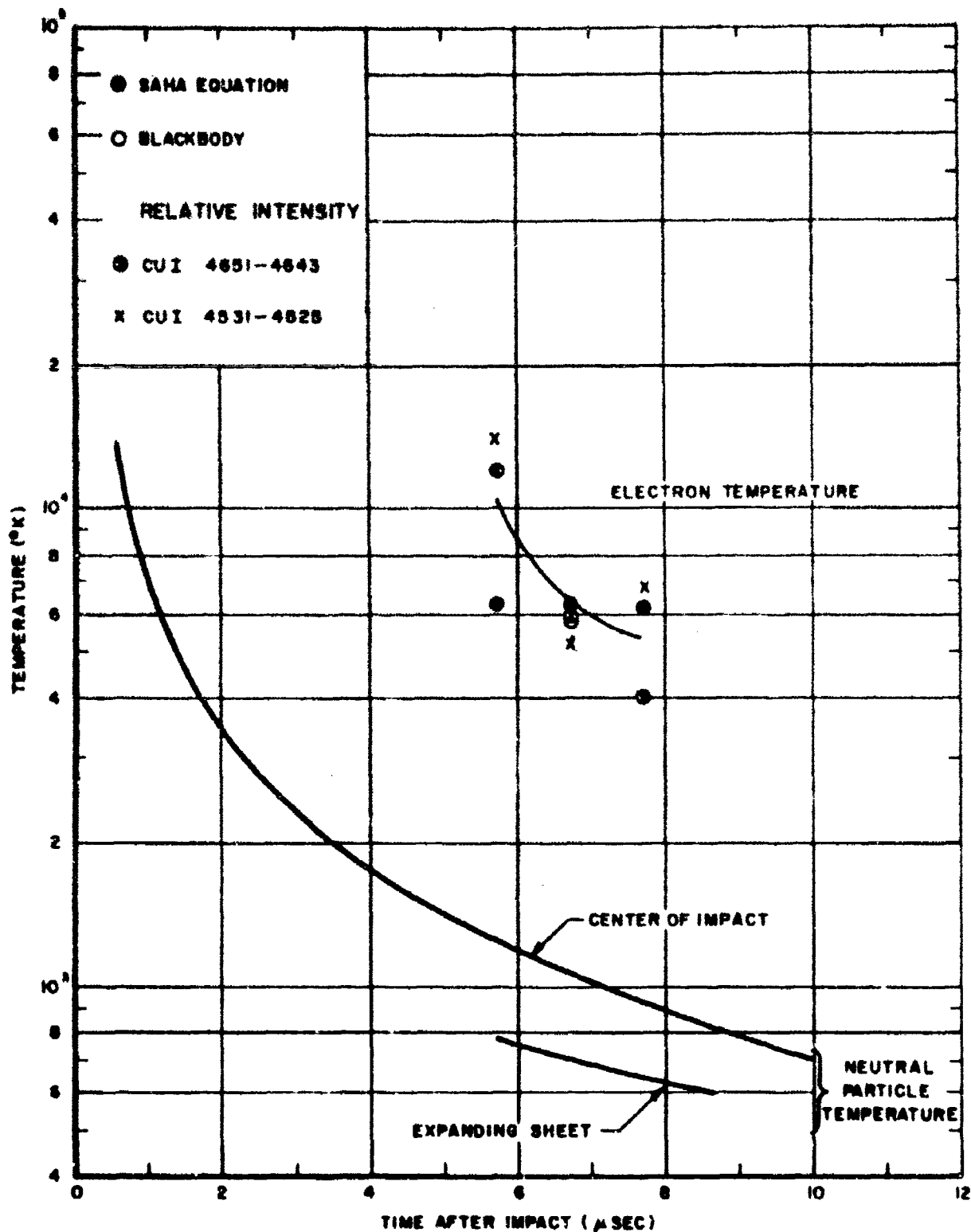


FIG. 28. TIME VARIATION OF JET COLLISION PLASMA TEMPERATURE

## APPENDIX A

## Summary of Experimental Firings

## (a) Jet Collision Experiments

Firing no.	Date	Camera* Coverage	Objectives and Comments
55	5 Jan 1960	F, S	observe an explosively driven hypervelocity pellet
56	6 Jan 1960	F	observe a single shaped charge jet; establish a time sequence of events
57	6 Jan 1960	F, S	observe a jet collision in air
58	15 Jan 1960	F	observe the collision of two hypervelocity pellets
59	15 Jan 1960	F, S	repeat of firing no. 57
69	19 Feb 1960	F, S	repeat of firing no. 58
70	19 Feb 1960	F, S	repeat of firing no. 58
77	14 Apr 1960	F	repeat of firing no. 57 charges aligned with collapsible rod
78	14 Apr 1960	F	repeat of firing no. 77; baffles added to delay reaction products

\*F: framing camera

S: streak camera

I: time-integrating spectrograph

R: time-resolved spectrograph

## APPENDIX A

## Summary of Experimental Firings

## (a) Jet Collision Experiments

Firing no.	Date	Camera* Coverage	Objectives and Comments
79	18 Apr 1960	F, S	repeat of firing no. 78
80	18 Apr 1960	F, S	repeat of firing no. 78
81	18 Apr 1960	F	observe collision in propane atmosphere
86	9 May 1960	F	repeat of firing no. 81
87	9 May 1960	F	repeat of firing no. 81
97	29 Mar 1961	F	observe jet collision in low pressure propane atmosphere, in a small diameter vacuum chamber
98	29 Mar 1961	F	repeat of firing no. 97
99	15 Apr 1961	F, S, I	obtain a time-integrated spectrum of a jet collision in air
100	27 Apr 1961	F, S, I	obtain a time-integrated spectrum of a jet collision in a low pressure propane atmosphere
109	30 Jan 1962	F, I, R	obtain a time-resolved spectrum of a jet collision in a low pressure helium atmosphere
110	10 Apr 1962	F, I, R	repeat of firing no. 109 in a small diameter vacuum chamber

# APPENDIX A

## Summary of Experimental Firings

### (a) Jet Collision Experiments

Firing no.	Date	Camera* Coverage	Objectives and Comments
111	15 May 1962	F, I, R	repeat of firing no. 110
112	30 Jul 1962	F, I, R	observe a jet collision in air using smaller shaped charges
113	13 Aug 1962	F, I, R	repeat of firing no. 112
114	16 Aug 1962	F, I, R	repeat of firing no. 112
115	24 Oct 1962	F, I, R	repeat of firing no. 110
122	19 Jun 1963	F, I, R	repeat of firing no. 110
123	20 Jun 1963	F, I, R	repeat of firing no. 110
124	27 Jun 1963	F, I, R	repeat of firing no. 109
125	29 Jun 1963	F, I, R	repeat of firing no. 109; shifted spectral range covered on time-resolved record
126	4 Oct 1963	F, I, R	repeat of firing no. 125, added instrumentation to measure arrival time of collision sheet at vacuum chamber wall

# APPENDIX A

## Summary of Experimental Firings

### (c) Jet-Target Impact Experiments

Firing no.	Date	Camera* Coverage	Objectives and Comments
101	9 May 1961	F, I	observe jet impact with massive, stationary copper target in a low pressure propane atmosphere
103	1 Sep 1961	F, I, R	repeat of firing no. 101; obtain a time-resolved spectrum of a jet-target impact
119	11 Dec 1962	F, I, R	repeat of firing no. 103, in a low pressure helium atmosphere
120	14 Feb 1963	F, I, R	repeat of firing no. 119
121	25 Apr 1963	F, I, R	repeat of firing no. 119

## APPENDIX B

### Direct-Vision Prism and Streak Camera Combination

A discussion of the direct-vision prism and Beckman and Whitley streak camera used in combination as a time-resolving spectrograph is contained in the following paper.

**BLANK PAGE**

## Time-Resolved Spectroscopy of High Speed Events\*

FRANK R. SCHWARTZ

*Explosives Research Section, Picatinny Arsenal, Dover, New Jersey*

AND

BENJAMIN J. PERNICK

*Siemens Institute of Technology, Hoboken, New Jersey*

(Received April 20, 1962)

THE time-resolved spectral information relating to highly transient, self-luminous phenomena over selective spectral ranges in the visible region can be readily obtained with a high speed streak camera by the simple addition of a direct-view prism into the existing entrance optics of the camera system. This technique has been employed here in observing spectral variations with respect to time of such luminous events as exploding wires, hypervelocity impact, and detonating high explosives.

The optical arrangement utilized is shown in Fig. 1. Light from a source is focused on an adjustable slit. The slit is positioned at the focal point of a 7 in.,  $f/2.5$  lens, which in conjunction with the objective lens of a Beckman-Whitley continuous writing streak camera forms a collimating optical system. A Leybold 20×20 mm direct-view prism, inserted between the lenses, disperses the light from the first collimating lens. A dove prism is used with the direct-view prism to facilitate preliminary adjustments and alignment so as to obtain the desired spectral range on the film record. Inclusion of the direct-view and dove prisms reduces the optical speed of the original system from  $f/5$  to about  $f/25$ . The spectral region that can be covered with

the above optical arrangement extends from about 4000 to 6500 Å.

Figure 2 is a film record that illustrates the spectral variations in time of a gold wire (99.99% pure) 0.0015 in. in diameter and 0.040 in. long, when exploded by a 4-kV pulse. The writing speed of the camera is 1.0 mm/ $\mu$ sec. Calibration lines from helium and zinc spectral lamps are also included on the same film strip. The wavelength region shown here is from 4400 to 5300 Å, which lies within the spectral sensitivity range of the Kodak 35-mm Tri-X film used. The maximum spectral resolution within this range is about 2 Å.

The calibration lines on the film strip are images of the full entrance slit. Thus, for broad sources that fully illuminate the entrance slit, the observed slit length corresponds to a writing time or time response of 1.8  $\mu$ sec at 1-mm/ $\mu$ sec writing speed<sup>1</sup> (i.e., the slit image will completely pass over a given point of the film in this time interval).

For the situation illustrated in Fig. 2, however, the time response is much smaller. The length of gold wire is oriented perpendicular to the entrance slit; hence, during the various stages of wire explosion the slit is not completely il-

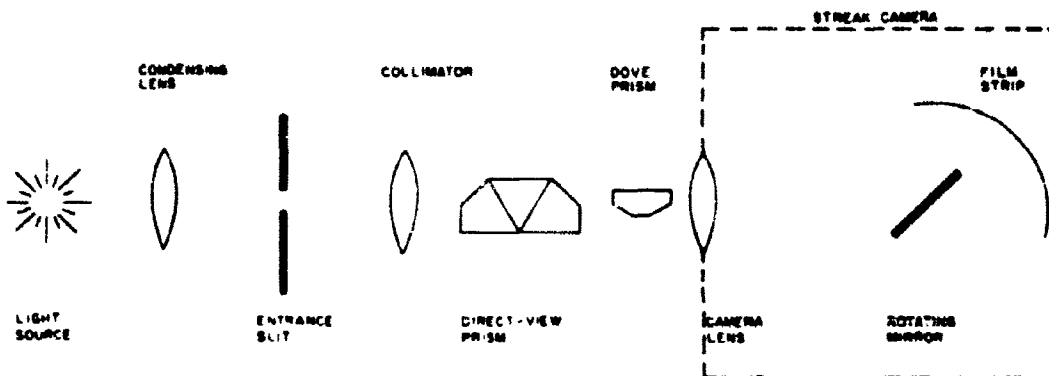


FIG. 1. Schematic of optical arrangement.



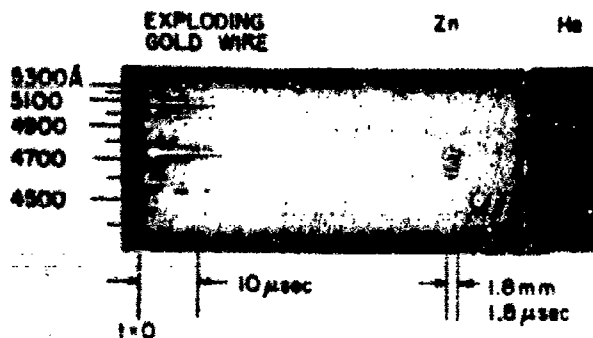


FIG. 2. Time-resolved spectrum of exploding gold wire with He and Zn calibration lines. (Writing rate, 1.0 mm/μsec.)

luminated. The time response in this case is related to the diameter of the expanding luminous region about the exploding wire rather than to the slit length.

For applications in which a spectral resolution of the

order of an angstrom over a visible range of the order of 1000 Å is of interest, the direct-view prism method for time-resolved spectroscopy is advantageous. The prism can be readily added to the optical train of most high-speed cameras without the use of additional optical equipment. Light transmission losses through the prism and reduced optical speed of the camera system have presented no difficulties for the highly luminous sources employed here.

This work was undertaken as part of a research program in explosive study. We would like to thank Dr. S. J. Lukasik of Stevens Institute of Technology and Dr. S. Koslov of Vitro Laboratories for their continued help and guidance. We are also grateful to personnel at Picatinny Arsenal for providing the necessary facilities and permission to publish this note.

\* Work supported by the Ordnance Corps, U. S. Army.

† G. E. Seay, L. B. Seely, Jr., and R. G. Fowler, J. Appl. Phys. 32, 2439 (1961).

## APPENDIX C

## Spectral Line Profile Program

A line profile is generated from densitometer measurements with the use of the spectral line profile program listed below. In brief, the program converts horizontal and vertical position measurements on a densitometer scan into wavelength and intensity values respectively. The line profile, given by eq (2-4) is then constructed by subtracting the background intensity from the total observed intensity at each wavelength step.

The input quantity TIME labels the program output with the time after first impact light at which the film record was scanned. A density scale calibration is established from a quadratic least squares fit of known density steps  $D(i)$ , and the corresponding densitometer displacements  $Y(i)$ . A listing of the subroutine POLYFT which performs the least squares fit is also included below. As a check on the reliability of the fit, density values  $DEV(i)$ , are computed from the input densitometer displacements  $Y(i)$ , and compared with the known density steps  $D(i)$ . A wavelength scale is constructed from the horizontal position measurements  $POS(i)$ , of several lines on the densitometer record with known wavelength  $WLT(i)$ , and wavenumber  $WNO(i)$ . All position measurements are with respect to an arbitrary zero reference point in the horizontal direction. The subroutine POLYFT is again used to obtain a quadratic least squares fit between the variables  $POS(i)$  and  $WNO(i)$ . Similarly the reliability of the fit is checked by comparing wavenumbers  $DIFF(i)$  computed from the input position measurements  $POS(i)$  with the known wavenumbers  $WNO(i)$ .

Each spectral line is labeled by the wavelength value of the line

center LWAVE. The number of input points used to describe the line profile is called  $L$ . Three variables define an input point; namely  $X(i)$  the horizontal position,  $YC(i)$  the vertical position of the background density, and  $YT(i)$  the vertical position of the total density. Since the length of a densitometer record exceeds the horizontal scale of the Gerber scanner, the scanning device must be translated in order to read all necessary points on the densitometer record. Thus one cannot directly obtain the required continuous sequence of values for the variable  $X(i)$ , measured from the arbitrary zero reference point, over the full range of the densitometer record. This difficulty does not occur for y-position measurements since the width of the densitometer record is easily accommodated by the scanner.

A uniform X-scale is obtained in the following manner. The current value of  $X(i)$  is compared with the previous value, i.e.  $X(i)$ -STORE. If there has been no translation of the Gerber scanning device  $X(i)$  will be numerically greater than the quantity STORE. Alternately if  $X(i)$  is less than STORE, a translation has been made. The amount by which the scanning device has moved, called SHIFT, is then added to the current value and all subsequent values of  $X(i)$ , i.e.  $X(i) = X(i) + \text{SHIFT}$ . Any number of translations of the Gerber scanner can be handled in this fashion. However, this procedure places restrictions on the manner in which the Gerber translations are made. First, one must ascertain that the last  $X(i)$  value read before translating is greater than the next  $X(i)$  value to be read. Also the amount of translation is not arbitrary. The scanning device is relocated so that the last X-position read becomes the starting point of subsequent readings.

After converting all  $X(i)$  values for a given spectral line into a continuous sequence the corresponding wavenumbers  $WAVEK(i)$ , and wavelengths  $WAVEL(i)$  are computed. The spectral line intensity at each wavelength is then calculated. The total density is found from  $YT(i)$ , and the background density from  $YC(i)$ . For a given value of the photometric slope  $GAMMA(J)$ , the line intensity  $BRITL(i)$  is found in accord with eq (2-4). The maximum value  $BRITH$ , of the quantities  $BRITL(i)$  is then obtained and all  $BRITL(i)$  values are normalized by division with  $BRITH$ . The wavelength at which the line intensity is a maximum is called  $WLMX$ . The output of the program consists of the quantities  $BRITL(i)$  and  $DEL(i)$ , where  $BRITL(i)$  is the normalized spectral line intensity and  $DEL(i)$  the wavelength difference from the position of maximum intensity. These latter computations are then repeated for the  $K$  values of  $GAMMA(J)$ . After completion of these spectral line profiles for a given line the program is ready to similarly process the next set of densitometer input points.

**BLANK PAGE**

```

C   SPECTRAL LINE PROFILE MK6
C   USES SUBROUTINE POLYFIT
      DIMENSION D( 40), Y( 40), A(3), DEV(40), POS( 40),
X   WAVEK(150), WAVE(150), BRITL(150), B(3),
X   DEL(150), WVLT(40), WVNO(40), X(150), YC(150), YT(150) ,
X   GAMMA(5) , COEFF(5) ,DIFF(40)
      COMMON Y, D, COEFF
      EQUIVALENCE (Y, POS ) , (D, WVNO )
      EQUIVALENCE ( DEV, DIFF, WAVEK, DEL )
      EQUIVALENCE (X, WAVE ) , ( YC, BRITL )
1   READ 86, TIME
      PUNCH 86, TIME
      PUNCH 96
      READ 89, DUMMY, N, M
      DO 2 I=1, N
2   READ 98, D(1), Y(1)
      CALL POLYFT (Y,D,2,N,COEFF)
      A(1) = COEFF(1)
      A(2) = COEFF(2)
      A(3) = COEFF(3)
      DO 5 I = 1, N
      DEV(I) = A(1) + A(2) *Y(1) +A(3)*Y(1)*Y(1)
      DEV(I) = D(1) - DEV(I)
5   PUNCH 98, D(1), Y(1), DEV(I)
      PUNCH 95, A(1), A(2), A(3)
      PUNCH 96
      DO 6 I = 1, M
6   READ 93, POS(1), WVLT(1), WVNO(1)
      CALL POLYFT (POS,WVNO,2,M,COEFF)
      B(1) = COEFF(1)
      B(2) = COEFF(2)
      B(3) = COEFF(3)
      DO 11 I = 1, M
      DIFF(I)=B(1) + B(2)*POS(1) + B(3)*POS(1)*POS(1)
      DIFF(I) = WVNO(1) - DIFF(I)
11  PUNCH 93, POS(1), WVLT(1), WVNO(1), DIFF(1)
      PUNCH 95, B(1), B(2), B(3)
      PUNCH 96
      STORE = 0.0
      SHIFT = 0.0
      READ 89, DUMMI, K
21  READ 90, LWAVE, L
      PUNCH 90, LWAVE
      PUNCH 96
      DO 22 I=1, L
22  READ 86, X(1), YC(1), YT(1)
      DO 26 I=1,L
      IF( X(1) - STORE ) 24, 24, 23
24  SHIFT = SHIFT + STORE
23  STORE = X(1)
      X(1) = X(1) + SHIFT
      WAVEK(1) = B(1) + B(2)*X(1) + B(3)*X(1)*X(1)
26  WAVE(1) = 1.0/WAVEK(1)
      PUNCH 95, STORE , SHIFT
      PUNCH 96
      DO 39 J = 1, K
      READ 89, GAMMA(J)
      PUNCH 89, GAMMA(J)
      PUNCH 96
      DO 12 I = 1, L
12  BRITL(I)=EXP((A(1)+A(2)*YT(1)+A(3)*YT(1)*YT(1) )/

```

```

X (GAMMA(J)*0.43429)) -
X EXPF((A(1)+A(2)*YC(1)+A(3)*YC(1)*YC(1)) /
X (GAMMA(J)*0.43429))
BRITM = BRITL(1)
WVLMX = WAVEL(1)
DO 42 I = 2, L
  IF ( BRITM - BRITL(I) ) 41, 42, 42
41 BRITM = BRITL(I)
  WVLMX = WAVEL(I)
42 CONTINUE
DO 33 I = 1, L
  BRITL(I) = BRITL(I)/BRITM
  DEL(I)=WAVEL(I)-WVLMX
33 PUNCH 85, WAVEL(I), DEL(I), BRITL(I)
  PUNCH 96
39 PUNCH 96
  GO TO 21
86 FORMAT ( 3F9.3)
89 FORMAT ( F10.5, 2I5 )
98 FORMAT ( F8.2, F11.3, F8.3 )
96 FORMAT (/)
95 FORMAT ( 3E20.7 )
93 FORMAT ( F10.3, 3F12.3 )
85 FORMAT ( 2E20.4, E20.8 )
90 FORMAT ( 114, 15 )
  END

```

```

SUBROUTINE POLYFT(X,Y,K,N,C)
C      PUT DATA POINTS AND FINAL COEFFICIENTS IN COMMON
      DIMENSION X( 40),Y( 40),B(5),S(4),A(5,5),C(5)
      COMMON X,Y,C
      CN=N
      K1=K+1
      DO 2 J=2,K1
        J2=J-1
        DO 1 I=1,J2
1      A(J,I)=0.0
        A(J2,J)=0.0
2      A(J,J)=1.0
        A(1,I)=1.0
        B(1)=0.0
        DO 3 I=1,N
3      B(1)=B(1)+Y(I)
        B(1)=B(1)/CN
        ALF=0.0
        DO 4 I=1,N
4      ALF=ALF+X(I)
        A(2,I)=-ALF/CN
        Q=0.0
        S(1)=0.0
        B(2)=0.0
        DO 5 I=1,N
        P=A(2,I)+X(I)
        Q=Q+X(I)*P*P
        S(1)=S(1)+P*P
5      B(2)=B(2)+Y(I)*P
        B(2)=B(2)/S(1)
        ALF=Q/S(1)
        BETA=S(1)/CN
        IF(K-2)11,6,6
6      DO 10 M=2,K
        M1=M+1
        M2=M-1
        A(M1,1)=-ALF*A(M,1)-BETA*A(M2,1)
        DO 7 J=2,M
        J2=J-1
7      A(M1,J)=A(M,J2)-ALF*A(M,J)-BETA*A(M2,J)
        S(M)=0.0
        Q=0.0
        R=0.0
        DO 9 I=1,N
        P=1.0
        DO 8 L=1,M
        NL=M1-L
8      P=P*X(I)+A(M1,NL)
        Q=Q+X(I)*P*P
        R=R+Y(I)*P
9      S(M)=S(M)+P*P
        ALF=Q/S(M)
        BETA=S(M)/S(M2)
10     B(M1)=R/S(M)
11     DO 12 L=1,K1
        C(L)=0.0
        DO 12 L1=L,K1
12     C(L)=C(L)+B(L1)*A(L1,L)
      RETURN
      END

```



**BLANK PAGE**

## APPENDIX D

### Photometric Emulsion Calibration

A rotating step-sector wheel method was used to obtain the photometric emulsion calibration of the time-resolved spectral film records. The experimental arrangement employed is shown schematically in Fig. D-1. Light from a spectral lamp source interrupted by a rotating step-sector wheel is focused on a rectangular slit. To provide for uniform illumination over the slit the magnification is such that only a small central region of the extended light source is projected. The slit is viewed by the direct vision prism-streak camera optical train (see Appendix B) with the narrow width spectrograph entrance slit removed. To vary the total exposure time of a calibration run a manually-operated shutter is inserted in the optical system as indicated in the figure. The streak camera mirror is stationary during the calibration exposure in order to obtain static images of the slit.

The step-wise variations in exposure along the length of an image are determined by the rotating sector wheel geometry and the total exposure time. From eq (2-10a) the film exposure at a given point on the image can be expressed as

$$\Phi = \int_t \int_{\Delta} J(v') dv' dt \quad (D-1)$$

where  $J(v')$  is the profile of a spectral line from the source lamp,  $\Delta$  is the slit image width (see Appendix E), and  $t$  is an effective exposure time.  $t$  is determined by the time per revolution of the sector wheel during which a portion of the slit is uncovered, and the length of time the mechanical shutter is kept open. If  $t_s$  is the time per

revolution of the sector wheel at a given step,  $F$  the rotational frequency, and  $t_e$  the total exposure time of the manual shutter, then the effective exposure time is simply the product  $t_s F t_e$ .

Since the source light is steady in time, one has

$$\bar{I} = t_s F t_e \int_{\Delta} J(\nu') d\nu' \quad (D-2)$$

If the slit image width is very large in comparison with the width of the spectral line then the film response at each step exposure is given by

$$\bar{I} \approx I F t_s t_e \quad (D-3)$$

where  $I$  represents the total line intensity, i.e.

$$I = \int_0^{\infty} J(\nu') d\nu'$$

The total line intensity and rotational frequency are constant for a given calibration run. For the sector wheel used in the calibrations, successive values of  $t_s$  are in the ratio 2 to 1. The manually controlled exposure times were chosen so as to cover a broad range of density values on the film record, from about 0.05 to 1.7 density units.

The measured variations of film density with relative exposure for a zinc spectral line are illustrated in Fig. D-2. Density values were obtained from densitometer readings of the slit image and relative exposure values derived from eq (D-3). Measurements corresponding to different total exposure times  $t_e$ , are distinguished in the figure. Over a density range from about 0.1 to 1.2 the density values vary linearly with the logarithm of the relative exposure, i.e.

$$D = Y \log \bar{I} + \text{const} \quad (D-4)$$

The slope  $\gamma$  is determined from a least squares fit to the data points. A summary of the values of  $\gamma$  obtained in this manner is presented in Table V. The density values for the observed spectral lines were within this linear density range.

**BLANK PAGE**

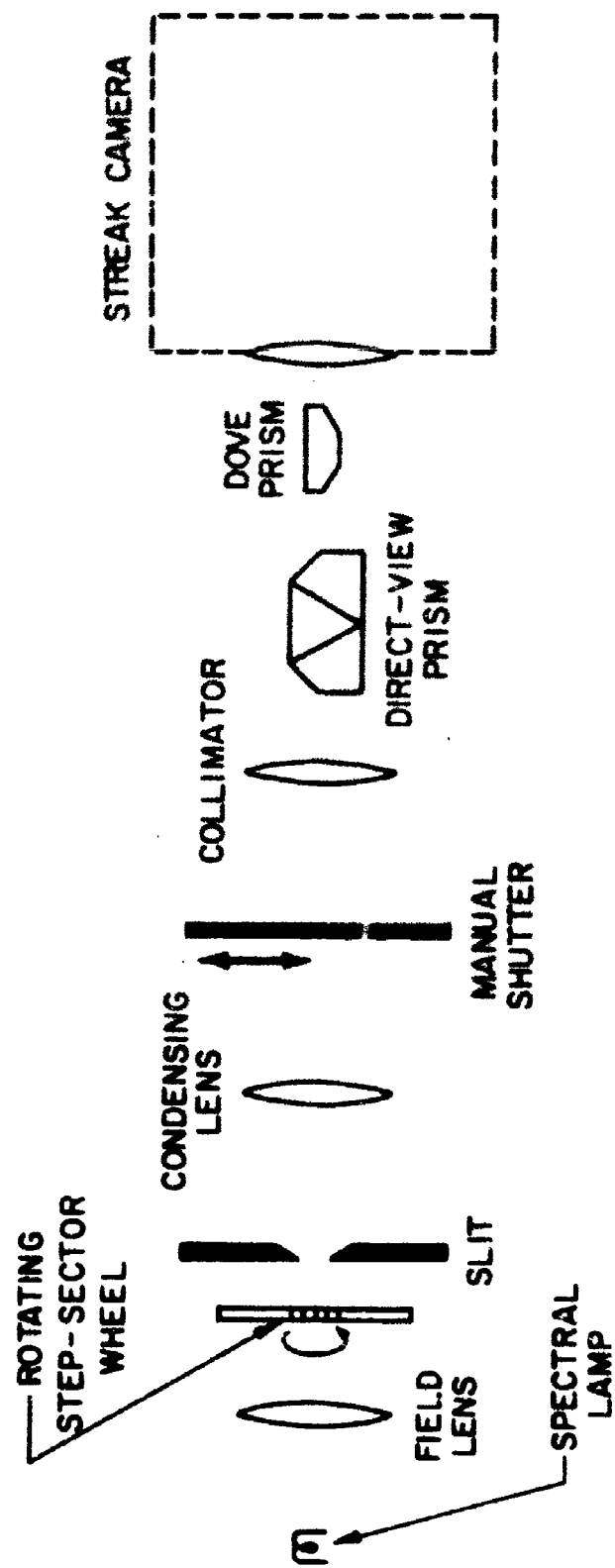


FIG D-1. PHOTOMETRIC EMULSION CALIBRATION SETUP

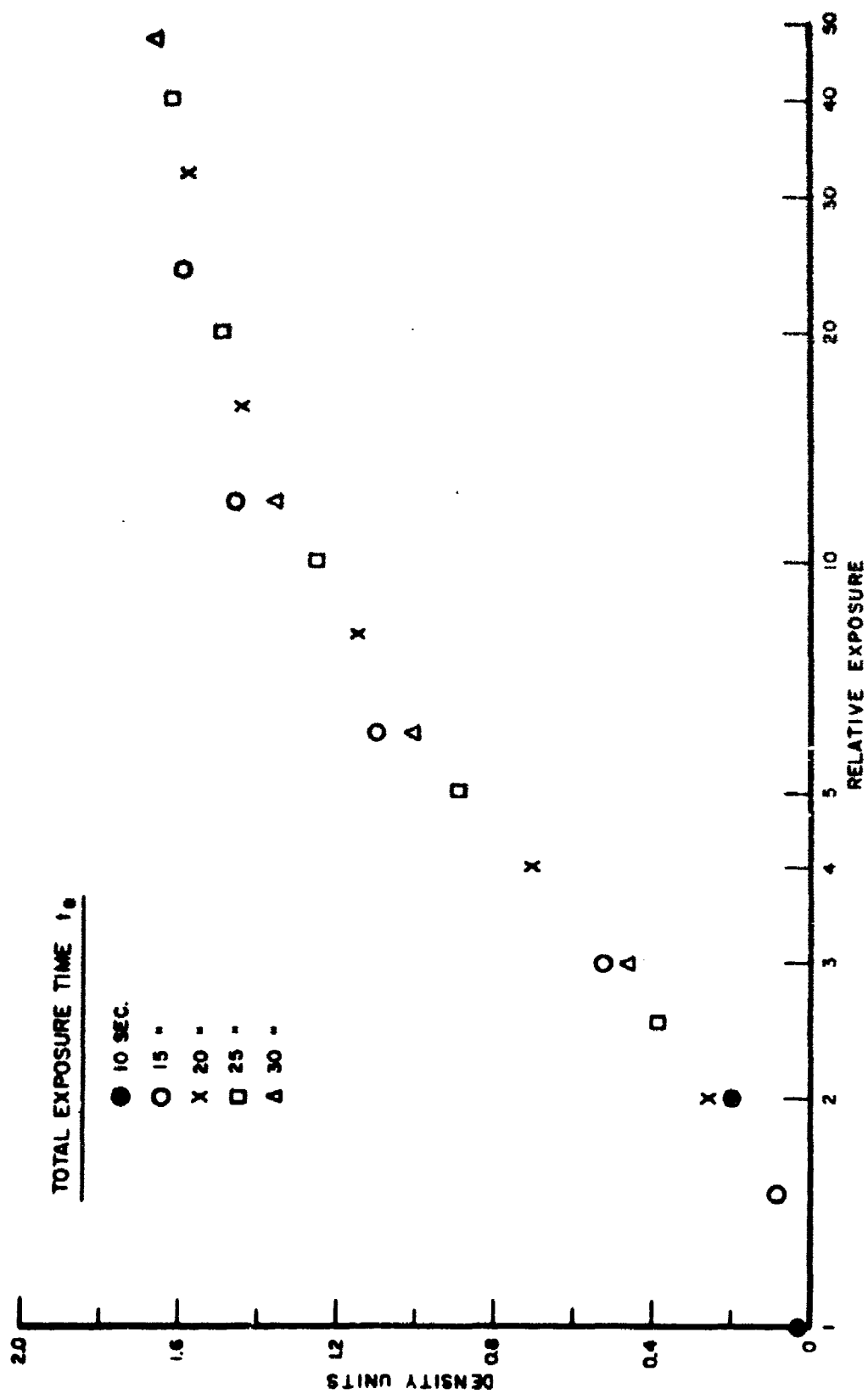


FIG.D-2. PHOTOMETRIC EMULSION CALIBRATION

## APPENDIX E

## Spectrograph Slit Image Width Calculations

Numerical estimates of the width of the spectrograph entrance slit image were obtained from an optical ray trace analysis of the direct vision prism streak camera combination. Principal rays originating from the entrance slit are deviated by the prism and focused at the image plane of the streak camera, thereby defining the slit image width. Since the deviations of these principal rays are wavelength dependent, the variation of slit image width with wavelength is calculated over the spectral range encompassed by the time-resolved spectral records.

Consider the ray diagram illustrated in Fig E-1. A ray from the center and from the edge of the entrance slit are followed through the collimator lens, direct vision prism, and telescope lens of the streak camera. The total width of the entrance slit is called  $S$ , the focal lengths of the collimator and telescope lens are  $f_1, f_2$  respectively, and the total slit image width is  $\Delta$ . The prism angles  $\alpha_c, \alpha_f, \Sigma$  and interface angles of importance indicated by other greek letter symbols are also given in the figure. The subscript 1 refers to interface angles associated with the ray from the entrance slit center, and similarly the subscript 2 is applied to angles associated with the ray from the entrance slit edge. The index of refraction of the identical outer crown glass prisms is called  $n_c$ , and for the middle flint glass prism,  $n_f$ . At the wavelength for zero deviation



the slit image is centered about the point located at  $O'$  in the image plane. For other wavelengths the slit image is located at a typical point  $x$  as illustrated. The angular deviation of the center ray from the principal axis is denoted by  $\Psi$ .

The following angular relations can be readily derived

$$\tan \theta_1 = S/2f_1$$

$$\theta_1 = x_1 - x_2$$

$$\sin x_1 = n_c \sin \zeta_1$$

$$\sin x_2 = n_c \sin \zeta_2$$

$$\zeta_1 + \eta_1 = \alpha_c$$

$$\zeta_2 + \eta_2 = \alpha_c$$

$$\sin \eta_1 = (n_F/n_c) \times \sin \xi_1$$

$$\sin \eta_2 = (n_F/n_c) \times \sin \xi_2$$

$$\xi_1 + \epsilon_1 = \alpha_F$$

$$\xi_2 + \epsilon_2 = \alpha_F$$

$$(n_F/n_c) \times \sin \epsilon_1 = \sin \delta_1$$

$$(n_F/n_c) \times \sin \epsilon_2 = \sin \delta_2$$

$$\delta_1 + \gamma_1 = \alpha_c$$

$$\delta_2 + \gamma_2 = \alpha_c$$

$$n_c \sin \gamma_1 = \sin \beta_1$$

$$n_c \sin \gamma_2 = \sin \beta_2$$

$$\theta_2 = \beta_2 - \beta_1$$

$$\Psi = \Sigma + \beta_1 - 190^\circ$$

The position of the slit image center is given by

$$x = f_2 \tan \gamma$$

The edge of the slit image is at a position

$$x + \Delta/2 = f_2 \tan (\gamma + \theta_2)$$

Hence the slit width  $\Delta$ , is given by

$$\Delta = 2 f_2 (\tan (\gamma + \theta_2) - \tan \gamma)$$

Numerical solutions of the above set of equations were performed with the use of the Slit Function Estimate program given below. Variables in the program are associated with terms in the above equations as follows.

F1,F2	focal lengths $f_1, f_2$
S	entrance slit width, $S$
ALPC,ALPF, SIGMA	prism angles, $\alpha_c, \alpha_f, \Sigma$
X1	angle of incidence, $\chi_1$
REFC, REFF	indices of refraction, $n_c, n_f$
WAVEL	wavelength
Z	$C$
ETA	$\eta$
SE	$\xi$
EPS	$\epsilon$
DELTA	$\delta$
GAMMA	$\gamma$
BETA	$\beta$
THET I	$\theta_1$
X2	$\chi_2$

PS1	$\Psi$
THET2	$\theta_2$
PHI	$\Psi + \theta_2$
DISP	$x$
DISPL	$x + \Delta/2$
SLIT	$\Delta/2$

The program systematically evaluates the angles from the above equations, first for the principal ray from the entrance slit center (i.e. BETA1, DELT1, etc.), and then for the principal ray from the entrance slit edge (i.e. BETA2, DELT2, etc.). The angular deviations  $\Psi$  and  $\Psi + \theta_2$  are then computed. The slit image center position DISP, the edge position DISPL, and finally the slit width SLIT at the wavelength WAVEL are obtained as part of the program output. These calculations are repeated at wavelengths for which refractive index data are available.

A dispersion curve is constructed from the above calculated DISP and WAVEL values with the use of the Least Squares Fitting of Slit Function program and LSQF subroutine listed below. This is a necessary step since the calculated SLIT values are in units of length in the image plane and must be converted to wavelength units by means of a dispersion curve. Also the calculated dispersion curve can be compared with an experimental calibration to provide a check on the ray-tracing calculations. The above calculated values of DISP, SLIT, and WAVEL are used as input information to these fitting programs and appear as dimensioned variables. For convenient numerical calculations a least squares polynomial fit is used to represent the functional dependence between wavelength and position in the image plane. A

least squares fit of order  $M$  of the quantities  $FRQ(I)$  and  $DISP(I)$  is obtained, where  $FRQ(I)$  is the wavenumber equivalent of  $WAVEL(I)$ . By comparing deviations in calculated and input wavelengths, i.e.  $DIF = WL - WAVEL(I)$ , for various values of the order of the fit  $M$ , a best value of  $M$  is obtained. A value of  $M$  equal to 4 was found to yield the best fit polynomial in the numerical computations.

The slit image width in wavelength units is then obtained with the use of this fourth-order polynomial representation of the dispersion curve. The position of the center of the slit image  $DISP(I)$  has a calculated equivalent wavelength value  $WL$ . Similarly the position of the edge of the slit image  $DISPL$  has an equivalent wavelength value  $WPL$ . The difference  $WPL - WL$  gives the slit image width in wavelength units  $DELW$ .

Numerical estimates of the slit image width were computed using refractive index data supplied by the prism manufacturer, measured prism angles, and known collimator and telescope lens focal lengths. These data are presented in Table E-1. The entrance slit width  $S$  and the angle of incidence  $\chi_1$  were treated as parameters and varied about their nominally known values. The slit image width was calculated at those wavelengths for which refractive indices were known. Results of the computations are given in Table E-II and illustrated in Fig. 17. Angular deviations of  $\pm 1^\circ$  about a nominal  $32.5^\circ$  incidence angle were considered representative of the uncertainty in the alignment of the direct vision prism in the optical train. The slit image width was computed for several values of the entrance slit width at each value of the incidence angle. The calculated position

of the center of the slit image  $x_c$ , at each wavelength is also indicated in the table.

Calculated wavelength positions  $x_c$ , were compared with measured positions obtained from a densitometer trace of the copper spark spectrum, originally used for wavelength identification on the time-resolved spectral record. This would provide a check on the ray-tracing computations. The calculated position values given in Table E-II were transformed to the position scale of the densitometer trace. A linear transformation was used since the densitometer scan represents a magnification of the original film record. A dispersion curve was then constructed from a least squares fit using these adjusted position values. Table E-III gives the calculated position for various wavelengths in the 4500-5300A range obtained from the dispersion curve, and the corresponding position from densitometer trace measurements. These results are seen to be in close agreement. The lack of systematic variation between the calculated and measured position values is to be noted. The differences given in Table E-III appear to oscillate about a zero mean. This is further indication that the approximations and numerical estimates employed in the calculations are realistic and that the slit image width estimates are reasonably good.

TABLE E-1

## Refractive Index Values

Wavelength (Å)	Crown	Flint
4047	1.53022	1.65071
4358	1.52667	1.64206
4800	1.52282	1.63312
4861	1.52236	1.63210
5461	1.51871	1.62410
5876	1.51680	1.62004
5893	1.51671	1.61992
6438	1.51471	1.61583
6563	1.51431	1.61504

## Prism Angles (deg)

 $\alpha_c$  98.5

 $\alpha_F$  132

 $\Sigma$  57.5

## Focal Lengths (in.)

 $f_1$  7

 $f_2$  12

TABLE E-11

Variation of Slit Image Width with Wavelength

Angle of Incidence $\alpha_i$ (deg)	Wavelength (A)	Image Position $x$ (mm)	Total Slit Width $\Delta$ (mm)	
			$S = 0.075\text{mm}$	$S = 0.100\text{mm}$
31.5	4047	-37.9	2.1	2.8
	4358	-20.2	3.3	4.4
	4800	- 5.5	5.0	6.6
	4861	- 4.0	5.2	7.0
	5461	7.1	8.5	11.4
	5876	12.2	11.5	15.2
	5893	12.2	11.5	15.2
	6438	17.0	15.9	21.1
	6563	17.8	16.7	22.3
32.5	4047	-45.6	2.1	2.7
	4358	-26.4	3.5	4.6
	4800	-11.0	5.2	6.8
	4861	- 9.4	5.4	7.2
	5461	1.9	8.8	11.7
	5876	7.2	11.8	15.7
	5893	7.2	11.9	15.9
	6438	12.1	16.1	21.5
	6563	12.9	17.3	23.0
33.5	4047	-54.7	2.0	2.7
	4358	-33.3	3.6	4.8
	4800	-16.9	5.3	7.1
	4861	-15.3	5.6	7.4
	5461	- 3.5	9.0	12.0
	5876	1.9	12.1	16.2
	5893	1.9	12.1	16.2
	6438	6.9	16.8	22.4
	6563	7.8	17.7	23.7

TABLE E-III

## Calculated and Measured Wavelength Position Comparison

Angle of Incidence $\chi_1$ (deg)	Wavelength (Å)	Position*		Difference (arb. units)
		Calc.	Meas.	
31.5	4500	5.46	5.30	0.16
	4600	7.73	7.85	-0.12
	4700	9.78	9.90	-0.12
	4800	11.62	11.65	-0.03
	4900	13.27	13.25	0.02
	5000	14.73	14.65	0.08
	5100	16.02	15.95	0.07
	5200	17.15	17.10	0.05
	5300	18.14	18.23	-0.09
32.5	4500	5.42	5.30	0.12
	4600	7.72	7.85	-0.13
	4700	9.79	9.90	-0.11
	4800	11.65	11.65	0.00
	4900	13.29	13.25	0.04
	5000	14.75	14.65	0.10
	5100	16.02	15.95	-0.07
	5200	17.14	17.10	0.04
	5300	18.10	18.23	-0.13
33.5	4500	5.37	5.30	0.07
	4600	7.72	7.85	-0.13
	4700	9.81	9.90	-0.09
	4800	11.68	11.65	0.03
	4900	13.33	13.25	0.07
	5000	14.77	14.65	0.12
	5100	16.03	15.95	0.08
	5200	17.12	17.10	0.01
	5300	18.05	18.23	-0.18

\* Position on a densitometer trace.



**BLANK PAGE**

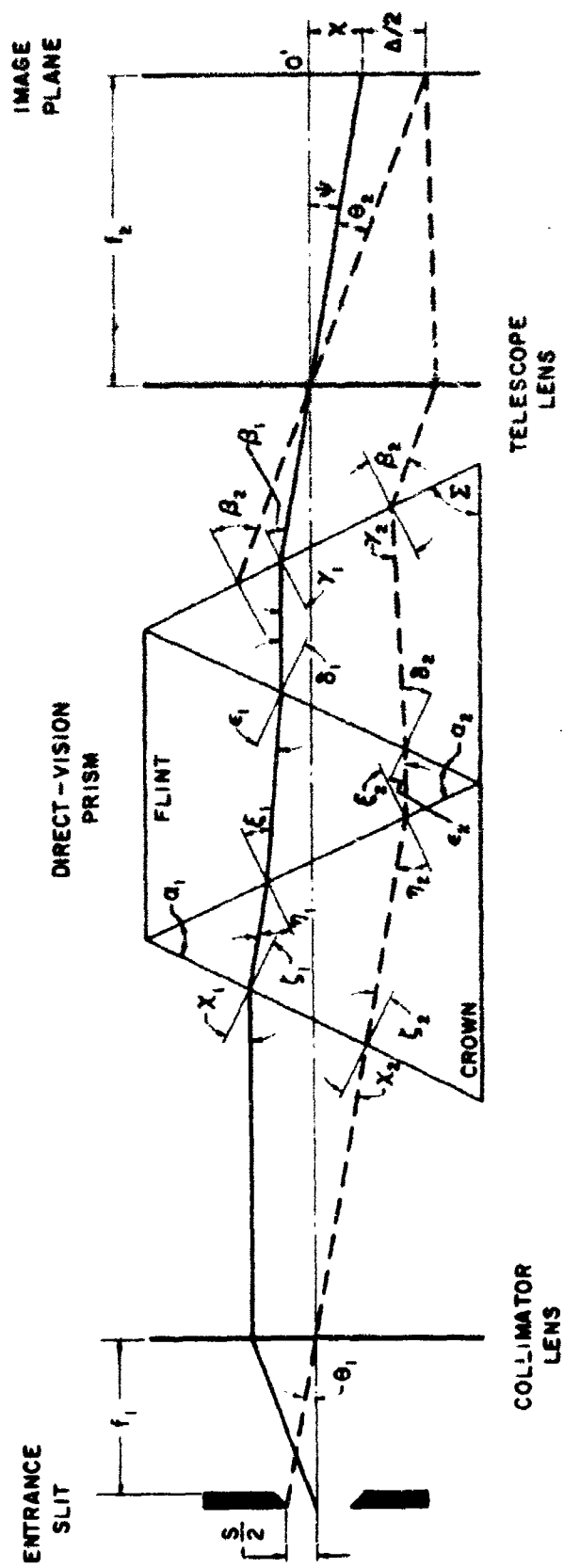


FIG.E-1. OPTICAL RAY TRACE DIAGRAM

**BLANK PAGE**

```

C      SLIT FUNCTION ESTIMATE MK 2
C      ARCSIN FUNCTION INCLUDED
C      F1, F2, S TO BE IN CONSISTENT UNITS
C      INPUT ANGLES IN DEGREES
      ASINF(X)=1.5707963-SQRTF(1.0-X)*((1.5707288-
X      0.2121144*X+0.0742610*X*X-0.0187293*X*X*X)
1 READ 99, F1, F2
  READ 99,5
  READ 98, ALPC, ALPF, SIGMA
  READ 98, X1
  READ 97, REFC, REFF, WAVEL
  I=0
C      DEGREE TO RADIAN CONVERSION
      ALPC = ALPC* 1.745329E-02
      ALPF = ALPF* 1.745329E-02
      SIGMA = SIGMA* 1.745329E-02
      X1 = X1* 1.745329E-02
      X = X1
3 IF (1.5707963 - X) 7,4,4
4 SINZ = SIN(X)/REFC
  Z = ASINF(SINZ)
  GO TO 10
7 X= X-1.5707963
  SINZ = COS(X)/REFC
  Z = ASINF(SINZ)
  X=X+ 1.5707963
10 ETA = ALPC - Z
  IF (1.5707963 - ETA) 15, 12, 12
12 SINSE = (REFC*SIN(ETA))/REFF
  SE = ASINF(SINSE)
  GO TO 18
15 ETA = ETA - 1.5707963
16 SINSE = (REFC*COS(ETA))/REFF
17 SE = ASINF(SINSE)
  ETA = ETA + 1.5707963
18 EPS = ALPF - SE
  IF (1.5707963-EPS) 23,20,20
20 SINDL = (REFF * SIN(EPS))/REFC
  DELTA = ASINF(SINDL)
  GO TO 26
23 EPS = EPS - 1.5707963
  SINDL = (REFF*COS(EPS))/REFC
  DELTA = ASINF(SINDL)
  EPS = EPS + 1.5707963
26 GAMMA = ALPC - DELTA
  IF (1.5707963 - GAMMA) 31,28,28
28 SINB = REFC * SIN(GAMMA)
  BETA = ASINF(SINB)
  GO TO 33
31 GAMMA = GAMMA - 1.5707963
  SINB = REFC*COS(GAMMA)
  BETA = ASINF(SINB)
  GAMMA = GAMMA + 1.5707963
33 IF (I-1) 34,39,39
34 I=I+1
  BETA1 = BETA
  DELT1 = DELTA
  EPS1 = EPS
  SE1 = SE
  ETA1 = ETA
  Z1 = Z

```

```

X1 = X
THET1 = ATANF (S/(2.0*F1))
X2 = X1 - THET1
X = X2
GO TO 3
39 BETA2 = BETA
DELT2 = DELTA
EPS2 = EPS
SE2 = SE
ETA2 = ETA
Z2 = Z
X2 = X
PSI = SIGMA + DELTA1 - 1.5707963
THET2 = BETA2 - DELTA1
PHI = PSI + THET2
IF (PSI - 0.0) 43,46,46
43 PSI = -PSI
DISP = -(F2*SINF(PHI))/COSF(PHI)
PSI=-PSI
GO TO 51
46 IF (1.5707963 - PSI) 49,47,47
47 DISP = (F2*SINF (PSI))/COSF(PHI)
GO TO 51
49 PSI = PSI - 1.5707963
DISP = -(F2 * COSF(PHI))/SINF(PHI)
PSI = PSI + 1.5707963
51 IF (PHI - 0.0) 52,55,55
52 PHI = -PHI
DISPL = -(F2*SINF(PHI))/COSF(PHI)
PHI=-PHI
GO TO 60
55 IF (1.5707963 - PHI) 58,56,56
56 DISPL = (F2*SINF(PHI))/COSF(PHI)
GO TO 60
58 PHI = PHI - 1.5707963
DISPL = -(F2*COSF(PHI))/SINF(PHI)
PHI = PHI + 1.5707963
60 SLIT = DISPL - DISP
C
RADIANT TO DEGREE CONVERSION
R = 57.295788
ALPC = ALPC* R
ALPF = ALPF* R
SIGMA = SIGMA* R
X1 = X1*R
PUNCH 99, F1, F2
PUNCH 98, ALPC, ALPF, SIGMA
PUNCH 97, REFC, REFF
PUNCH 96
PUNCH 99, S, X1, WAVEL, SLIT
PUNCH 96
IF (SENSE SWITCH 1) 63, 1
63 BETA1 = BETA1*R
DELT1 = DELT1*R
EPS1 = EPS1*R
SE1 = SE1*R
ETA1 = ETA1*R
Z1 = Z1*R
BETA2 = BETA2*R
DELT2 = DELT2*R
EPS2 = EPS2*R
SE2 = SE2*R

```

```

ETA2 = ETA2*R
Z2 = Z2*R
X2 = X2*R
PSI = PSI*R
PHI = PHI*R
PUNCH 98, BETA1, BETA2
PUNCH 98, DELT1, DELT2
PUNCH 98, EPS1, EPS2
PUNCH 98, SE1, SE2
PUNCH 98, ETA1, ETA2
PUNCH 98, Z1, Z2
PUNCH 98, X1, X2
PUNCH 98, PSI, PHI
PUNCH 99, DISP, DISPL
PUNCH 96
PUNCH 95, WAVEL, DISP, SLIT
GO TO 1
99 FORMAT (4F9.3)
98 FORMAT (3F7.2)
97 FORMAT (2F8.5, F9.3)
96 FORMAT (/)
95 FORMAT (3F10.3)
END

```

```

C      LEAST SQUARE FITTING OF SLIT FUNCTION MK2
C      INPUT DATA FROM SLIT FUNCTION ESTIMATE MK2
      DIMENSION WAVEL(9), DISP(9), SLIT(9), FRQ(9), A(5)
1 READ 98, M
  DO 2 I=1,9
    READ 99, WAVEL(I), DISP(I), SLIT(I)
2 FRQ(I)=1.0/WAVEL(I)
  CALL LSQF(DISP, FRQ, M, 9, A)
4 DO 20 I=1,9
  FQY=A(1)
  MM=M+1
  DO 5 J=2, MM
5 FQY = FQY + A(J)*DISP(I)**(J-1)
  WL=1.0/FQY
  DIF=WL-WAVEL(I)
  XPL = DISP(I) + SLIT(I)
  FPL=A(1)
  DO 10 J=2,MM
10 FPL=FPL+A(J)*XPL**(J-1)
  WPL=1.0/FPL
  DELW=WPL-WL
  PUNCH 98, I
  PUNCH 99, SLIT(I)
  PUNCH 99, WL, WAVEL(I), DIF
20 PUNCH 99, WPL, DELW
  GO TO 1
99 FORMAT (3F10.3)
98 FORMAT (I4)
  END

```

```

SUBROUTINE LSQF (X,Y,M,N,A)
DIMENSION X(9), Y(9), B(9), C(5), A(5), U(5,5), V(5)
K=2*M+1
DO 1 L=1,K
  B(L)=0.0
  DO 1 I=1,N
1  B(L)=B(L)+X(I)**(L-1)
  I1=M+1
  DO 2 L=1,M1
    C(L)=0.0
    DO 2 I=1,N
2  C(L)=C(L)+Y(I)*X(I)**(L-1)
    DO 3 I=1,M1
      DO 3 J=1,M1
        K=I+J-1
3  U(I,J)=B(K)
    DO 4 I=1,M
      I1=I+1
      DO 4 J=I1,M1
        V(J)=U(J,I)/U(I,I)
        C(J)=C(J)-V(J)*C(I)
      DO 4 K=I1,M1
4  U(J,K)=U(J,K)-V(J)*U(I,K)
      A(M1)=C(M1)/U(M1,M1)
    DO 5 I=1,M
      K=M-I+1
      Q=0.0
      DO 6 J=K,M
6  Q=Q+A(J+1)*U(K,J+1)
5  A(K)=(C(K)-Q)/U(K,K)
  RETURN
END

```



**BLANK PAGE**

## APPENDIX F

## Integrated Lorentzian Profile Computer Programs

## (a) Single Component Profile

The computer program employed to calculate an integrated Lorentzian profile for an isolated spectral line, described by eqs (2-12) and (2-13) is given below. Input terms defined in the program are identified as follows:

    HFWIT: total halfwidth,  $\delta$

    WAVEL: wavelength of spectral line,  $\lambda_0$

    DELWV: increment in wavelength

    SLITW: spectrograph entrance slit,  $\Delta/2$

All wavelengths are in angstrom units.

The quantities HFWIT and SLITW are first converted to wavenumber equivalents, DEFRQ and DSLIT. The resonance halfwidth of the spectral line HFBRT, is then calculated in accord with eq (2-13), and converted to angstrom units as BREAT. The line profile at selected wavelength increments is then computed. DELAM(1) and DELNU(1) are the wavelength and wavenumber steps measured from the spectral line center wavelength WAVEL, at which the intensities RELIN(1) are calculated. These intensity values are normalized to the peak value at the line center by division with the quantity CONST. The negative wavelength portion of the line profile is first obtained, represented by the variables DELAM(1) and RELIN(1) in the program output. The positive wavelength portion of the line profile is then similarly calculated, again designated by the same variables DELAM(1) and RELIN(1) in the program output.

**BLANK PAGE**

```

C      INTEGRATED LORENTZIAN PROFILE MK4
C      SINGLE COMPONENT PROFILE
      DIMENSION DELAM (200), DELNU (200), RELIN (200)
      EQUIVALENCE (DELNU, RELIN)
1  READ 99, HFW, I
      READ 99, WAVEL
      READ 99, DELWV
      READ 99, SLITW
      READ 96, LTERM
      WAVE = WAVEL + 0.5*HFWIT
      DEFRQ = ( 1.0 / WAVE ) - ( 1.0 / WAVEL )
      WLENT = WAVEL + SLITW
      DSLIT = ( 1.0 / WLENT ) - ( 1.0 / WAVEL )
      HFBRT=(DEFRQ*DEFRQ) - (DSLIT*DSLIT )
      HFBRT = SORTF ( HFBRT )
      RECIP = HFBRT + 1.0 / WAVEL
      BREAT = WAVEL - ( 1.0 / RECIP)
      PUNCH 99, WAVEL, HFWIT
      PUNCH 97
      PUNCH 99, SLITW, BREAT
      PUNCH 97
      CONST=2.0*ATANF(DSLIT/HFBRT)
      STORE = 0.0
      DO 27 I = 1, LTERM
      DELAM (I) = STORE-DELWV
      STORE = DELAM(I)
      DELAM(I) = DELAM(I) + WAVEL
      DELNU(I) = (1.0/DELAM(I))-(1.0/WAVEL)
      IF (DELNU(I) -DSLIT) 22, 22, 24
22  RELIN(I)=ATANF((DELNU(I)+DSLIT)/HFBRT)
      X + ATANF ((DSLIT - DELNU(I))/HFBRT)
      GO TO 25
24  RELIN(I) = ATANF ((DELNU(I)+DSLIT)/HFBRT)
      X -ATANF ((DELNU(I) -DSLIT)/HFBRT)
25  RELIN(I) = RELIN(I)/CONST
      DELAM(I) = DELAM(I) - WAVEL
27  PUNCH 98, DELAM(I), RELIN(I)
      PUNCH 97
      STORE = 0.0
      DO 40 I=1, LTERM
      DELAM(I) = STORE + DELWV
      STORE = DELAM(I)
      DELAM(I) = DELAM (I) + WAVEL
      DELNU(I) = (1.0/DELAM(I))-(1.0/WAVEL)
      DELNU(I) = -DELNU(I)
      IF (DELNU(I)-DSLIT) 35,35,37
35  RELIN(I)=ATANF ((DELNU(I)+DSLIT)/HFBRT)
      X +ATANF ((DSLIT-DELNU(I))/HFBRT)
      GO TO 38
37  RELIN(I)=ATANF((DELNU(I)+DSLIT)/HFBRT)
      X -ATANF ((DELNU(I)-DSLIT)/HFBRT)
38  RELIN(I) = RELIN(I)/CONST
      DELAM(I) = DELAM(I) -WAVEL
40  PUNCH 98, DELAM(I), RELIN(I)
      PUNCH 97
      GO TO 1
99  FORMAT ( 2F9.3 )
98  FORMAT ( F9.3, E20.8 )
97  FORMAT (/)
96  FORMAT ( 15 )
      END

```

### (b) Multicomponent Profile

A listing of the computer program used in the calculation of a multicomponent integrated Lorentzian line profile described by eq (2-11) is given below. The following input variables are identified as:

SLIT: spectrograph entrance slit,  $\Delta/2$   
DELW: wavelength increment  
WAVE(J): center wavelength of Jth line,  $\lambda_j$   
A(J): resonance halfwidth of Jth line,  $A_j/2$   
BI(J): relative intensity of Jth line,  $J(v_j)$

All wavelengths are in angstrom units.

The variables SLIT, WAVE(J), and A(J) are first converted to wavenumber equivalents as DSLIT, FREQ(J), and BRET(J) respectively. Individual contributions to the total line profile from each broadened spectral component are then computed at specified wavelength intervals about the center wavelength of the principal spectral line WAVE(1). Negative and positive wavelength increments are called DELAM(1) and DELW(1) respectively. No distinction is made for the corresponding wavenumber steps DELNU(1). The spectral component intensities RELIN(J) and SOURC(J) are added to give the total line intensity SUM(1) and ADD(1) about the center wavelength WAVE(1). These results are normalized to the maximum total intensity value PHIZ0. The normalized line intensities SUM(1) and ADD at wavelength intervals DELAM(1) and DELW(1) comprise the program output.

```

C      INTEGRATED LORENTZIAN PROFILE MK7
C      MULTICOMPONENT PROFILE
C      PRINCIPAL COMPONENT CALLED WAVE(1)
      DIMENSION WAVE(5), A(5), BI(5), FREQ(5), BRET(5), DELAM(60),
      X DELNU(60), RELIN(5), SUM(60), DELWV(60), SOURC(5), ADD(60)
      EQUIVALENCE ( RELIN, SOURC )
1 READ 99, SLIT
  READ 99, DELW
  READ 96, LTERM
  READ 96, N
  DO 3 J= 1,N
    READ 99, WAVE(J)
    READ 99, A(J)
    READ 99, BI(J)
3 PUNCH 99, WAVE(J), A(J), BI(J)
  PUNCH 95
  PUNCH 99, SLIT
  PUNCH 95
  SLITW = WAVE(1) - SLIT
  DSLIT = ( 1.0/SLITW ) - ( 1.0/WAVE(1) )
  DO 6 J=1, N
    FREQ(J) = 1.0/WAVE(J)
6 BRET(J) = 1.0/(WAVE(J) - A(J)) - FREQ(J)
  STORE = DELW
  SUMA = 0.0
  LL = LTERM + 1
  DO 20 I = 1, LL
    DELAM(I) = STORE - DELW
    STORE = DELAM(I)
    DELAM(I) = DELAM(I) + WAVE(1)
  DO 18 J= 1, N
    DELNU(I) = ( 1.0/DELAM(I) ) - FREQ(J)
    IF( DELNU(I) - DSLIT ) 11, 11, 12
11 RELIN(J) = ATANF( (DELNU(I) + DSLIT)/ BRET(J) ) +
  X ATANF( (DSLIT - DELNU(I)) / BRET(J) )
    GO TO 13
12 RELIN(J) = ATANF( (DELNU(I) + DSLIT)/ BRET(J) ) -
  X ATANF( (DELNU(I) - DSLIT) / BRET(J) )
13 RELIN(J) = BRET(J)* BI(J)* RELIN(J)
    BLANK = 0.0
    SUM(I) = SUMA + RELIN(J)
18 SUMA = SUM(I)
20 SUMA = 0.0
  STORE = 0.0
  SUMB = 0.0
  DO 35 I= 1, LTERM
    DELWV(I) = STORE + DELW
    STORE = DELWV(I)
    DELWV(I) = DELWV(I) + WAVE(1)
  DO 34 J=1,N
    DELNU(I) = ( 1.0/DELWV(I) ) - FREQ(J)
    IF( DELNU(I) - DSLIT ) 27, 27, 26
27 SOURC(J) = ATANF( (DELNU(I) + DSLIT)/ BRET(J) ) +
  X ATANF( (DSLIT - DELNU(I)) / BRET(J) )
    GO TO 29
28 SOURC(J) = ATANF( (DELNU(I) + DSLIT)/ BRET(J) ) -
  X ATANF( (DELNU(I) - DSLIT)/ BRET(J) )
29 SOURC(J) = BRET(J)* BI(J)* SOURC(J)
    ADD(I) = SUMB + SOURC(J)
34 SUMB = ADD(I)
35 SUMB = 0.0

```

```

PUNCH 95
AMAX = SUM(1)
BIGD = DELAM(1)
DO 39 I=2, LL
IF( AMAX - SUM(1) ) 38,39,39
38 AMAX = SUM(1)
BIGD = DELAM(1)
39 CONTINUE
BMAX = ADD(1)
BIGL = DELWV(1)
DO 43 I = 2, LTERM
IF ( BMAX - ADD(1) ) 42,43,43
42 BMAX = ADD(1)
BIGL = DELWV(1)
43 CONTINUE
IF( AMAX - BMAX ) 45,46,46
45 PHIZO = BMAX
WVZO = BIGL - WAVE(1)
GO TO 47
46 PHIZO = AMAX
WVZO = BIGD - WAVE(1)
47 PUNCH 99, BLANK, BLANK, WVZO, PHIZO
PUNCH 95
DO 49 I =1,LL
SUM(1) = SUM(1) / PHIZO
DELAM(1) = DELAM(1) - WAVE(1)
49 PUNCH 99, BLANK, BLANK, DELAM(1), SUM(1)
PUNCH 95
DO 51 I =1, LTERM
ADD(1) = ADD(1)/PHIZO
DELWV(1) = DELWV(1) - WAVE(1)
51 PUNCH 99, BLANK, BLANK, DELWV(1), ADD(1)
PUNCH 95
GO TO 1
99 FORMAT ( 3F9.3, E20.8 )
96 FORMAT ( 15)
95 FORMAT (/)
END

```

## APPENDIX G

## Spectral Line Shift Calculations

## (a) Holtsmark's theory

The computer program used to calculate the linear Stark shift due to a given plasma ion density is listed below. The following quantities used in the program are related to terms in eqs (2-23), (2-28), and (2-29) as:

DION    ion density,  $N_i$   
 CLIN    linear Stark coefficient,  $C_i$   
 WAVE    spectral line wavelength,  $\lambda_0$   
 FZERO   average intermolecular field,  $F_0$   
 DELTA   Stark component shift,  $(\Delta\nu)_i$

DION is in units of  $10^{18} \text{ cm}^{-3}$ , CLIN in  $\text{cm}^{-1}/\text{esu}^*$ , and WAVE in angstrom units. The program output FZERO is in kv/cm and DELTA is given in angstrom units.

Values of the net line shift  $\delta_s$ , for the CuI 4531 line computed for a range of ion densities are shown in Table G-1. The intermolecular field strength  $F_0$ , and the individual p- and n- component shifts are also included. The variation of the CuI 4531 net line shift with ion density for a linear Stark effect is illustrated in Fig. 27.

The computer program used to calculate the quadratic Stark shift from Holtsmark's theory is given below. The quantity CQUAD is the quadratic Stark coefficient appearing as  $K_i$  in eq (2-34). All other terms

---

\*The electrostatic unit of field strength (esu) is statvolt/cm.



are defined as in the above linear Stark shift calculation. CQUAD is in units of  $\text{cm}^{-1}/(\text{esu})^2$ . Evaluations of the net line shift for the CuI 4531 line are given in Table G-11. The variation of the net shift with ion density for a quadratic Stark effect is also illustrated in Fig. 27.

#### (b) Folded distribution

Spectral line shifts resulting from the combined effect of nearby plasma ions and electrons are obtained from an evaluation of the folded distribution, eq (2-30), where the electron-broadened line profile is given by eq (2-31). Briefly what is done is to determine the electron-ion broadened line profile for a given charged particle density. The wavelength position at which the resultant profile has a maximum value yields the spectral line shift corresponding to the given charged particle density.

In terms of the dimensionless ratio  $\beta$ , the electron-ion profile for a Stark component of a spectral transition that exhibits a linear Stark effect is given by

$$J(\nu) = \text{const} \times \int_0^{\infty} \frac{W(\beta) d\beta}{(\omega - C_J F_0 \beta)^2 + \gamma_J^2} \quad (\text{G-1})$$

where

$$\beta = F/F_0$$

$$\omega = \nu - \nu_0$$

$W(\beta)$  is the Holtsmark distribution function,  $\nu_0$  the nominal wavenumber of the spectral line,  $C_J$  a linear Stark coefficient,  $F_0$  the average intermolecular field given by eq (2-23), and  $\gamma_J$  the halfwidth of the electron-broadened component profile.

Let  $W(\beta)$  be represented by a linear function of  $\beta$  in the interval  $A_K \leq \beta \leq A_{K+1}$ , i.e.

$$W(\beta) = a_K + b_K \beta \quad (G-2)$$

The values of the coefficients  $a_K$ ,  $b_K$  are calculated for each interval in the following simple manner. At the point  $A_K$  one has

$$W(A_K) = a_K + b_K A_K$$

and similarly, at the point  $A_{K+1}$

$$W(A_{K+1}) = a_K + b_K A_{K+1}$$

where  $W(A_K)$ ,  $W(A_{K+1})$  are the values of the Holtsmark distribution function at  $A_K$ ,  $A_{K+1}$  respectively. Solving these for the coefficients  $a_K$ ,  $b_K$  one has:

$$a_K = \frac{A_{K+1} W(A_K) - A_K W(A_{K+1})}{A_{K+1} - A_K} \quad (G-3)$$

$$b_K = \frac{W(A_{K+1}) - W(A_K)}{A_{K+1} - A_K} \quad (G-4)$$

Values for  $A_K$  and  $W(A_K)$  are obtained from a numerical tabulation of the Holtsmark distribution function, (Greenstein, 1960).

With this linear approximation for  $W(\beta)$ , eq (G-1) can be written as

$$J(v) \approx \sum_K \int_{A_K}^{A_{K+1}} \frac{(a_K + b_K \beta) d\beta}{(v - C_J F_0 \beta)^2 + \gamma_J^2} \quad (G-5)$$

where the summation is performed for all tabulated values of  $\beta$ . The constant in eq (G-1) has been set to unity since the resultant profile is to be normalized to its maximum value.

Define the quantities  $K_K$ ,  $L_K$  as

$$K_K = a_K \int_{A_K}^{A_{K+1}} \frac{d\beta}{(\omega - c_j F_o \beta)^2 + \gamma_j^2}$$

$$L_K = b_K \int_{A_K}^{A_{K+1}} \frac{\beta d\beta}{(\omega - c_j F_o \beta)^2 + \gamma_j^2}$$

Thus

$$J(\nu) = \sum_K (K_K + L_K) \quad (G-6)$$

Upon integration, one has

$$K_K = \left\{ \frac{a_K}{c_j F_o \gamma_j} \tan^{-1} \frac{x}{\gamma_j} \right\}_{A_K}^{A_{K+1}}$$

$$L_K = \left\{ \frac{b_K}{2(c_j F_o)^2} \ln(x^2 + \gamma_j^2) + \frac{b_K \omega}{(c_j F_o)^2 \gamma_j} \tan^{-1} \frac{x}{\gamma_j} \right\}_{A_K}^{A_{K+1}}$$

where

$$x = c_j F_o \beta - \omega$$

Thus

$$\begin{aligned} \gamma_j (c_j F_o)^2 (K_K + L_K) = & \left\{ (a_K c_j F_o + b_K \omega) \tan^{-1} \frac{x}{\gamma_j} \right. \\ & \left. + \frac{b_K \gamma_j}{2} \ln(x^2 + \gamma_j^2) \right\}_{A_K}^{A_{K+1}} \end{aligned} \quad (G-7)$$

The resultant spectral line profile is found from eqs (G-6) and (G-7).

Numerical evaluations of these equations leading to the determination of the line shift for a given electron-ion density were performed with the computer program listed below. The input quantities are related to terms in the above equations as follows.

B(I) dimensionless field strength,  $A_K$   
W(I) Holtsmark distribution function,  $W(A_K)$   
DION ion density,  $N_i$   
CLIN linear Stark coefficient,  $C_j$   
GAMMA electron-broadened halfwidth,  $\gamma_j^*$   
WAVE spectral line wavelength,  $\lambda_0$   
DELAM wavelength increment

The profile calculations were initiated at an arbitrary wavelength  $D$ , from the nominal spectral line center,  $\lambda_0$ . DION is in units of  $10^{18} \text{ cm}^{-3}$ , CLIN in  $\text{cm}^{-1}/\text{esu}$ , GAMMA in  $\text{cm}^{-1}$ , and WAVE in angstrom units.

The average intermolecular electric field FZERO, is determined in accord with eq (2-23) and appears as an output in units of kv/cm. The variable DEL(J) represents the wavelength with respect to the nominal line center,  $\lambda - \lambda_0$ , at which the profile is to be calculated. DNU(J) is the related wavenumber difference,  $\omega$ . At a particular wavelength DEL(J), the coefficients in the linear approximation equation for the Holtsmark distribution function are computed in accord with eqs (G-3) and (G-4).  $a_K$  is represented in the program by the term A, and  $b_K$  by the term BB.

---

\*Estimates for  $\gamma_j$  are discussed below in part (c) of this appendix.

Values of the quantities  $K_K + L_K$  given by eq (G-7) are then obtained. The program first calculates the sum of the individual contributions to the quantity  $K_K + L_K$  at the upper limit,  $A_{K+1}$ . XPLUS represents the value of the variable  $X$  at the upper limit of each individual integration,  $A_{K+1}$ . The resulting value of this summation is ADD(J). Similarly the sum of the individual contributions to  $K_K + L_K$  at the lower limit  $A_K$  is obtained next. XMINS is the value of the variable  $X$  at the lower limit of each integration,  $A_K$ . The value of this summation is called SUM(J). The quantity  $ADD(J) - SUM(J)$  then determines  $J(v)$  in accord with eq (G-6) at the wavelength DEL(J). This procedure is repeated at each wavelength step to describe the line profile ADD(J) at the wavelength DEL(J) for each Stark component.

The remainder of the program is directed towards the determination of the wavelength at which the line profile has a peak value. The quantities ADD(J) are first normalized to their maximum value BMAX, and presented as output along with the associated wavelengths DEL(J). In order to improve the determination of the peak value of the line profile a second-order least squares fit in the vicinity of the above-calculated maximum value of the computed profile is then made. Two points on either side of this computed maximum are used in the fitting calculation. The subroutine POLYFT, previously listed in Appendix C is used to obtain the least squares fit. The wavelength at which the fitted profile is a maximum is called XMAX. It represents the shift in a Stark split component of a spectral line under the combined influence of electrons and ions in the vicinity of an emitting atom.

Values of the net line shift  $\delta_s$ , for the CuI 4531 line obtained

from the folded distribution calculation for several values of ion density are shown in Table G-III. Shifts of the individual p- and n- components are also included. The variation of the CuI 4531 net wavelength shift with ion density for a linear Stark effect is illustrated in Fig. 27.

(c) Electron-broadened halfwidth calculations

Kolb (1956) has derived the following expression for the electron-broadened line halfwidth  $\gamma_j$ , for a spectral line that exhibits a linear Stark effect.

$$\gamma_j = \frac{16N_e}{3\bar{v}} (eC_j)^2 (2.36 - 2\ln \delta_j) \quad (G-8)$$

where  $N_e$  is the electron density,  $C_j$  is a linear Stark coefficient,  $e$  the electronic charge and

$$\bar{v} = (3kT/m)^{1/2}$$

$$\delta_j = 2eC_j/\rho\bar{v}$$

$$\rho = (kT/8\pi m_e^2 N_e)^{1/2}$$

$m$  represents the mass of an electron and  $T$  the temperature.

For the p- and n- Stark components of the CuI 4531 line one has numerically

$$\gamma_p = 1.424(1 - 0.847 \ln \delta_p) n_e / (T)^{1/2}$$

where

$$\delta_p = 72.7(n_e)^{1/2}/T$$

and

$$\gamma_n = 0.801(1 - 0.847 \ln \delta_n) n_e / (T)^{1/2}$$

where

$$\delta_n = 54.0(n_e)^{1/2}/T$$

$n_e$  is the electron density in units of  $10^{18} \text{ cm}^{-3}$ , and  $\gamma_p, \gamma_n$  are the component halfwidths in wavenumber units,  $\text{cm}^{-1}$ .

A program for computing these electron-broadened line halfwidths for a given electron density and temperature is given below. The program input quantities DION and T represent the electron density value  $n_e$  and temperature T respectively. The halfwidth value  $\gamma_p$  is called GAMMA, and  $\gamma_n$  is called GAMMB. Table G-IV shows the calculated  $\gamma$ -values for several choices of electron density and temperature.

These values for  $\gamma_j$  were employed to carry out the folded distribution line shift calculations. Specifically the electron-broadened halfwidth at a temperature of  $5000^\circ\text{K}$  for a given charged particle density was used. To ascertain that the calculated line shifts were relatively insensitive to the value of temperature chosen over a reasonable temperature range, comparative shifts were calculated for a fixed particle density and different temperatures. The numerical results given in Table G-V show that for the temperature values considered the variations in line shift are insignificant.

Table G-1

CuI 4531 Linear Stark Shift (Holtsmark Theory)

Ion Density ( $\text{cm}^{-3}$ )	$F_o$ (kv/cm)	Component Shift		$\delta_s$ (A)
		p (A)	n (A)	
$5.0 \cdot 10^{16}$	51	0.07	0.05	0.06
$1.0 \cdot 10^{17}$	81	0.11	0.08	0.10
$5.0 \cdot 10^{17}$	227	0.32	0.24	0.28
$1.0 \cdot 10^{18}$	376	0.51	0.38	0.45
$5.0 \cdot 10^{18}$	1100	1.50	1.12	1.31
$1.0 \cdot 10^{19}$	1745	2.38	1.78	2.08
$5.0 \cdot 10^{19}$	5103	6.96	5.22	6.09



Table G-11

Cul 4531 Quadratic Stark Shift (Holtsmark Theory)

Ion Density ( $\text{cm}^{-3}$ )	$F_0$ (kv/cm)	Component Shift		$\delta_s$ (A)
		p (A)	n (A)	
$1.0 \cdot 10^{17}$	. 81	0.30	0.23	0.27
$5.0 \cdot 10^{17}$	227	2.61	1.96	2.28
$1.0 \cdot 10^{18}$	376	6.57	4.93	5.75
$5.0 \cdot 10^{18}$	1100	56.17	42.13	49.15

Table G-III

CuI 4531 Linear Stark Shift (Folded Distribution)

Ion Density (cm <sup>-3</sup> )	Component	Shift	$\delta_s$ (A)
	p (A)	n (A)	
1.0 10 <sup>18</sup>	0.58	0.44	0.51
5.0 10 <sup>18</sup>	1.64	1.23	1.44
1.0 10 <sup>19</sup>	2.61	1.95	2.28

Table G-IV

## Electron-Halfwidth Values for CuI 4531 Stark Components

Electron Density ( $\text{cm}^{-3}$ )	Temperature ( $^{\circ}\text{K}$ )	Halfwidth	
		$\gamma_p$ ( $\text{cm}^{-1}$ )	$\gamma_n$ ( $\text{cm}^{-1}$ )
$1.0 \times 10^{19}$	1000	0.145	0.088
	5000	0.092	0.055
	10000	0.074	0.043
$5.0 \times 10^{18}$	1000	0.572	0.353
	5000	0.393	0.235
	10000	0.320	0.190
$1.0 \times 10^{19}$	1000	1.011	0.632
	5000	0.727	0.437
	10000	0.597	0.356

Table G-V

Variation of Line Shift with Temperature\*

Temperature $T(^{\circ}\text{K})$	Line Shift $\delta_s, (\text{\AA})$
1000	1.447
5000	1.439
10000	1.436

\* An electron density of  $5 \times 10^{18} \text{ cm}^{-3}$  was assumed.

**BLANK PAGE**

```

C LINE SHIFT CALCULATION MK3
C HOLTSMARK THEORY
C LINEAR STARK EFFECT
  I READ 98, DION
    READ 96, CLIN
    READ 98, WAVE
    PUNCH 98, DION
    PUNCH 98, WAVE
    PUNCH 96, CLIN
    PUNCH 99
    WAVE = WAVE*1.0E-08
    FZERO = 7.1333 + 0.6667*LOGF(DION)
    FZERO = 0.3*EXP(FZERO)
    PUNCH 96, FZERO
    DELTA = 1.5*CLIN*FZERO
    DELTA = -DELTA*WAVE*WAVE
    DELTA = DELTA*1.0E+08
    PUNCH 98, DELTA
    PUNCH 99
    GO TO 1
99 FORMAT (/)
98 FORMAT ( F11.4 )
96 FORMAT ( E15.8 )
END

```

C LINE SHIFT CALCULATION MR4

C HOLTSMARK THEORY

C QUADRATIC STARK EFFECT

```
1 READ 98, DION
  RE D 96, CQUAD
  READ 98, WAVE
  PUNCH 98, DION
  PUNCH 98, WAVE
  PUNCH 96, CQUAD
  PUNCH 99
  WAVE = WAVE*1.0E-08
  FZERO=7.1333 + 0.6667*LOGF(DION)
  FZERO = 0.3*EXP(-FZERO)
  PUNCH 96, FZERO
  DELTA= 2.25*FZERO*FZERO
  DELTA = CQUAD*DELTA
  DELTA = - DELTA*WAVE*WAVE
  DELTA = DELTA*1.0E+08
  PUNCH 98, DELTA
  PUNCH 99
  GO TO 1
99 FORMAT (/)
98 FORMAT ( F11.4 )
96 FORMAT ( E15.8 )
END
```

C FOLDED DISTRIBUTION

C POLYFT SUBROUTINE USED

```
      DIMENSION B(50),W(50),DNU(65),DEL(65),ADD(65),SUM(65)
      DIMENSION X(40), Y(40), COEFF(5)
      COMMON X, Y, COEFF
      READ 98, ZERO,ZERO,N
      DO 1 I=1,N
1 READ 98, B(I),W(I)
2 READ 98, DION
  READ 96, CLIN
  READ 96, GAMMA
  READ 98, WAVE,DELAM,LTERM
  READ 98, D
  PUNCH 98, DION
  PUNCH 98, WAVE
  PUNCH 96, CLIN, GAMMA
  PUNCH 99
  FZERO=7.1333+0.6667*LOGF(DION)
  FZERO = 0.3*EXPF(FZERO)
  PUNCH 96, FZERO
  PUNCH 99
  WAVE=WAVE*1.0E-08
  DELAM=DELAM*1.0E-08
  D = D*1.0E-08
  G2=GAMMA*GAMMA
  DO 3 J=1,LTERM
    D=D+DELAM
    DEL(J)=D*1.0E+08
    WAVEK = WAVE + D
    DNU(J)=1.0/WAVEK-1.0/WAVE
    ADD(J)=0.0
3 SUM(J) = 0.0
  DO 11 J = 1, LTERM
    NN = N-1
    DO 4 K = 1, NN
      A=(B(K+1)*W(K)-W(K+1)*B(K))/(B(K+1)-B(K))
      BB=(W(K+1)-W(K))/(B(K+1)-B(K))
      XPLUS = CLIN*FZERO*B(K+1)-DNU(J)
      AMPP=LOGF(XPLUS*XPLUS+GAMMA*GAMMA)
      AMPP=0.5*BB*GAMMA*AMPP
      QTYP=XPLUS/GAMMA
      IF(QTYP) 5, 6, 6
5 QTYP=-ATANF(-QTYP)
      GO TO 7
6 QTYP=ATANF(QTYP)
7 QTYP = QTYP*(A*CLIN*FZERO + BB*DNU(J))
      ADD(J)=ADD(J)+AMPP+QTYP
      XMIN = CLIN*FZERO*B(K)-DNU(J)
      AMPM=LOGF(XMIN*XMIN+GAMMA*GAMMA)
      AMPM=0.5*BB*GAMMA*AMPM
      QTYM=XMIN/GAMMA
      IF(QTYM) 8, 9, 9
8 QTYM=-ATANF(-QTYM)
      GO TO 10
9 QTYM=ATANF(QTYM)
10 QTYM = QTYM*(A*CLIN*FZERO + BB*DNU(J))
  4 SUM(J) = SUM(J)+AMPM+QTYM
11 ADD(J)=ADD(J)-SUM(J)
    BMAX=ADD(1)
    WMAX=DEL(1)
```



```

      LMAX = 1
      DO 12 J=2,LTERM
        IF (ADD(J)-BMAX) 12,31,31
31    BMAX=ADD(J)
        WMAX=DEL(J)
        LMAX = J
12    CONTINUE
      PUNCH 95, WMAX,BMAX
      BMAX=1.0/BMAX
      DO 32 J = 1, LTERM
        ADD(J)=ADD(J)*BMAX
32    PUNCH 98, DEL(J),ADD(J)
      PUNCH 99
      DO 30 K = 1, 5
        LMIN = LMAX - J + K
        Y(K) = ADD(LMIN)
30    X(K) = DEL(LMIN)
      CALL POLYFT ( X, Y, 2, 5, COEFF )
      XMAX = -0.5*COEFF(2)/COEFF(3)
      PUNCH 95, XMAX
      PUNCH 99
      GO TO 2
99    FORMAT (/)
98    FORMAT (F11.4,F11.5,15)
96    FORMAT (2E15.8)
95    FORMAT ( F11.4, E15.8 )
      END

```

C ELECTRON BROADENING HALFWIDTH ESTIMATES

```
1 READ 99, DION
  READ 99, T
  A = SQRTF(DION)
  B = 1.0/SQRTF(T)
  DELA = 72.7*A
  DELA = DELA/T
  GAMMA = 1.424*(1.0-0.847*LOGF(DELA))
  GAMMA = (GAMMA*DION)*B
  DELB = 54.0*A
  DELB = DELB/T
  GAMMB = 0.801*(1.0-0.847*LOGF(DELB))
  GAMMB = (GAMMB*DION)*B
  PUNCH 99, DION, T, GAMMA, GAMMB
  GO TO 1
99 FORMAT ( 2F11.4, 2E15.8 )
END
```

**BLANK PAGE**

## APPENDIX H

## Densitometer Slit Broadening Effects

The operation of the Baird-Atomic densitometer is schematically indicated in Fig. H-1.\* A light beam from a source lamp is chopped by means of a rotating shield. The chopped beam is first transmitted through the film under study, and alternately through a mechanically driven aperture, i.e. the reference beam path. After passage through the film the resultant beam is focused on the scanning slit and photomultiplier for comparison with the reference beam. Differences in light intensity actuate a servo amplifier and motor which in turn drives the adjustable aperture in the reference beam path. The servo system is at a null balance when both beam intensities are equal.

Let  $J_0$  be the source lamp intensity and  $J_0^i$  the light intensity of the reference beam after passage through the adjustable aperture.

Thus

$$J_0^i = J_0 10^{-D} \quad (H-1)$$

where  $D$  is the density value determined by the opening of the adjustable aperture. If  $D(x,y)$  represents the density corresponding to a given position  $x,y$ , on the film, then the intensity of the chopped beam after passage through the film is given by

$$J = \frac{1}{WL} \int_{-L/2}^{L/2} \int_{-w/2}^{w/2} J_0 10^{-D(x,y)} dx dy \quad (H-2)$$

where  $W,L$  represent the scanning slit width and length respectively,

---

\*A full description of this instrument is given by R.O. Carpenter and J.U. White, Analytical Chemistry 25, 1473 (Oct 1953).

projected onto the film plane. The y-direction corresponds to the direction of increasing time on the film record, and the x-direction is related to a wavenumber scale from a dispersion relation. Neglecting temporal variations on the film record over the length of the slit L one has

$$J = \frac{1}{W} \int_{-W/2}^{W/2} J_0 10^{-D(x)} dx \quad (H-3)$$

The system is at null balance when

$$J = J_0^1$$

or from eqs (H-1) and (H-3)

$$\frac{1}{W} \int_{-W/2}^{W/2} 10^{-D(x)} dx = 10^{-D} \quad (H-4)$$

Conversion from linear distance on film  $x$ , to optical wavenumber  $\nu$  from a dispersion relation results in

$$\frac{1}{\bar{W}} \int_{-\bar{W}/2}^{\bar{W}/2} 10^{-D(\nu)} d\nu = 10^{-D} \quad (H-5)$$

where  $\bar{W}$  is the wavenumber equivalent of the geometrical slit width  $W$ .

Expanding  $D(\nu)$  about the center frequency  $\nu_c$  in the interval from  $-\bar{W}/2$  to  $\bar{W}/2$ , and keeping second order terms one has

$$D(\nu) \approx D(\nu_c) + \left\{ \frac{dD}{d\nu} \right\}_{\nu_c} \nu + \frac{1}{2} \left\{ \frac{d^2 D}{d\nu^2} \right\}_{\nu_c} \nu^2$$

where  $\nu$  is measured from  $\nu_c$ . Thus

$$10^{-D(\nu)} \approx 10^{-D(\nu_c)} 10^{-\alpha \nu} 10^{-\beta \nu^2}$$

where  $\alpha = \left(\frac{dD}{dv}\right)_{v_c}$

$$\beta = \frac{1}{2} \left(\frac{d^2D}{dv^2}\right)_{v_c}$$

For small  $\alpha$  and  $\beta$  the above expression becomes

$$10^{-D(v)} \approx 10^{-D(v_c)} \left\{ 1 - \alpha v + \frac{1}{2} \alpha^2 v^2 - \frac{1}{2} \beta v^2 \right\}$$

to second order terms in  $v$ . Thus from eq (H-5)

$$\frac{10^{-D(v_c)}}{\bar{v}} \int_{-\bar{v}/2}^{\bar{v}/2} \left\{ 1 - \alpha v + \frac{(\alpha^2 - \beta)}{2} v^2 \right\} dv \approx 10^{-D}$$

Performing the integration there finally results

$$D(v_c) - D \approx \log \left\{ 1 + \left(\frac{\alpha^2 - \beta}{12}\right) \bar{v}^2 \right\} \quad (H-6)$$

Thus the optical density as measured by the densitometer deviates from the true film density (at the center of the scanning slit) by the amount indicated on the right hand side of eq (H-6).

If  $\bar{\Phi}$  is the film exposure associated with the density  $D(v_c)$  and  $\Phi_m$  that associated with  $D$  then

$$\bar{\Phi}/\Phi_m \approx \left\{ 1 + \left(\frac{\alpha^2 - \beta}{12}\right) \bar{v}^2 \right\}^{1/\gamma} \quad (H-7)$$

where  $\gamma$  is the slope of the photometric calibration curve. Expanding the bracketed expression one has finally

$$(\bar{\Phi} - \Phi_m)/\Phi_m \approx (\alpha^2 - \beta) \bar{v}^2 / 12\gamma \quad (H-8)$$

The constants  $\alpha$ ,  $\beta$  are evaluated as follows. From their definition

$$\alpha = \left( \frac{dB}{dv} \right)_{v_c} = \gamma / \theta \left( \frac{d\theta}{dv} \right)_{v_c}$$

and similarly

$$\begin{aligned} 2\beta &= \left( \frac{d^2B}{dv^2} \right)_{v_c} \\ &= \gamma / \theta \left\{ \frac{d^2\theta}{dv^2} - \frac{1}{\theta} \left( \frac{d\theta}{dv} \right)^2 \right\}_{v_c} \end{aligned}$$

where  $\theta$  is given by eq (2-11) in the text. After some manipulation one finally arrives at

$$\alpha^2 - \beta = 4/A^2 \left\{ \left( \frac{c_2}{c_1} \right)^2 - \frac{c_3}{c_1} \right\} \quad (H-9)$$

where

$$c_1 = \tan^{-1} X - \tan^{-1} Z$$

$$c_2 = \frac{1}{1+X^2} - \frac{1}{1+Z^2}$$

$$c_3 = \frac{Z}{(1+Z^2)^2} - \frac{X}{(1+X^2)^2}$$

$$X = (v_c - v_o + \Delta) / A/2$$

$$Z = (v_c - v_o - \Delta) / A/2$$

and  $\gamma = 1.0$  has been assumed.

A listing of the Fortran program used to numerically evaluate errors that result from the use of a finite width scanning slit is given below. Several important quantities named in the program are related to variables in the above equations in the following manner

WAVEK Wavelength of spectral line,  $\lambda_0$   
 BREAT Resonance halfwidth,  $A/2$   
 SLIT Spectrograph entrance slit,  $\Delta/2$   
 ERROR Densitometer slit width,  $\bar{\lambda} = 1/\bar{v}$   
 DWAVE Increment in wavelength

These input quantities are all in angstrom units

The output of the program consists of:

DEL wavelength difference,  $\lambda_c - \lambda_0$   
 ERR relative exposure error,  $(\bar{I} - \bar{I}_m)/\bar{I}_m$

A sample calculation of the error due to a finite width densitometer slit has been made for a CuI 4651 profile of narrow width. At a time of 7.7  $\mu$ sec the resonance halfwidth  $A$ , for this line is 3.10A; the spectrograph entrance slit is 5.50A at this wavelength. The projected width of the scanning slit onto the film plane is about 0.013 mm and corresponds to a wavelength range of approximately 0.5A for the nominal 40A/mm dispersion at this wavelength. The calculations indicate that the maximum relative exposure error ERR is less than 0.5 percent throughout the line profile.



**BLANK PAGE**

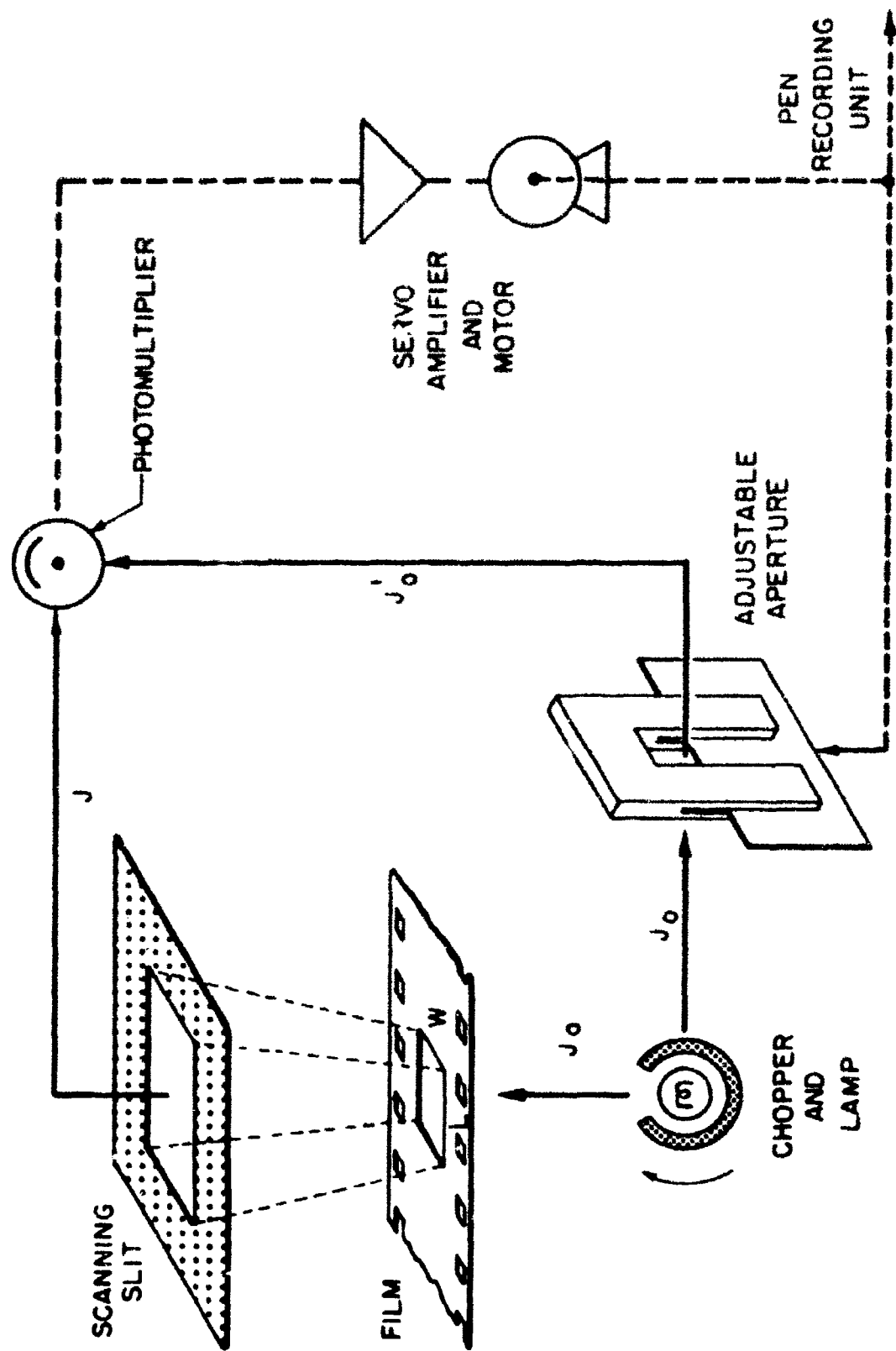


FIG.H-1. SCHEMATIC DIAGRAM OF DENSITOMETER

```

C   DENSITOMETER SLIT CORRECTION  MK2
1  READ 99, WAVEK, BREAT, SLIT, ERROR, DWAVE, N
   PUNCH 99, WAVEK, BREAT, SLIT, ERROR
   RATIO = ERROR/BREAT
   PUNCH99, RATIO
   WAVE=WAVEK+BREAT
   HFWIT=(1.0/WAVEK)-(1.0/WAVE)
   WAVE=WAVEK+SLIT
   SLIT=(1.0/WAVEK)-(1.0/WAVE)
   I=1
   AAA=0.0
2  DEL=DWAVE*AAA
   WAVE =WAVEK+DEL
   Y=(1.0/WAVEK)-(1.0/WAVE)
   X=(Y+SLIT)/HFWIT
   Z=(Y-SLIT)/HFWIT
   IF(Z)3,3,4
3  ZZ= -Z
   C1=ATANF(X)+ATANF(ZZ)
   GO TO 5
4  C1=ATANF(X)-ATANF(Z)
5  C2=(1.0/(1.0+X*X)) - (1.0/(1.0+Z*Z))
6  C3=(Z/(1.0+Z*Z))*(1.0/(1.0+Z*Z))
7  C3=C3-(X/(1.0+X*X))*(1.0/(1.0+X*X))
   BETA = (C2*C2/(C1*C1)) - C3/C1
   BETA=BETA/(BREAT*BREAT)
   ERR= 0.0833*BETA*ERROR*ERROR
   PUNCH98, DEL, ERR
   IF(1-N)8, 1,1
8  I=I+1
   AAA=AAA+1.0
   GO TO 2
99 FORMAT ( 5F9.3, 15 )
98 FORMAT ( F9.3, 2E20.8 )
END

```

## APPENDIX I

### Spectral Line Self-Absorption Calculations

Numerical estimates of the effects of self-absorption on the observed spectral lines are derived from a one-dimensional absorption model. Distortions of the line profile upon passage through a thin plane-parallel absorbing region are given by eqs (2-36), (2-38), and (2-39). The optical depth of a thin slab  $\tau_j(\nu)$  is, in cgs units

$$\tau_j(\nu) = -8.448 \cdot 10^{-3} f_{\text{abs}} \int_{r_{j-1}}^{r_j} \frac{N_a \gamma}{(\nu - \nu_j)^2 + \gamma^2} dr \quad (I-1)$$

where  $N_a$ , the number density of absorbing atoms and  $\gamma$ , the collision damping constant depend upon the radial position. The number density of absorbing atoms, i.e., of excited atoms in the lower energy level of the affected spectral transition, is related to the total number density of neutral atoms as

$$N_a/N = (g/U) \exp(-E/kT) \quad (I-2)$$

assuming local thermodynamic equilibrium in each element of the slab.  $g$  is the statistical weight of the lower energy level,  $U$  the partition function for the neutral atom,  $E$  the energy of the lower level, and  $T$  the local temperature in the slab.

The neutral atom density and temperature distributions determined from the fluid-dynamic model of a jet collision are used in the calculations (Lukasik et al, 1964). If  $N_c$  represents the

neutral atom density and  $T_c$  the temperature at the impact center,  $r_f$  the position of the front of the expanding collision-produced material sheet, and  $r$  a radial position in the sheet, then near the expanding front one has

$$N/N_c = 26.0 (1 - r/r_f)^4 \quad (1-3)$$

The temperature ratio  $T/T_c$  was expressed as a fourth-order polynomial in  $r/r_f$  (see program listing).  $N_c$  and  $r_f$  are given as functions of the time after initial impact as

$$N_c (\text{cm}^{-3}) = 35.0 \cdot 10^{20} / t^2 \quad (1-4)$$

$$r_f (\text{cm}) = 1.72 t \quad (1-5)$$

for  $t$  in  $\mu\text{sec}$ .  $T_c$  was treated as a parameter in the calculations.

Combining the above equations one finally arrives at

$$\tau_j(\nu) = - \int_{r_{j-1}}^{r_j} \alpha \beta (1 - r/r_f)^4 dr \quad (1-6)$$

where

$$\alpha = 9.095 \cdot 10^{22} g \exp(-E/kT) / Ut^2$$

$$\beta = 8.448 \cdot 10^{-3} f_{\text{abs}} \gamma \left\{ (\nu - \nu_j)^2 + \gamma^2 \right\}$$

Treating  $\alpha$  and  $\beta$  as constants over the range of integration for each absorbing slab by considering a small slab thickness one has

$$\tau_j(\nu) \approx - (\alpha \beta / 5 r_f^4) (r_f - r)^5 \Big|_{r_{j-1}}^{r_j} \quad (1-7)$$

With the substitutions

$$\delta = r_f - r_o$$

$$r_j = r_o + x_+$$

$$r_{j-1} = r_o + x_-$$

where  $r_o$  is the position for which the neutral atom density is given as  $N_o$ , then

$$\tau_j(\nu) \approx -(\alpha B/5 r_f^4) \left\{ (\delta - x_+)^5 - (\delta - x_-)^5 \right\} \quad (1-8)$$

The alteration of the shape of a spectral line with an incident intensity profile  $J_{j-1}(\nu)$  upon passage through the slab is obtained from eqs (2-36) and (1-8). Hence, the change in a given intensity profile  $J_o(\nu)$ , after passage through a number of plane-parallel absorbing slabs is obtained by repeated application of the combined eqs. (2-36) and (1-8).

The computer program used to numerically evaluate the profile of a self-absorbed spectral line is given below. Several input terms defined in the program are related to quantities in the above equations as

D	neutral atom density, $N_o$
TIME	time after collision, $t$
G	statistical weight, $g$
U	partition function, $U$
E	energy of lower level, $E$
TC	temperature at impact center, $T_c$
WAVE	wavelength, $\lambda_o$
F	oscillator strength, $f_{abs}$

A            collision damping constant,  $\gamma$   
 CONST       absorption slab thickness,  $r_j - r_{j-1}$

D is in units of  $10^{18} \text{ cm}^{-3}$ , TIME in  $\mu\text{sec}$ , E in eV, TC in  $^{\circ}\text{K}$ , WAVE and A are in angstrom units.

The calculations proceed in the following manner. The initial position R at which the neutral atom density is D is first calculated in accord with eq. (1-3). The intensity profile of the radiation incident on the first absorbing slab RELIN(J) is then determined at fixed wavenumber increments DNU(J). This profile has a Lorentzian shape with a halfwidth determined by the neutral atom density. DD(J) is the wavelength equivalent of DNU(J). The radial positions of the faces of the absorbing slab are called X<sub>-</sub> and X<sub>M</sub>, and are equivalent to  $x_-$  and  $x_+$  in the above equations. The average collision damping constant A1 and temperature TEMP in the absorbing slab are then calculated. The quantities ALPHA and B(J) which are the equivalent of  $\alpha$  and  $\beta$  in the above equations are obtained and the opacity of the slab BRIT(J) at the wavelength increment DD(J) is then calculated as in eq. (1-7). The intensity profile after passage through the first slab is found and relabeled BRIT(J). This profile becomes the incident profile for the next slab, RELIN(J). The radial positions X<sub>-</sub>, X<sub>M</sub> of the next adjacent absorbing slab are then obtained and similar calculations leading to the intensity profile after passage through the second slab are done. These calculations are further repeated until the position of the front of the expanding collision-produced sheet is reached.

The program output consists of the initial intensity profile before absorption, the total opacity OPAC of the absorbing regions as given by eq. (2-36), and the intensity profile of the emerging radiation. This latter profile is also normalized to its peak computed value to facilitate comparison with profiles of observed spectral lines.

A number of self-absorbed spectral profiles for the CuI 4651 and 5153 transitions have been computed the results of which are shown in the following figures. Values of the neutral atom density used in the calculations were obtained from the measured density variations illustrated in Fig. 26. Estimates of the initial collision damping halfwidth were obtained from these density values and known oscillator strengths by means of eq. (2-21a). The temperature of the material at the entrance face of the absorbing layers was treated as a parameter in the computations and is indicated in the figures.



**BLANK PAGE**

```

C      SPECTRAL LINE ABSORPTION MK4
C      SW 1 ON TO PUNCH INTERMEDIATE PROFILES
C      DATA FROM COLLISION MODEL USED
C      D IN E+18, TIME IN USEC, DEL IN CM
      DIMENSION DNU(40),RELIN(40),B(40),BRIT(40),DD(40),AMP(40)
1 READ 99, D
  READ 99, TIME
  READ 99, G,U,E
  READ 99, T
  READ 99, WAVE,F,A
  READ 98, DELAM,LTERM
  READ 99, CONST
  PUNCH 99, D,TIME,T
  PUNCH 99, WAVE,F,A
  PUNCH 99, CONST , G, U, E
  PUNCH 95
  TT=TIME*TIME
  TTR=1.0/TT
  DIST=D*TT*1.0995E-05
  DIST=SQRTF(DIST)
  R=1.0-SQRTF(DIST)
  RF=1.720*TIME
  R=R*RF
  DEL=RF-R
  RF=1.0/RF
  WAVE=WAVE*1.0E-08
  A=A*1.0E-08
  A=WAVE+A
  A=((1.0/WAVE)-(1.0/A))*3.0E+10
  AA=A*A
  BETA=A/(DEL*RF)**4
  U=-DELAM
  DO 2 J=1,LTERM
    D=U+DELAM
    WAVEK=D*1.0E-08+WAVE
    DNU(J)=((1.0/WAVE)-(1.0/WAVEK))*3.0E+10
    RELIN(J)=AA/(DNU(J)*DNU(J)+AA)
    AMP(J)=RELIN(J)
    DD(J)=D
2 PUNCH 97, DD(J),RELIN(J)
  X=0.0
  XM=CONST*DEL
6 I=0
  Z1=BETA*(1.0-(R+X)*RF)**4
  AA1=BETA*(1.0-(R+XM)*RF)**4
  A1=0.5*(Z1+AA1)
  PUNCH 96, Z1,AA1
  P=(R+X)*RF
  P2=P*P
  Q=(R+XM)*RF
  Q2=Q*Q
  T1=T*(3.772605-3.679437*P-7.065880*P2+10.06610*P2*P-3.092834*P2*
X P2)
  T2=T*(3.772605-3.679437*Q-7.065880*Q2+10.06610*Q2*Q-3.092834*Q2*
X Q2)
  TEMP=0.5*(T1+T2)
  EX=(E*1.160562E+04)/TEMP
  PUNCH 96, T1,T2,TEMP,EX
  PUNCH 95
  IF (EX-230.0) 20,20,23
20 ALPHA=(9.095E+22)*G*EXP(-EX)

```

```

ALPHA=ALPHA*TTR/U
QTY=0.2*ALPHA*RF**4
B1 =0.008448*F*A1*QTY
DO 3 J=1,LTERM
3 B(J)=B1 / (DNU(J)*DNU(J)+A1*A1)
DELA=(DEL-X)**5
DELB=(DEL-XM)**5
DO 5 J=1,LTERM
BRIT(J)=B(J)*(DELB-DELA)
BRIT(J)=RELIN(J)*EXP(BRIT(J))
RELIN(J)=BRIT(J)
10 IF (1) 4,4,5
4 I=1
POS=R+X
POSN=POS*RF
PUNCH 99, POS, POSN
IF (SENSE SWITCH 1) 9,5
9 PUNCH 97, DD(J), BRIT(J)
5 CONTINUE
X=XM
XM=XM+CONST*DEL
IF (XM-DEL) 6,6,23
23 DO 24 J=1,LTERM
24 PUNCH 97, DD(J), BRIT(J)
PUNCH 95
DO 8 J=1,LTERM
AMP(J)=BRIT(J)/AMP(J)
OPAC=-LOGF(AMP(J))
8 PUNCH 97, DD(J), OPAC
PUNCH 95
BMX = BRIT(1)
DO 30 J = 2, LTERM
IF ( BRIT(J) - BMX ) 30, 31, 31
31 BMX = BRIT(J)
30 CONTINUE
DO 32 J = 1, LTERM
BRIT(J) = BRIT(J)/BMX
32 PUNCH 97, DD(J), BRIT(J)
PUNCH 95
GO TO 1
99 FORMAT (4F10.3)
98 FORMAT (F10.3,15)
97 FORMAT (F10.3,E20.8)
96 FORMAT (4E20.8)
95 FORMAT (/)
END

```

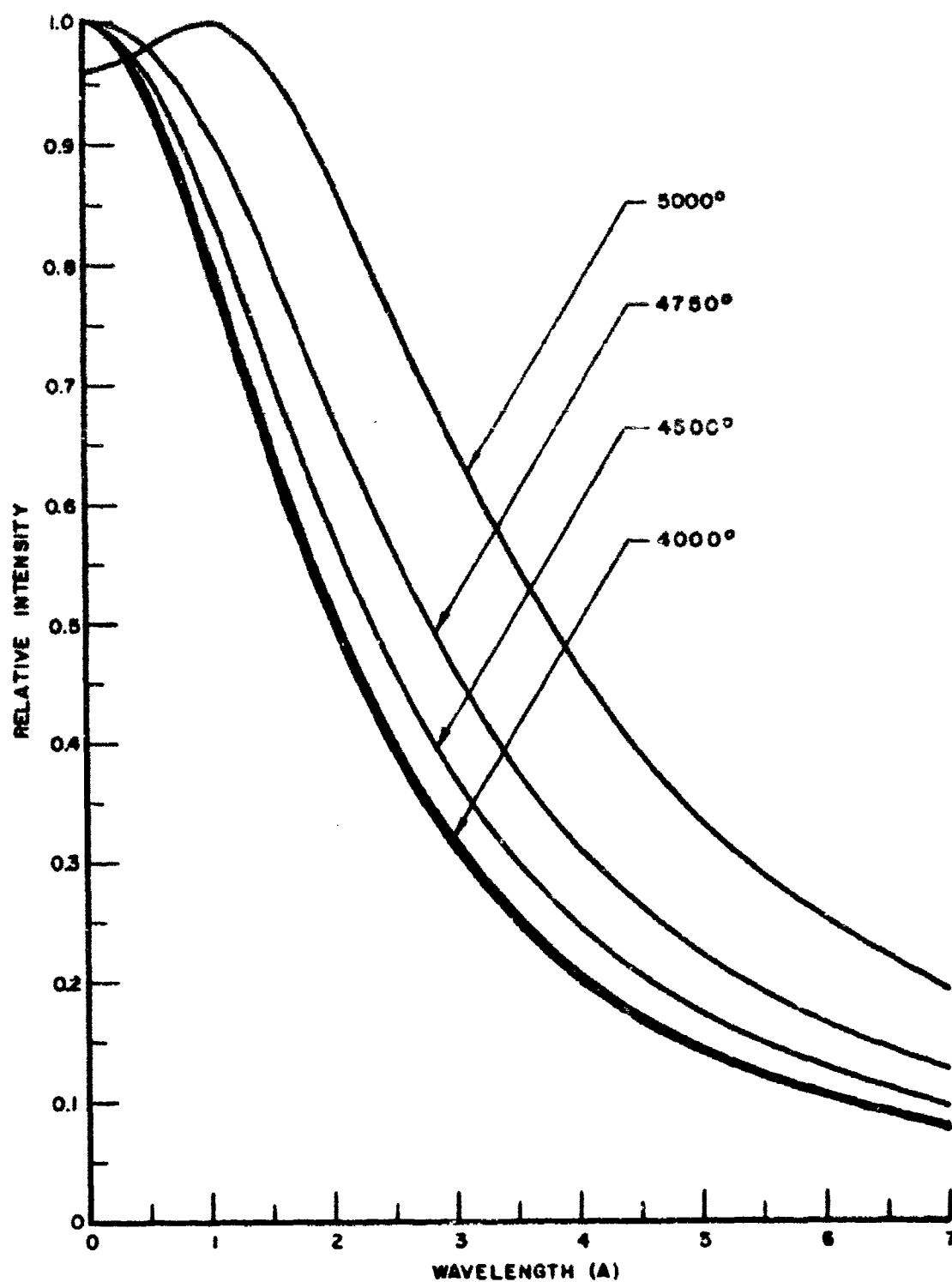


FIG. I-1. NORMALIZED SELF-ABSORBED Cu I 4651 PROFILE

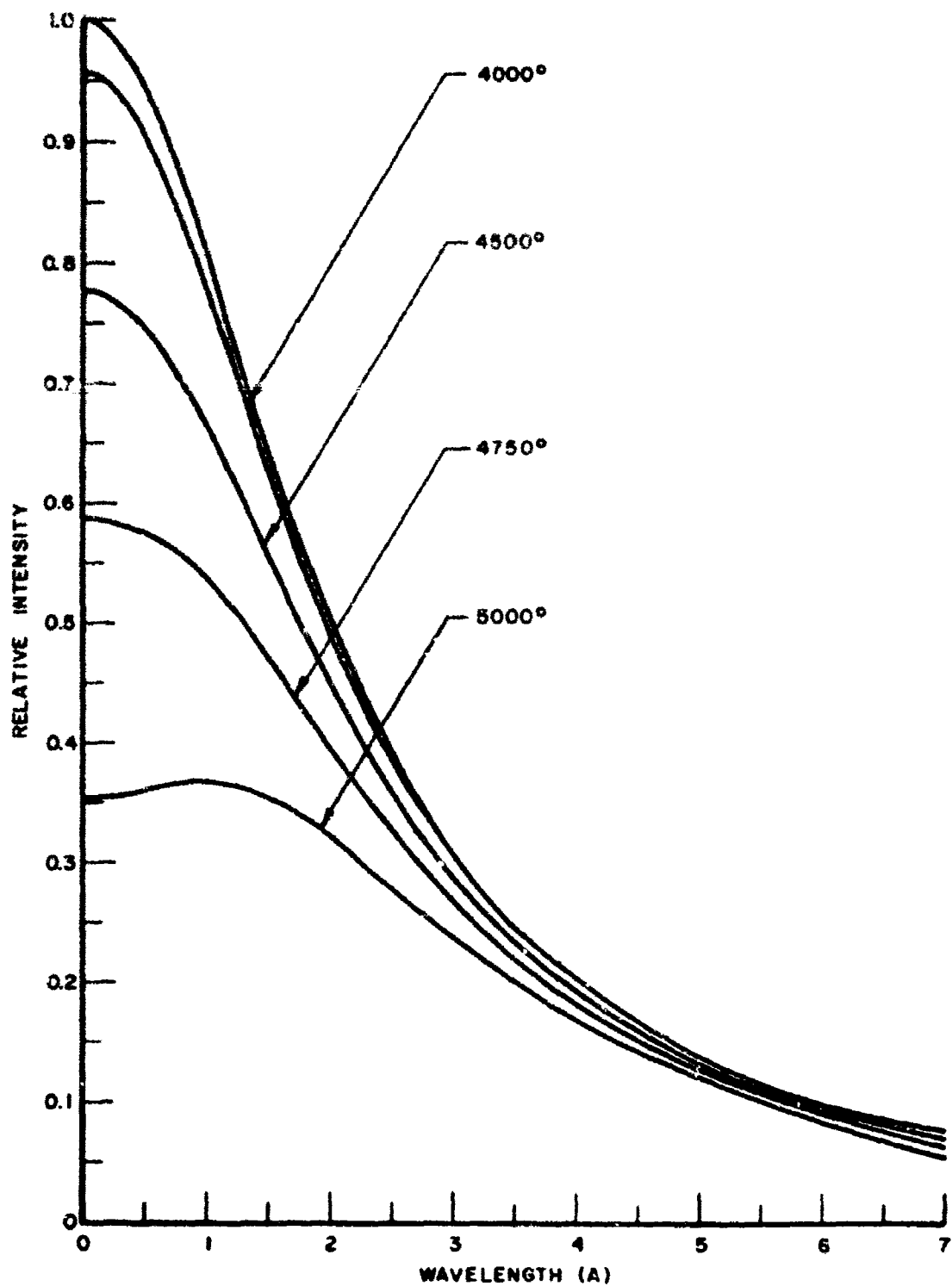


FIG.I-2. SELF-ABSORBED Cu I 4651 PROFILE

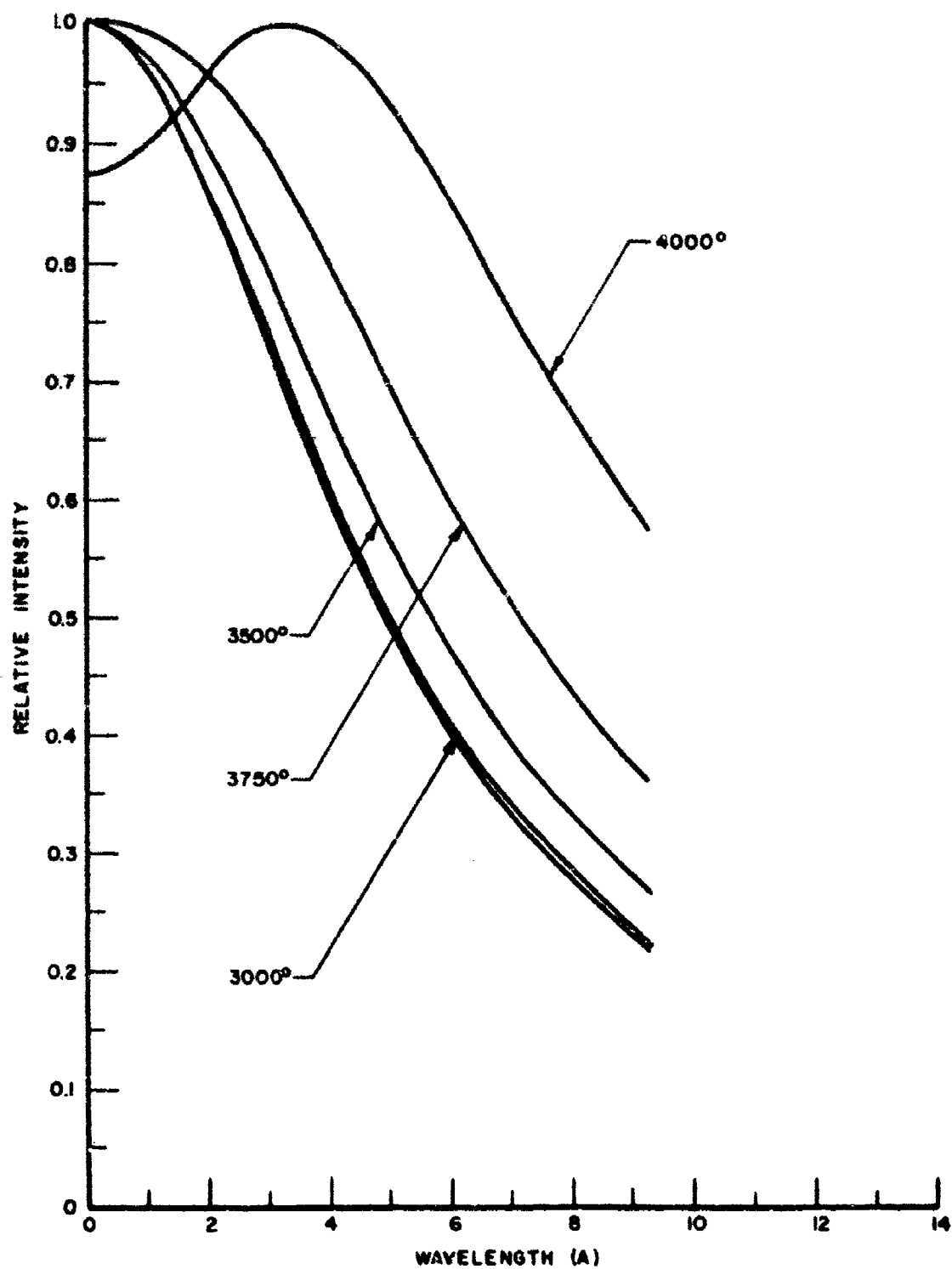
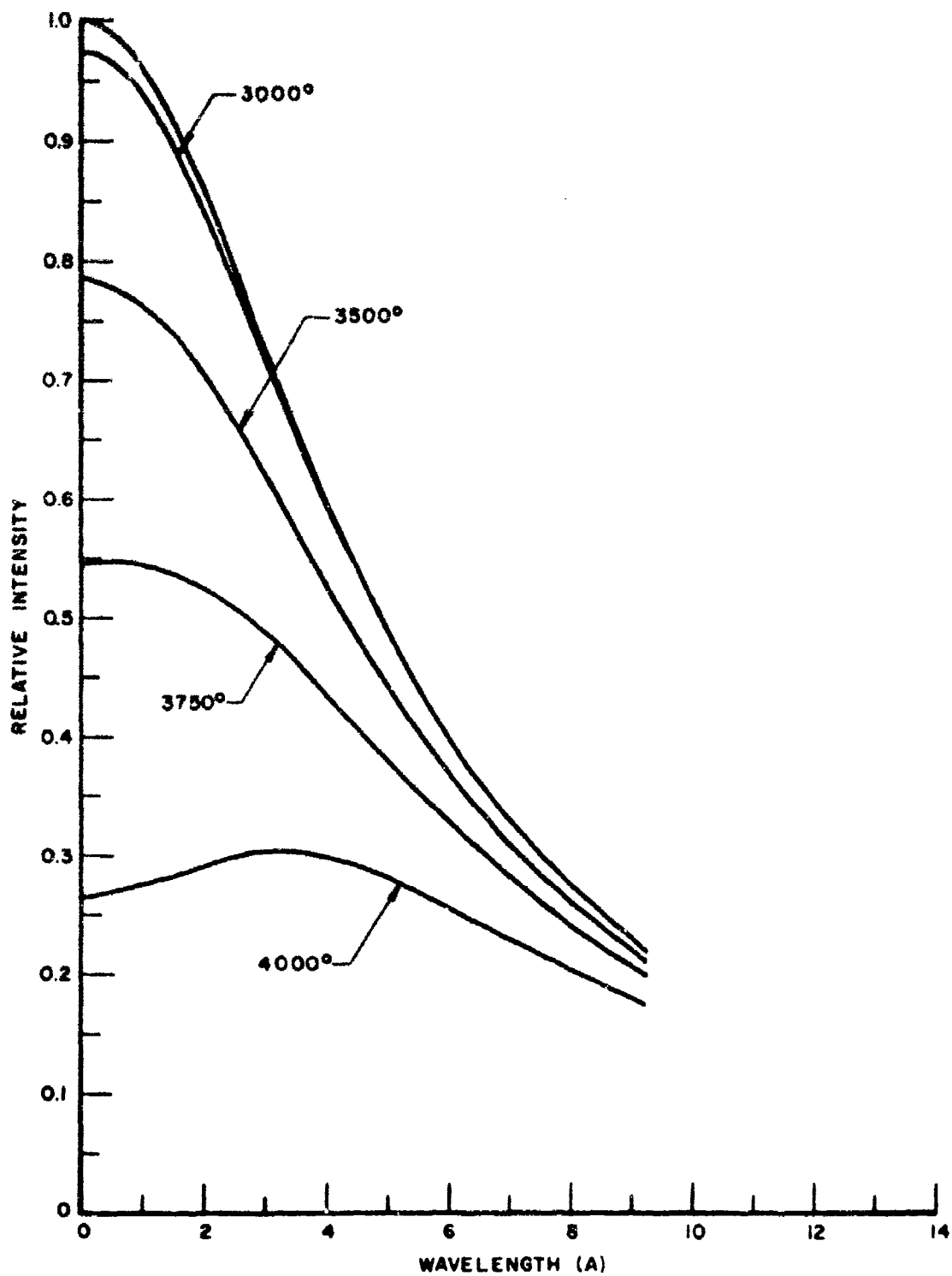


FIG. I-3. NORMALIZED SELF-ABSORBED Cu I 5153 PROFILE



FIGI-4. SELF-ABSORBED Cu I 5153 PROFILE

## References

- C. W. Allen, Phys. Rev. 39, 42 (1932)
- C. W. Allen, Phys. Rev. 39, 55 (1932)
- C. W. Allen and A. S. Asaad, Monthly Not. Roy. Astron Soc. 117, 36 (1957)
- C. W. Allen, "Astrophysical Quantities," Second edition, Oxford University Press, New York (1963)
- W. A. Allen, H. L. Morrison, D. B. Ray, and J. W. Rogers, "Proceedings of the Third Symposium on Hypervelocity Impact," Armour Research Foundation, Illinois (Feb. 1959)
- L. H. Aller, "Astrophysics, the Atmospheres of the Sun and Stars," The Ronald Press, New York (1953)
- V. N. Alyamovskii, and V. F. Kitaeva, Optika i Spektrosk 8, 152 (1959)
- V. A. Ambartsumyan, "Theoretical Astrophysics," Pergamon Press, New York (1958)
- J. A. Anderson, Astrophys J. 51, 37 (1920)
- E. C. C. Baly, "Spectroscopy," Longman, Green and Co., London (1905)
- M. Baranger, Phys. Rev. 111, 494 (1958)
- Y. Beers, "Introduction to the Theory of Error," Addison-Wesley Pub. Co., Mass. (1958)
- T. Bergstrahl, D. Krucoff, N. Meyer, and J. Worcester, "Final Report on Study of Methods of Producing High-Speed Particles" Pub. No. V-698, Aeronautronic Division, Ford Motor Co., (Nov. 1959)
- H. A. Bethe, K. Fuchs, J. O. Hirschfelder, J. L. Magee, R. E. Peierls, and J. von Neumann, "Blast Wave," Los Alamos Scientific Laboratory, LA-2000, Los Alamos, New Mexico (Aug. 1947)
- G. Birkhoff, D. P. MacDougall, E. M. Pugh, and Sir G. Taylor, J. Appl. Phys. 19, 563 (1948)
- A. S. Bishop, "Project Sherwood, The U. S. Program in Controlled Fusion," Addison-Wesley Pub. Co., Mass. (1958)
- P. Bogen, Z. Phys. 149, 62 (1957)



- W. A. Boyd, W. S. Partridge, and E. T. Cannon, "Proceedings of the Third Symposium on Hypervelocity Impact," Armour Research Foundation, Illinois (Feb. 1959)
- R. G. Breene Jr., Rev. Mod. Phys. 29, 94 (1957)
- R. G. Breene Jr., "The Shift and Shape of Spectral Lines," Pergamon Press, New York (1961)
- S. Brodersen, J. Opt. Soc. Amer. 43, 877 (1953)
- W. Brugel, "An Introduction to Infrared Spectroscopy," J. Wiley (1962)
- W. G. Chace, and H. K. Moore, editors, "Exploding Wires" Vol 1 and 2, Plenum Press, New York (1959, 1962)
- S. Chandrasekhar, "An Introduction to the Study of Stellar Structure," University of Chicago Press, Illinois (1939)
- G. L. Clark, editor, "The Encyclopedia of Spectroscopy," Reinhold Pub. Co., New York (1960)
- J. S. Clark, R. R. Kadesch, and R. W. Grow, University of Utah Technical Report OSR-13, University of Utah (Sept. 1959)
- E. U. Condon, and G. H. Shortley, "The Theory of Atomic Spectra," Cambridge University Press, Mass. (1959)
- M. A. Cook, "The Science of High Explosives," Reinhold Co., New York (1958)
- M. A. Cook, and R. T. Keyes, "Proceedings of the Third Symposium on Hypervelocity Impact," Armour Research Foundation, Illinois (Feb. 1959)
- C. H. Corliss, J. Res. Nat. Bur. Stand. 66A, 497 (1962)
- C. H. Corliss, and W. R. Bozman, "Experimental Transition Probabilities for Spectral Lines of Seventy Elements," Nat. Bur. Stand. Monograph 53, (1962)
- R. Courant, and K. O. Friedrichs, "Supersonic Flow and Shock Waves," Interscience Pub. New York (1948)
- G. C. Crews, "Proceedings of the Third Symposium on Hypervelocity Impact," Armour Research Foundation, Illinois (Feb. 1959)

- M. L. Dalton Jr., Appl. Optics 2, 1195 (1963)
- D. M. Dennison, Phys. Rev. 31, 503 (1928)
- E. M. Dewan, Phys. of Fluids 4, 759 (1961)
- P. J. Dickerman, editor, "Optical Spectrometric Measurements of High Temperatures," University of Chicago Press, Illinois (1961)
- R. J. Donohue, and R. F. Majkowski, J. Appl. Phys. 33, 3 (1962)
- H. Edels, and J. D. Craggs, Proc. Phys. Soc. (London) A64, 575 (1951)
- R. J. Eichelberger, and E. M. Pugh, J. Appl. Phys. 23, 537 (1952)
- R. J. Eichelberger, J. Appl. Phys. 26, 398 (1955)
- H. Fisher, and L. C. Mansur, "Conference on Extremely High Temperatures," J. Wiley, New York (1958)
- H. M. Foley, Phys. Rev. 69, 616 (1946)
- N. E. Forsythe, editor, "Measurement of Radiant Energy," McGraw-Hill Pub. Co., New York (1937)
- J. F. Friichtenicht, and J. C. Slattery, "Ionization Associated with Hypervelocity Impact," Space Technology Laboratories, Calif. (March 1963)
- Y. Fujioka, and S. Nakamura, Astrophys. J. 65, 201 (1927)
- W. Furrssow, and A. Wlassow, Physik Z. Sowjetunion 10, 378 (1936)
- J. J. Gilvarry, and J. E. Hill, Astrophys. J. 124, 610 (1956)
- W. Goldsmith, "Impact," Edward Arnold Pub., London (1960)
- J. Greenstein, editor "Stellar Atmospheres," University of Chicago Press, Illinois (1960)
- H. R. Griem, Z. Phys. 137, 280 (1954)
- H. R. Griem, A. C. Kolb, and K. Y. Shen, Phys. Rev. 116, 4 (1959)
- H. R. Griem, "Plasma Spectroscopy," McGraw-Hill Pub., New York (1964)

- R. W. Grow, R. R. Kadesch, E. P. Palmer, W. H. Clark, J. S. Clark, and R. E. Blake, "Proceedings of the Fourth Symposium on Hypervelocity Impact," Eglin Air Force Base, Florida (April 1960)
- E. R. Harrison, Phys. Rev. Letters 11, 535 (1963)
- W. D. Henkel, Z. Phys. 137, 295 (1954)
- G. Herzberg, "Atomic Spectra and Atomic Structure," Prentice-Hall Inc., New York (1937)
- J. Holtsmark, Ann. Physik 58, 577 (1919)
- J. Holtsmark, Z. Physik 25, 73 (1924)
- J. Holtsmark, and B. Trumpp, Z. Phys. 31, 803 (1925)
- R. L. Jameson, Private communication, (1963)
- G. Joos, "Theoretical Physics," Blackie and Son Pub., London, (1951)
- R. T. Keys, R. W. Bartlett, and M. A. Cook, "Proceedings of the Fourth Symposium on Hypervelocity Impact," Eglin Air Force Base, Florida (April 1960)
- J. H. Kineke Jr., "Proceedings of the Third Symposium on Hypervelocity Impact," Armour Research Foundation, Illinois (Feb. 1959)
- G. W. King, and A. G. Emslie, J. Opt. Soc. Amer. 41, 405 (1951)
- B. Kivel, Phys. Rev. 98, 1055 (1955)
- Eastman Kodak Co., "Kodak Plates and Films for Science and Industry," No. P-9, Rochester (1962)
- A. C. Kolb, "Theory of Hydrogen Line Broadening in High Temperature Partially Ionized Gases," (Thesis), University of Michigan, Michigan (1956)
- A. C. Kolb, and H. R. Griem, Phys. Rev. 111, 514 (1958)
- S. Koslov, Private communication, (1959)
- G. P. Kuiper, editor, "The Solar System," Vol. 1, "The Sun", University of Chicago Press, Illinois (1962)

- E. Lindholm, Z. Physik 109, 223 (1938)
- W. Lochte-Holtgreven, Z. Phys. 109, 358 (1938)
- W. Lochte-Holtgreven, Rep. Progr. Phys. 21, 312 (1958)
- S. J. Lukasik, B. J. Pernick, C. E. Grosch, and S. Koslov,  
Bull. Amer. Phys. Soc. 9, 593 (a) (1964)
- H. Margenau, and W. Watson, Rev. Mod. Phys. 8, 22 (1936)
- H. Margenau, and M. B. Lewis, Rev. Mod. Phys. 31, 569 (1959)
- H. Margenau, "Proceedings of the Fourth International Conference on  
Ionization Phenomena in Gases," Upsala (1959), N. R. Nilson, editor,  
North-Holland Pub. Co., Amsterdam
- C. E. K. Mees, "The Theory of the Photographic Process,"  
Macmillan Co., New York (1946)
- L. Minnhagen, J. Opt. Soc. Amer. 54, 320 (1964)
- A. C. G. Mitchell, and M. W. Zemansky, "Resonance Radiation and  
Excited Atoms," Cambridge University Press, Mass. (1934)
- C. E. Moore, "Atomic Energy Levels as Derived from the Analysis of  
Optical Spectra," Vol. 11, Nat. Bur. Stand. Circular 467, (Aug. 1952)
- H. Nagaoka, and Y. Sugiura, Japan J. Phys. 3, 45 (1924)
- J. R. Nielsen, V. Thornton, and E. B. Dale, Rev. Mod. Phys. 16, 307  
(1944)
- N. H. Olsen, and W. S. Huxford, Phys. Rev. 87, 922 (1952)
- S. S. Penner, "Quantitative Molecular Spectroscopy and Gas  
Emissivities," Addison-Wesley Pub. Co., Mass. (1959)
- H. E. Petschek, P. H. Rose, H. S. Glick, A. Kune, and A. Kantrowitz,  
J. Appl. Phys. 26, 83 (1955)
- Z. Pressman, "Proceedings of the Fifth International Congress of High  
Speed Photography," J. S. Courtney-Pratt, editor, Society of  
Motion Picture and Television Engineers, (1962)
- E. M. Pugh, R. J. Eichelberger, and N. Rostoker, J. Appl. Phys. 23,  
532 (1952)

- R. J. Reithel, J. H. Blackburn, G. E. Seay, and S. Skolnick,  
"Exploding Wires," Vol. 1, W. C. Chace and H. K. Moore, editors,  
Plenum Press, New York (1959)
- R. A. Sawyer, and H. B. Vincent, J. Opt. Soc. Amer. 33, 247 (1943)
- R. A. Sawyer, "Experimental Spectroscopy," Prentice-Hall Inc.,  
New York (1951)
- G. E. Seay, L. B. Seely, and R. G. Fowler, J. Appl. Phys. 32, 2439 (1961)
- A. G. Shenstone, Phys. Rev. 39, 63 (1932)
- A. G. Shenstone, Phil. Trans. Roy. Soc. A235, 195 (1936)
- A. G. Shenstone, Phil. Trans. Roy. Soc. A241, 297 (1948)
- J. C. Slater, Phys. Rev. 25, 783 (1925)
- S. Smith, Astrophys. J. 61, 186 (1925)
- J. L. Summers, and A. C. Charters, "Proceedings of the Third Symposium  
on Hypervelocity Impact," Armour Research Foundation,  
Illinois (Feb. 1959)
- T. Takamine, Astrophys. J. 50, 23 (1919)
- E. B. Turner, "The Production of Very High Temperatures in the Shock  
Tube with an Application to the Study of Spectral Line Broadening,"  
(Thesis), University of Michigan, Michigan (1956)
- C. E. Walbrecht, "Exploding Wires," Vol. 1, W. C. Chace and H. K. Moore,  
editors, Plenum Press, New York (1959)
- J. M. Walsh, R. G. Shreffler, and F. J. Willig, J. Appl. Phys. 24,  
349 (1953)
- J. M. Walsh, and R. H. Christian, Phys. Rev. 97, 1544 (1955)
- V. F. Weisskopf, Z. Physik 77, 398 (1932)
- H. E. White, "Introduction to Atomic Spectra," McGraw-Hill Pub.,  
New York (1934)

## Acknowledgements

The author wishes to express his gratitude to Dr. S. Koslov and Dr. S. J. Lukasik for suggesting this area of research as a thesis endeavor. The author is deeply indebted to Dr. S. J. Lukasik for his valuable guidance and concern throughout all phases of this work from its inception to its present form; to Mr. C. E. Grosch for numerous helpful and enlightening discussions, to Mr. G. W. Zepko for his guidance in computer programming and operation, and to Mr. S. Chen for his assistance in the preparation of Autoplotter computer programs. The author wishes to thank Mr. F. R. Schwartz and associates at Picatinny Arsenal for their assistance in the operation of the high speed camera facilities; to Mr. D. Simon of Vitro Laboratories for the use of that laboratory's densitometer and associated equipment, to Mr. R. L. Jameson of the Ballistic Research Laboratories for assistance in using the computing facilities (BRLESC) at the Aberdeen Proving Grounds, and to a number of employees of the Davidson Laboratory for their cooperation in the preparation of this work.

Computations were carried out on an IBM 1620 digital computer located at the Computer Center of Stevens Institute of Technology, which is partly supported by the National Science Foundation. This work was derived from a research effort under the auspices of the Ballistic Research Laboratories, Aberdeen Proving Grounds, Aberdeen, Maryland.